



FACULTY OF SCIENCE
DEPARTEMENT OF PHYSICS

Study of transverse momentum dependent formalisms

PROEFSCHRIFT TER VERKRIJGING VAN DE GRAAD VAN MASTER IN DE FYSICA

Maxim PAVLOV
Supervisor: Prof. Dr. Francesco Hautmann

Year 2019-2020

Samenvatting

Eén van de processen die het meest geproduceerd wordt in de *Large Hadron Collider* (LHC), is de botsing tussen protonen. Door de aanwezigheid van hoogtechnologische detectoren kunnen verschillende eigenschappen van de producten uit deze interacties tot op een hoge nauwkeurigheid gemeten worden. Op deze manier tracht men afwijkingen binnen het Standaardmodel te vinden. Hiervoor is het nodig dat ook de theoretische voorspellingen een hoge nauwkeurigheid bevatten, wat binnen de sterke wisselwerking niet evident is. Vaak worden interacties van het Standaardmodel berekend met behulp van storingsrekening. Dit is echter alleen mogelijk als de interactie zwak is. Dit is niet altijd het geval voor de sterke wisselwerking door de koppingsconstante α_S die varieert met de energie. Bij hoge energieën is de interactie zwak genoeg om storingsrekening te kunnen gebruiken. Bij lagere energieën is dit echter niet meer mogelijk. Dit zorgt ervoor dat quarks en gluonen, die samen partonen worden genoemd, met elkaar gaan binden om hadronen te vormen, waarvan het proton een welbekend voorbeeld is. Dit impliceert echter ook dat laag-energetische contributies steeds aanwezig zullen zijn in de proton-proton botsingen. De werkzame doorsnede van deze interacties kan dus niet berekend worden met storingsrekening.

Hier biedt collineaire factorisatie een oplossing voor. Het ontbindt de uitdrukking voor de werkzame doorsnede in twee factoren die de interactie beschrijven op verschillende energieschalen. De bijdragen vanuit het hoogenergetisch regime kunnen berekend worden met storingsrekening. Deze beschrijven het proces waaraan de partonen deelnemen, wat de harde interactie wordt genoemd. De laagenergetische bijdragen worden voorgesteld door een parton distributie functie (PDF), die de verdeling van de partonen binnenin het proton of andere hadronen beschrijft. Dit is een functie die afhangt van de fractie x van de proton impuls en van de energieschaal Q . De PDFs kunnen niet berekend worden, maar binnen de kwantumchromodynamica (QCD) kan wel hun energieafhankelijkheid beschreven worden door de Dokshitzer-Gribov-Lipatov-Altarelli-Parisi (DGLAP) vergelijkingen. Deze worden daarom ook evolutievergelijkingen genoemd. Eens de PDF gekend is op een initiële energieschaal, wat men verkrijgt door deze te fitten aan experimentele waarnemingen, kan de uitdrukking voor deze functie op andere energieschalen verkregen worden met de DGLAP vergelijkingen. Belangrijk hierbij is het feit dat de PDFs niet afhangen van de harde interactie. Dezelfde PDFs kunnen dus gebruikt worden voor verschillende processen, zolang dezelfde hadronen deelnemen aan de interacties. De energieafhankelijkheid van de PDFs impliceert dat de inwendige structuur van een proton niet steeds dezelfde is. Bij hogere energieën kunnen meer parton vertakkingen onderscheiden worden, waardoor de verdeling van de partonen verandert.

Collineaire factorisatie zorgt ervoor dat verschillende interacties met een hoge nauwkeurigheid voorspeld kunnen worden. Het werkt echter minder goed als meerdere schalen een rol spelen in het proces. Een voorbeeld dat grondig werd bestudeerd in deze thesis, is de transversale impuls q_T distributie van het Z boson, geproduceerd in het Drell-Yan proces door annihilatie van een quark en een antiquark. Als men dit probeert te berekenen met collineaire factorisatie, dan verschijnen machten van $\log(Q^2/q_T^2)$ in de termen van de expansie van de harde interactie. Deze zijn afkomstig van het uitstralen van een willekeurig aantal gluonen met een lage energie, die ervoor zorgen dat het Z boson een lage transversale impuls kan verkrijgen. Hierbij worden de hogere-orde termen in de expansie te groot door de vernoemde logaritmen om verwaarloosd te kunnen worden. Een grote onnauwkeurigheid verschijnt dan op de berekende waarden en het is daarom nodig om alle hogere orde termen te hersommen.

In deze thesis werden twee verschillende formalismen bestudeerd die de transversale impuls van de partonen mee in rekening nemen. Het Collins-Soper-Sterman (CSS) formalisme werd oorspronkelijk geformuleerd voor het Drell-Yan proces en is later uitgebreid naar gelijkaardige interacties. Het is al een lange tijd in gebruik voor het hersommen van de bijdragen van laagenergetische gluonen. De uitdrukking voor de werkzame doorsnede bestaat hierbij uit de PDFs samen met meerdere functies die hogere-orde correcties met verschillende groottes in transversale impuls voorstellen. Eén van die functies is de Sudakov vorm factor die instaat voor de hersommatie. Het problematisch logaritme verschijnt hier in een exponentiële functie samen met twee perturbatieve functies A en B . De expansie van de Sudakov vorm factor omvat dus alle machten van dit logaritme.

Het tweede formalisme is de parton branching (PB) methode, een recent ontwikkelde methode die eerder focust op de PDFs in plaats van op het berekenen van werkzame doorsnedes. Het gaat hier ook niet meer

over collineaire PDFs maar over TMD (*transverse momentum dependent*) PDFs, die een bijkomende afhankelijkheid van de transversale impuls van het parton erbij hebben gekregen. Het PB formalisme beschrijft hoe de DGLAP vergelijkingen omgevormd kunnen worden tot evolutievergelijkingen voor de TMD PDFs. Deze vergelijkingen kunnen dan opgelost worden met een Monte Carlo simulatie om TMD PDFs te verkrijgen over een groot kinematisch bereik. Het CSS formalisme daarentegen is alleen geldig voor $q_T \ll Q$. Ook in de PB methode is er een Sudakov vorm factor aanwezig die bestaat uit perturbatieve functies k en d . Deze factor zorgt weer voor de hersommatie, maar heeft binnen het formalisme nog een andere eigenschap: het geeft de kans dat een parton niet splitst wanneer de energieschaal verhoogd wordt. Met behulp van de Sudakov vorm factor en splitsingsfuncties, die de waarschijnlijkheid aangeven dat er wel een splitsing plaatsvindt, kan zo een simulatie verkregen worden van hoe de TMD PDF verandert als functie van de energieschaal.

Het uiteindelijke doel van deze thesis was om een vergelijkende studie uit te voeren tussen de genoemde formalismen. Op analytisch vlak zijn de twee Sudakov vorm factoren onlangs vergeleken geweest met elkaar tot op NNLL (*next-to-next-to-leading logarithm*) nauwkeurigheid. Dat toonde aan dat de LL en NLL orden met elkaar overeen kwamen. Voor de NNLL orde werd er wel een verschil vastgesteld. Dat kan verklaard worden door het feit dat de Sudakov vorm factor uit het CSS formalisme afhankelijk is van de harde interactie, wat niet het geval is voor deze factor in de PB methode. Deze studie is nog steeds gaande en een stand van zaken wordt beschreven.

De focus van de thesis lag meer op een numerieke vergelijking tussen de twee formalismen, waarbij voorspellingen voor de transversale impuls distributie van het Z boson werden bestudeerd. Dit is origineel werk en de figuren hiervoor werden gemaakt door gebruik te maken van verschillende bestaande programma's. Eén van deze programma's was reSolve, een C++ programma dat het CSS formalisme implementeerd. Het is recent ontwikkeld geweest en is nog steeds in opbouw. Transversale impuls spectra werden geproduceerd voor verschillende nauwkeurigheden om deze systematisch te bestuderen. Ter controle werden ook experimentele waarnemingen van de ATLAS detector toegevoegd aan de figuren om de precisie van de resultaten te beoordelen. De grafieken vertonen een gelijkaardige overeenkomst die werd bekomen in de analytische vergelijking. Verder laten de geproduceerde figuren ook merken dat de relatief nieuwe PB methode in staat is om resultaten van dezelfde kwaliteit te bekomen als het gerenommeerd CSS formalisme.

Abstract

The Standard Model (SM), on which the current knowledge on particle physics is based, is extremely successful. It is able to predict the outcome of many experiments. However, it has its limitations. Experimental and theoretical physicists are therefore looking for signs of Beyond Standard Model (BSM) processes. The SM can be studied experimentally in colliders like the Large Hadron Collider (LHC). Precision measurements are hereby one of the approaches to search for BSM processes, because any deviation from the SM predictions could be a sign of BSM processes.

One of the uncertainty sources in theoretical predictions are QCD (Quantum Chromodynamics) processes. Usually perturbation theory is used to obtain these predictions, but this does not always hold for the strong interaction due to the running of the strong coupling, which displays the strength of the interaction and increases for low energies. Low-energy contributions are however always present in interactions involving protons, which means that the cross section for these interactions is not calculable with perturbation theory. The collinear factorization theorem provides the solution by decomposing the expression for the cross section into a hard process and parton distribution functions (PDFs). The hard process is the interaction that takes place at the highest energy scale and is therefore calculable with perturbation theory. The PDFs describe the distributions of quarks and gluons (partons) inside the proton and are functions of the momentum fraction x carried by these particles and the energy scale Q^2 . It is not possible to calculate an explicit expression for the PDFs, but their Q^2 dependence is described by the Dokshitzer-Gribov-Lipatov-Altarelli-Parisi (DGLAP) equations. Most importantly is that the PDFs are the same for all hard processes for a given hadron. If they are extracted from the measurements of one process, they can be used for obtaining the prediction of another process, which would involve the same hadron.

The collinear factorization in collider physics provides excellent results for processes characterized by a single scale, but breaks down when multiple scales are involved. Emissions of low-energy (soft) gluons cause the appearance of $\log(\frac{Q^2}{q_T^2})$ factors at all orders in the perturbative expansion of the hard process. For low transverse momenta, the higher order terms can no longer be neglected and therefore the obtained results are inaccurate. Transverse momentum dependent (TMD) factorization has then been set up to take into account the transverse momentum of the partons with respect to the beam axis in the calculations for the cross section in order to provide more accurate results.

This thesis studied two formalisms for TMD physics and their predictions for the transverse momentum spectrum of the Z boson, produced through the Drell-Yan process (quark-antiquark annihilation). The Collins-Soper-Sterman (CSS) formalism is a well-established method that provides a resummation for the contributions of the soft gluons up to all orders in the coupling constant at a certain logarithmic accuracy. It factorizes the expression for the cross section into PDFs and perturbative functions that each represent contributions from processes with different transverse momentum. One of these is the Sudakov form factor, which represents the resummation. The second formalism is a relatively new one, called the parton branching (PB) method, and it provides equations for the Q^2 dependence of TMD PDFs together with an iterative Monte Carlo (MC) solution method to obtain TMD PDFs valid over a broad kinematic range. The Sudakov form factor also appears in this formalism, which again represents the resummation of the soft gluons.

In this thesis, the two approaches are compared at both analytical and numerical level. The analytical comparison shows a correspondence between the Sudakov form factors up to NLL accuracy. At NNLL, the comparison becomes more difficult because the Sudakov form factor from the CSS formalism is not unambiguously defined. It depends on the hard process, which is not the case for the PB formalism.

The main result of the thesis is the numerical comparison of the transverse momentum spectra of the Z boson. The produced results are original work and different existing computational programs were used in order to obtain these results. The C++ program reSolve, which implements the CSS formalism, has only been developed recently and is still under construction. For the PB method, the PB TMD PDFs are publicly available in TMDlib and the cross sections from PYTHIA and MC@NLO MC event generators are used in the CASCADE generator. These are then analysed by Rivet. Together with measured data from the ATLAS experiment, the two TMD approaches have been studied at different accuracies. The spectra show a similar correspondence as was observed in the comparison between the Sudakov form factors and conclude that the (relatively-new) PB approach is able to provide results of the same quality as the (well-established) CSS formalism does.

Contents

I	Theory of the strong interaction	11
1	Concepts of QCD	13
1.1	Lagrangian and Feynman rules	13
1.2	Regularization and renormalization	17
1.3	Running of the strong coupling	18
1.3.1	Asymptotic freedom	19
1.3.2	Confinement	20
1.3.3	Λ_{QCD} parameter	20
2	Parton distribution functions	23
2.1	Factorization	23
2.1.1	Deep inelastic scattering	24
2.1.2	Drell-Yan	25
2.2	DGLAP equations	27
2.2.1	Bjorken scaling	27
2.2.2	Breaking of Bjorken scaling	28
2.2.3	Factorization scheme	30
2.2.4	Evolution equations	31
2.2.5	Splitting functions	32
2.2.6	Momentum sum rule	33
2.2.7	Related experimental results	33
2.3	Event generators	34
II	TMD formalisms	37
3	TMD factorization	39
3.1	Introduction	39
3.1.1	Low q_T factorization	39
3.1.2	High-energy factorization	40
3.2	CSS formalism	41
3.2.1	Resummation	41
3.2.2	Resummation scheme	44
3.2.3	Matching procedure	45
3.3	Parton Branching method	46
3.3.1	Resolvable and non-resolvable emissions	47
3.3.2	Sudakov form factor	50
3.3.3	Collinear PDFs	52
3.3.4	TMD PDFs	53

III	Comparison between the PB and CSS formalisms	59
4	Analytic comparison	61
4.1	Sudakov form factors	61
4.1.1	LL order	62
4.1.2	NLL order	62
4.1.3	NNLL order	63
5	Numerical comparison	65
5.1	reSolve	66
5.2	p_T spectrum of Z boson	68
5.2.1	Different orders within reSolve	68
5.2.2	Influence of non-perturbative smearing in reSolve	70
5.2.3	Use of PDF set	71
5.2.4	Comparison between PB and reSolve	72

Introduction

Physicists have always tried to describe the world mathematically as effective as possible. One of the most famous examples would be I. Newton, who casted the motion of an object subjected to different forces into three simple laws. This desire to understand everything has expanded to the complete universe. Theoretical physicist seek the description of phenomena taking place at very short distances, studying the building blocks of life, and very large distances, examining the behaviour of stellar objects like black holes. One of the most noteworthy outcomes from theoretical physics of the previous century is the reduction of all forces in nature to four fundamental ones. The electromagnetic force and gravity are well-known by many people due to their clear presence in daily life. The remaining forces are the weak and strong interaction. Their closest association with generally known phenomena can be found back in nuclear physics. The weak force causes the β -decay of radioactive particles and nuclear fusion processes, while the strong interaction accounts for the attractive nuclear force which binds the particles of a nucleus together.

Quantum Field Theory (QFT) provides a theoretical description for three of the fundamental forces. It is the result of combining Quantum Mechanics with Special Relativity. Together they form the Standard Model of elementary particle physics. This represents our current understanding of the laws of nature, gravity excluded. Although General Relativity provides excellent predictions (some being confirmed only recently, a century after they were pinned down by physicists like A. Einstein), the interaction can not yet be described at quantum level. This is possible for the other three forces, which can be described by interacting fields. Excitations of these fields represent the fermions and bosons. Fermions are the elementary particles like the quarks and electrons that build up the atoms. These two belong to the lightest fermions (with exception of the neutrinos). Heavier ones are encountered less on Earth due to their shorter lifetime, but they are present in large amounts in the universe. Each fundamental force is represented by the exchange of a boson in QFT, making these particles the force-carriers. One exception here is the Higgs boson, which does not carry any force but is actually the materialization of spontaneous symmetry breaking.

The Standard Model would not have become the accepted fundamental theory if it was not possible to validate its predictions. This is where particle accelerators and colliders like the Large Hadron Collider (LHC) play an important role. They accelerate particles (e.g. protons, electrons) so that they collide at high energies. Detectors are then used to identify the abundance of particles produced in the collisions. Both the colliders and the detectors are composed of highly advanced technologies to study the interactions as precise as possible. Throughout the years, results coming from these experiments have provided steady evidence for the Standard Model to be correct and have also provided important input for theoretical developments. The other way around, theoretical physicists offer predictions that can be used in the construction of colliders/detectors to search for new particles or to improve the accuracy on the measurements. These searches are being held because the Standard Model has its limitations. Indications of so-called Beyond Standard Model (BSM) processes are investigated in two ways. One either looks for particular BSM processes by using the theoretical predictions for this or one looks for deviations between the theoretical predictions from the Standard Model and the measurements. For this, both the predictions and the measurements have to be as precise as possible.

This thesis will focus on Quantum Chromodynamics (QCD), the QFT for the strong force that causes the main uncertainty in the theoretical predictions. It describes the interaction between quarks, of which there are six types (flavours), each with their own antiparticle. The interaction takes place through the exchange of a gluon, the force-carrier. Only particles with a so-called colour charge (red, blue or green) participate

in the strong interaction. These colour charges were introduced as an additional degree of freedom to the wavefunctions of quarks to make the Standard Model invariant under local $SU(3)$ transformations. This invariance is necessary to introduce the gluon fields into the theory. Detectors however never observe single quarks or gluons, since these colour charged particles appear only in colourless bound states called hadrons. These states can be subdivided into mesons (quark-antiquark pair) and baryons (three quarks). This is a consequence of the strong interaction becoming very strong at large distances. In order to keep their energy as low as possible, the quarks and gluons rearrange themselves into colourless bound states, which - as a whole - do not participate in the strong interaction.

The increase of the strong force over large distances has another consequence. Interactions between fields are usually not solvable in QFT, but they can be approximated through the use of perturbation theory, which gives the possibility to come up with predictions for the cross section of the interaction. This approximation is however only valid when the interaction is weak. At short distances, QCD can provide a perturbative description of the interactions. This however fails at larger distances, because one then enters a non-perturbative region. This is where the factorization theorem is being put to use. This theorem states that the expression for the cross section can be factorized into a perturbative part (calculable) and a non-perturbative part. The last part usually consists of collinear parton distribution functions (PDF), which give the probability of finding a parton inside a hadron. These PDFs are functions of the energy scale and the longitudinal momentum fraction of the hadron carried by the parton. Important to note is that PDFs are universal for a given hadron: if they are extracted from the measurements of one process, they can be used for obtaining predictions of another process which involves the same hadrons. The extraction from measurements only has to be done for one value of the energy scale, because the dependence of the PDFs on the energy scale is given by the Dokshitzer-Gribov-Lipatov-Altarelli-Parisi (DGLAP) equations: a set of coupled integro-differential equations. Once the expression for the PDFs is known, the factorization theorem provides the possibility to calculate the cross section of interactions involving bound states.

Physicists expected more discoveries of new particles from the collisions at the LHC. Since only the Higgs boson has been discovered at the moment, a shift has been made to obtain more precise measurements from the experiments instead of searching for mass bumps as is done for new discoveries. This causes the need for more precise predictions coming from the theoretical part. The collinear factorization theorem provides excellent results as long as there is only one scale involved in the process. When a second scale is involved, like for example the transverse momentum, the theorem breaks down. Logarithms $\log(Q^2/q_T^2)$ hereby appear in the coefficients of the perturbative expansion due to the emission of soft gluons. At low transverse momenta, higher order terms are no longer negligible and the obtained results are therefore inaccurate. These can be improved by using transverse momentum dependent (TMD) factorization.

This thesis will provide a thorough analysis of two different approaches to handle transverse momentum dependencies. The first one is the Collins-Soper-Sterman (CSS) formalism, which has already been established in the 80's for the Drell-Yan process. This process refers to the annihilation of a quark with an antiquark in hadron-hadron collisions. The formalism provides an expression for the cross section with a resummation of the large logarithms, so that a finite value for the cross section is obtained at lower values of the transverse momentum. Numerical results will also be produced and an existing program called reSolve will be used for this. It has only been developed recently and it implements the resummation procedure.

The second approach is a relatively new one and it is called the Parton Branching (PB) formalism. It provides an improvement on the Monte Carlo (MC) event generators, which are used to simulate the events from the colliders. These are usually based on the collinear factorization theorem, but this causes a mismatch because the transverse momentum is not correctly taken into account, which results in a loss of accuracy. To solve this problem, MC event generators are developed to use TMD factorization. The key element here is the TMD PDF, which is a PDF with an additional dependence on the transverse momentum. The PB method provides a technique to obtain collinear PDFs and TMD PDFs from the DGLAP equations. Numerical results for this are also generated, which will be compared to the results from the CSS formalism and experimental data from ATLAS (A Toroidal LHC Apparatus).

Both formalisms are able to provide results at varying accuracies. This is determined by the order at

which perturbative functions, that appear in the expressions, are truncated. The main goal of the thesis is to provide a systematic study of the two formalisms order per order, both analytically and numerically. Chapters 1 and 2 will provide the necessary background information needed for the two formalisms. This starts from general concepts of QCD in the first chapter and continues to obtaining the DGLAP equations by studying Deep Inelastic Scattering (DIS), an interaction between electrons and protons. Chapter 3 describes why TMD formalisms are needed and how the CSS and PB formalisms are an improvement on the collinear factorization theorem. These first chapters are based on literature that has been studied for this thesis. In Chapter 4, the two formalisms will be compared analytically by examining the Sudakov form factor, a factor that appears in both approaches but is not defined in the same way. The numerical comparison follows in Chapter 5, which contains the original work in this thesis. Results for the transverse momentum spectrum of the Drell-Yan process from both formalisms are compared. These results are produced by using different existing programs. One of those is reSolve, which has only been developed recently and is still under construction.

Part I

Theory of the strong interaction

Chapter 1

Concepts of QCD

In this chapter, some basic concepts of the strong interaction will be outlined briefly. The fundamental theory describing this interaction is QCD, which together with the theory for the weak and electromagnetic interactions forms the Standard Model. Knowledge on the strong interaction is of great importance, because these interactions appear the most in particle colliders and therefore can cause a lot of background. Through theoretical predictions, this background can be estimated so that uncommon processes can be extracted from the measurements.

The concepts of QCD explained here will come back throughout the entire thesis. For more details on the topics discussed here, one should consult [1–7].

1.1 Lagrangian and Feynman rules

QFT interprets the fundamental processes of the Standard Model as interactions between fields [6]. The elementary particles are hereby considered to be excitations of these fields and the force acting on them is represented by the exchange of a particle. Following the Lagrangian formalism, these interactions are not described classically, but instead one has to take into account all possible field configurations. This is similar to how the path integral formalism was invented from the double-slit experiment. Each field configuration is assigned a phase factor, making it possible to have destructive interference between fields that deviate too much from the classical configuration. This phase factor is proportional to the action and the field which minimizes the action, is the classical field. The action is obtained by integrating the Lagrangian density \mathcal{L} over spacetime. This density is central in QFT, because from \mathcal{L} one is able to describe the interactions between the fields completely.

The sum over all field configurations becomes an integral in the continuum limit, which causes problems. As long as the Lagrangian density is at most quadratic in the fields, the integral is solvable because it is a Gaussian integral. This Lagrangian density refers to free fields, that do not interact. Once interaction terms are present, which consist of higher powers for the fields, the integral is no longer solvable. QFT then relies on perturbation theory to still come up with an approximate solution. Usually the integrand is expanded in powers of the so-called coupling constant g , which appears in the interaction terms and depicts the strength of the interaction. In case of the electromagnetic force, this coupling constant is the electric charge e . Feynman noticed that the expansion of the integrand can be represented as propagators and vertices in a diagram, the Feynman diagram. Each power of g corresponds to a vertex and a certain amount of propagators that connect the vertices. The first two orders in g for the electron propagator are displayed in figure 1.1 as an example. The exact expressions for the propagators and vertices can be extracted from the Lagrangian density and are used to set up the Feynman rules for the theory connected to the Lagrangian density. These rules act as a manual on how to evaluate the Feynman diagrams.

In particle physics, one is mainly interested in calculating the cross section of an interaction. The cross section is defined as the number of interactions per unit of time, per target particle, per incident flux [5]. It can be considered as the probability for an interaction to happen. Although these are in general very low



Figure 1.1: Representation of the electron propagator in Feynman diagrams up to second order in perturbation theory. The lowest order does not have any vertices, while the second order has two. Source: [2]

probabilities (usually expressed in picobarn, which corresponds to $10^{-40}m^2$), the large amount of interactions produced in particle colliders provides the possibility to measure the cross section. Usually this observable is studied as a distribution of detectable kinematic variables, which is then called a differential cross section. These kinematic variables could refer to the transverse momentum of the produced state after the collision. Another possible variable is the four-momentum squared Q^2 of the exchanged boson between the interacting particles. This is often referred to as the energy scale at which the interaction takes place.

Theoretically, the cross section can be calculated using the Feynman diagrams. The interactions are usually weak enough for higher powers of g to be negligible, meaning that only the lowest order (also called tree-level) is considered for the calculation. Using the Feynman rules, the diagram provides an expression for the matrix element, which represents the probability for the interaction to take place at the fundamental level. The cross section can then be obtained by combining the matrix element with the phase space, the density of accessible states. The calculations including higher orders proceed in a similar way. This however quickly becomes challenging, because one has to take into account all possible Feynman diagrams that would contribute to the considered interaction. Furthermore, loops as displayed in figure 1.1 cause divergences, as will be shown in Section 1.2.

Fundamental processes involving the strong interaction can be calculated with the Lagrangian density for QCD ¹

$$\mathcal{L} = -\frac{1}{4}F_{\mu\nu}^a F_a^{\mu\nu} + \sum_f \bar{\psi}_f (i\not{D} - M_f)\psi_f \quad (1.1)$$

The Greek indices refer to space-time components. This Lagrangian density is able to describe the interactions between quarks and gluons. There exist six flavours f of quarks: up (u), charm (c), top (t), down (d), strange (s) and bottom (b). The first three flavours have an electric charge of $+2/3e$, the charge of the other three is $-1/3e$ (with e being the unit of electric charge). Different flavours also differ in mass and these masses are incorporated into the diagonal matrix M_f . The quark fields are represented by the Dirac spinors ψ_f . It describes the wavefunction of the quarks with four degrees of freedom, so that it would satisfy the energy-momentum conservation law. This formula then gives rise to four solutions for the wavefunction, of which two would have negative energies. Since unitarity in Quantum Mechanics forbids to discard these, physicists solved this problem by interpreting them as solutions for the wavefunctions of antiparticles. This means that interactions involving antiquarks are also included in the QCD Lagrangian.

The Standard Model is a theory which is invariant under $SU(3) \times SU(2) \times U(1)$ transformations (not considering spontaneous symmetry breaking). The $SU(2) \times U(1)$ symmetry corresponds to the theory of electroweak interactions, while $SU(3)$ is the symmetry associated with the strong interaction. The Lagrangian of QCD is constructed to be invariant under local $SU(3)$ transformations, which alter the quark wavefunctions as follows:

$$\psi_f(x) \rightarrow \psi'_f(x) = \exp \left[\frac{ig}{2} \theta_a(x) \lambda^a \right] \psi_f(x) \quad (1.2)$$

where λ^a are the eight generators of $SU(3)$ (referred to with the index a) and $\theta_a(x)$ are eight functions dependent on the space-time coordinates, which makes the transformations local. The index a runs over

¹This is not the complete Lagrangian, because it does not include the gauge-fixing terms and the ghost fields. These are not important for this thesis and are therefore left out.

these eight degrees of freedom. The generators of $SU(3)$ are represented by 3×3 -matrices (see [1] for the expressions) and for the wavefunction to be able to transform under these matrices, it has to have three additional degrees of freedom. This introduces the concept of colour, of which there are three: red, blue and green. These can be represented by three component vectors. QCD therefore describes interactions only between particles that carry a colour component. Electron fields for example do not carry the additional colour degrees of freedom, which means that they do not interact through the strong force. These fields then do not transform under $SU(3)$ operations. For the Lagrangian in (1.1) to be completely correct, the quark fields should have an additional index for the colour. A summation over these indices is then also implied.

The covariant derivative D_μ in (1.1) assures that the Lagrangian is invariant under $SU(3)$ transformations, which would not be true if a partial derivative was used instead. The introduction of eight gauge fields A_μ^a in the expression of the covariant derivative is hereby necessary:

$$D_\mu = \partial_\mu - \frac{ig}{2} A_\mu^a \lambda_a \quad (1.3)$$

where γ^μ refers to the Gamma matrices, which often appears in the Lagrangian of the Standard Model. Their expressions can be found back in [5]. The gauge fields A_μ^a correspond to eight different gluon fields, that vary in colour combination. To ensure the conservation of colour, gluons carry a combination of multiple colours, which therefore makes it possible to construct eight different colour states from red, blue and green.

Thanks to the covariant derivative, a first interaction appears in the second term of the Lagrangian in (1.1). Indeed, replacing the derivative by its expression from (1.3) gives rise to a term which is cubic in the fields, consisting of the $\bar{\psi}$, ψ and A_μ fields. This term therefore describes the interaction between two quarks and a gluon. It can be interpreted as the annihilation of a quark and antiquark, which forms a gluon, or as the emission of a gluon by a quark/antiquark.

The other QCD interactions are present in the first term of the Lagrangian. This contains the gluon field strength tensor $F_{\mu\nu}$, which is similar to the electromagnetic field tensor. However, one additional term depicts the main difference between QCD and Quantum Electrodynamics (QED), the QFT of electromagnetic interactions.

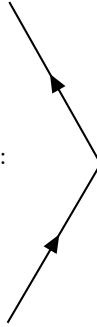
$$F_{\mu\nu} = \underbrace{(\partial_\mu A_\nu^a - \partial_\nu A_\mu^a + gf_{abc} A_\mu^b A_\nu^c)}_{F_{\mu\nu}^a} t_a \quad (1.4)$$

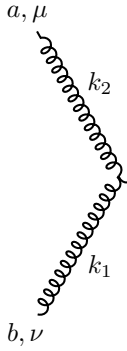
where the indices a, b, c refer to the colour component and run from 1 to 8. The third term does not appear in the electromagnetic field tensor. The symmetry associated with QED is namely $U(1)$, which in general is just a multiplication with a phase factor. In $SU(3)$, the transformation includes the eight generators of the symmetry and they do not necessarily commute with each other. This causes the appearance of the third term. The absence of this term in QED refers to the fact that photons, represented by gauge fields in the QED Lagrangian, do not interact with each other. The product of the two field strength tensors in the QCD Lagrangian however gives rise to interactions consisting of three and four gluon fields. QCD therefore states that gluons are not only emitted by quarks, but also by gluons themselves. This gluon-gluon interaction is the reason behind concepts like hadronization that are specific to QCD and do not have an analogy in QED. Section 1.3 will clarify this.

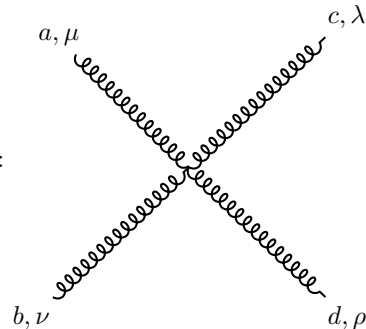
The Feynman rules for QCD processes described by the Lagrangian in (1.1) are summed up here below.

Quark propagator: $a \longrightarrow \overrightarrow{p} \longrightarrow b = \frac{i\delta_{ab}(\gamma_\mu p^\mu + m)}{p^2 - m^2}$

Gluon propagator: $a, \mu \text{ } \text{-----} \text{ } b, \nu = \frac{-i\delta_{ab}g_{\mu\nu}}{p^2}$

Quark-gluon vertex:  $= -igt_a\gamma^\mu$

Three gluons vertex: 
 $= -gf_{abc}[g_{\mu\nu}(k_1 - k_2)_\lambda + g_{\nu\lambda}(k_2 - k_3)_\mu + g_{\lambda\mu}(k_3 - k_1)_\nu]$

Four gluons vertex: 
 $= -ig^2 \left[f_{bae}f_{cde}(g_{\nu\lambda}g_{\mu\rho} - g_{\nu\rho}g_{\mu\lambda}) + f_{bde}f_{ace}(g_{\nu\mu}g_{\lambda\rho} - g_{\nu\lambda}g_{\mu\rho}) + f_{bce}f_{ade}(g_{\nu\rho}g_{\mu\lambda} - g_{\nu\mu}g_{\lambda\rho}) \right]$
Summation over e implied

1.2 Regularization and renormalization

Problems arise with calculations of processes of second order and higher. Such processes are characterized by the appearance of a loop in the Feynman diagram, as was displayed in figure 1.1. The momentum of the two particles that form the loop is not constrained to a fixed value after applying momentum conservation, leaving one free momentum parameter that one has to integrate over according to the Feynman rules. These momentum integrals are however divergent. With the use of regularization and renormalization one makes sure that the contributions from the higher order processes are finite. The details for these procedures can be found back in [2].

The loop from figure 1.1 considers a second order correction to the electron propagator through the presence of a virtual photon. This photon is called virtual, because after it has been emitted, it is being absorbed back again by the electron. The momentum k of the virtual photon can take any value, as long as the momentum of the electron in the loop is equal to $p - k$. It is this momentum k where one has to integrate over according to the Feynman rules. In the expression of the matrix element for the second order propagator, obtained after applying these Feynman rules, the following integral can be found:

$$\int d^4k \, i \left(\frac{-g_{\alpha\beta}}{k^2} \right) \gamma^\alpha i \left(\frac{\not{p} - \not{k} + m_e}{(p-k)^2 - m_e^2} \right) \gamma^\beta \sim \int dk \, k^3 \frac{k}{k^4} \sim k \quad (1.5)$$

This integral represents the self-energy correction to the electron propagator, which is another name for the second order process from figure 1.1. The integral diverges in the limit $k \rightarrow \infty$ (which is called ultraviolet (UV) divergence), meaning that the contribution from the second order processes would make the matrix element increase infinitely, which should not be the case. For perturbation theory to be valid, these corrections should be of order $\alpha = \frac{e_0^2}{4\pi}$, which is called the fine structure constant of QED. A similar parameter is present in QCD, where $\alpha_S = g^2/4\pi$. From now on, α_S will be referred to as coupling constant instead of g (unless g is explicitly mentioned). The Feynman diagrams can therefore also be considered as different orders in α_S instead of g .

To obtain finite corrections to the lowest order results, one uses regularization and renormalization. Regularization modifies the theory so that it remains finite in all orders of perturbation theory. There are many ways of achieving this. The technique used in QCD is called dimensional regularization, where the diverging integral is rewritten to a dimension $D = 4 - \eta$ instead of the usual four dimensions. Eventual divergences for $k \rightarrow 0$ that would appear here, called infrared (IR) divergences, are handled by a cut-off, of which the correct limit is taken in the end of the regularization/renormalization procedure. Besides the cut-off, the dimensional regularization introduces an extra mass scale μ to keep the natural unit dimensions of the propagator independent of η .

Regularization allows to solve integrals similar to Eq.(1.5), since the UV divergence is dealt with thanks to the change in dimensions. The results however still diverge in the limit $\eta \rightarrow 0$, which restores the expression back to four dimensions. This is where renormalization provides the solution. The concept behind this procedure is to place all singularities into non-observable quantities.

Renormalization states that the electric charge e_0 and electron mass m_e , which both appear in the QED Lagrangian, are properties of an electron that does not interact. These are called bare parameters. In QCD, this would refer to the coupling g and the quark mass m_q . Values for the mass and charge of the electron are obtained through experiments, which always involve an interacting electron and therefore the bare parameters are altered.

To obtain the relation between the measured parameters and the bare ones, the renormalization procedure first collects the singularities present for $\eta \rightarrow 0$ into so-called divergent constants. This separation can be done in multiple schemes with the same result. For QCD, the usual scheme is the 'modified minimal subtraction scheme' ($\overline{\text{MS}}$), which operates together with the dimensional regularization. The divergent constants are then absorbed into the relation between renormalized and bare parameters. The renormalized parameters are finite for $\eta \rightarrow 0$, because the bare parameters are assumed to be singular too. These cancel

out the divergent constants. Making the bare parameters divergent does not cause any inconveniences, because these parameters are never observed in experiments. The expression for the electron propagator (and similar objects) is now free of any divergences and it depends on two new parameters: the renormalized mass and charge.

1.3 Running of the strong coupling

The renormalized parameters depend on the mass scale μ , which was introduced in the dimensional regularization. The value for this scale can be chosen arbitrarily. The QCD Lagrangian in (1.1) however does not mention this scale, even though a choice must be made for μ to correctly describe the theory. Physical observables can therefore not depend on this scale. Instead, dimensionless physical observables for example will depend on the ratio Q^2/μ^2 and on the strength of the interaction, which is represented by the renormalized coupling constant $\alpha_S(\mu^2)$ in case of QCD. Q^2 is hereby the four-momentum of the exchanged boson and it acts as the energy scale for the interaction. The following analysis will show that the scale dependence of such observables can be accounted for with a coupling constant that depends on Q^2 , also referred to as a running coupling constant $\alpha_S(Q^2)$ [1].

Considering a dimensionless physical observable R , the μ independence implies:

$$\begin{aligned} \mu^2 \frac{d}{d\mu^2} R(Q^2/\mu^2, \alpha_S(\mu^2)) &= \left[\mu^2 \frac{\partial}{\partial \mu^2} + \mu^2 \frac{\partial \alpha_S(\mu^2)}{\partial \mu^2} \frac{\partial}{\partial \alpha_S(\mu^2)} \right] R(Q^2/\mu^2, \alpha_S(\mu^2)) = 0 \\ \Leftrightarrow \left[-\frac{\partial}{\partial t} + \beta(\alpha_S) \frac{\partial}{\partial \alpha_S} \right] R(e^t, \alpha_S(\mu)) &= 0 \end{aligned} \quad (1.6)$$

where the following variables were used to simplify the expression:

$$\begin{aligned} t &= \log \frac{Q^2}{\mu^2} \\ \beta(\alpha_S) &= \mu^2 \frac{\partial \alpha_S(\mu^2)}{\partial \mu^2} \end{aligned} \quad (1.7)$$

The differential equation in (1.6) can be solved by introducing the running coupling constant $\alpha_S(Q^2)$, defined as:

$$t = \int_{\alpha_S(\mu^2)}^{\alpha_S(Q^2)} \frac{dx}{\beta(x)} \quad (1.8)$$

which implies the following derivatives of $\alpha_S(Q^2)$:

$$\begin{aligned} \frac{\partial \alpha_S(Q^2)}{\partial t} &= \beta(\alpha_S(Q^2)) \\ \frac{\partial \alpha_S(Q^2)}{\partial \alpha_S(\mu^2)} &= \frac{\beta(\alpha_S(Q^2))}{\beta(\alpha_S(\mu^2))} \end{aligned} \quad (1.9)$$

These derivatives of $\alpha_S(Q^2)$ make that $R(1, \alpha_S(Q^2))$ is a solution for the differential equation in (1.6). This solution states that all scale dependence of R is contained within the running coupling constant $\alpha_S(Q^2)$, which ensures that R is independent of μ . This is not only valid for QCD, but for all theories that introduce an arbitrary scale through renormalization. In QED for example, the parameter α also becomes a function of the energy scale Q^2 .

The differential equation which determines the scale dependence is called the renormalization group equation (RGE). The RGE is characterized by the β function, which in QCD can be expanded as a series in α_S .

$$Q^2 \frac{\partial \alpha_S}{\partial Q^2} = \beta(\alpha_S) \quad (1.10)$$

with

$$\beta(\alpha_S) = -\alpha_S \sum_{n=0}^{\infty} \beta_n \left(\frac{\alpha_S}{4\pi} \right)^{(n+1)} \quad (1.11)$$

The coefficients β_n are obtained from higher order corrections to the QCD propagators and vertices. They determine the relation between the bare and renormalized parameters. One-loop corrections as the ones from figure 1.2 contribute to the β_0 coefficient, which in QCD is

$$\beta_0 = 11 - \frac{2}{3}N_f \quad (1.12)$$

with N_f equal to the amount of quark flavours in the theory. This coefficient can be considered to be the main contribution to the β function when α_S is small enough, which justifies the truncation of the expansion for β . The expression for β_0 shows two contributions that differ in sign. Negative contributions like the second term will cause the coupling constant to increase at higher energies (keeping in mind the additional minus sign from the perturbative expansion of β). These originate from loops where the gluon splits into a quark-antiquark pair, as the first diagram in figure 1.2 shows. It causes a so-called screening effect. The second diagram of figure 1.2 yields positive terms in the expression of β_0 , which cause the coupling constant to decrease at higher energies. This anti-screening effect is a consequence of gluon-loops, which contribute the most to the β_0 coefficient. Indeed, the value of β_0 is positive, since $N_f < 17$ for the Standard Model. This means that the strong coupling α_S becomes weaker at high energies. A discussion on the consequences of this follows in the next part.



Figure 1.2: Two examples of virtual corrections that provide different contributions to the β -function. The anti-screening effect is only present in QCD due to the gluon-gluon interactions.

1.3.1 Asymptotic freedom

The behaviour of the coupling constant is different in QED, but easier to interpret. Since photons do not interact with each other, there are no anti-screening contributions to the β function. The left diagram of figure 1.2 is still present in QED, since photons can for example split into an electron-positron pair. The sole contributions from the screening effect lead to a negative value of β_0 and cause the QED coupling constant α to increase at higher energies. This can be understood intuitively by considering the interaction between a photon and an electron. An electron with enough energy is able to radiate photons, similar to how quarks can radiate gluons as the QCD Lagrangian shows. These photons would then materialize into an electron-positron pair. The target electron is therefore surrounded by a cloud consisting of photons, electrons and positrons. The positively charged positrons will however be drawn towards the target electron. This will have a screening effect on the charge of the electron. Low-energy photons will not be able to pass through this barrier of positrons and therefore they would interact with a 'particle' that is less charged than the electron. High-energy photons however will be able to get closer to the target electron. The effect of the screening is less here and the interaction will therefore be stronger.

The anti-screening effect present in QCD causes the opposite behaviour of the strong coupling constant. The RGE for α_S in (1.10) implies that the coupling constant becomes weaker at higher energies. This

phenomenon is called asymptotic freedom [8]. It justifies the use of perturbation theory for calculations of the matrix element at high energies. Indeed, higher orders correspond to powers of α_S and the truncated perturbative series therefore provides a reliable prediction. These high energetic interactions are also being studied at particle colliders. The LHC for example is able to provide interactions with particles that have an energy up to 6.5 TeV [9]. It gives the possibility to compare predictions from perturbation theory with actual measurements.

1.3.2 Confinement

At longer distance scales (the equivalent of a lower energy scale, a quantum mechanical relation), the coupling increases and the interaction becomes stronger. This causes quarks and gluons to form bound states called hadrons. This process is referred to as hadronization. These hadrons have to be colourless, so that they are sterile to the strong interaction and the coupling constant stops growing. Two possible quark combinations to achieve this are a quark-antiquark pair (mesons) and a bound state consisting of three quarks/antiquarks (baryons), since the mix of a red, green and blue particle is also considered to be colourless. Theoretically, other bound states could exist, but at the moment only the mesons and baryons have been observed in experiments.

The increase in strength of the interaction at longer distance scales is called confinement and it is the reason behind the fact that quarks and gluons are never observed directly in particle colliders. This can be explained by imagining two quarks that are pulled apart from each other. This causes the strong force between them to increase, together with the potential energy corresponding to the force. At a certain point, the quarks will have enough energy and it becomes energetically favourable to create a quark-antiquark pair. These newly created particles will bound together to form hadrons, which are then detected in experiments.

The increase in strength also has implications in the theoretical study. At low energies, the coupling constant becomes too large for perturbation theory to be accurate. Contributions from higher order corrections, which are usually not included in the calculations, can now no longer be neglected. The absence of a mathematical description for lower energies makes it challenging to come up with predictions for interactions involving hadrons. Nonetheless, physicists still found a way to describe this non-perturbative part. Chapter 2 will explain one possible approach to this.

1.3.3 Λ_{QCD} parameter

One last concept of QCD that is left to explain is the Λ_{QCD} parameter. To introduce this, the RGE for α_S has to be brought up again. Assuming that the coupling constant is small enough, the expansion of the β function can be truncated at the lowest order. This gives:

$$Q^2 \frac{\partial \alpha_S}{\partial Q^2} = -\frac{\beta_0}{4\pi} \alpha_S^2 \quad (1.13)$$

The solution for this differential equation is

$$\alpha_S(Q^2) = \frac{\alpha_S(\mu^2)}{1 + \frac{\beta_0}{4\pi} \alpha_S(\mu^2) t} \quad (1.14)$$

which again shows the increase of α_S at lower energies. For an absolute value of $\alpha_S(Q^2)$, one first has to extract the value at a scale μ from experiments. As mentioned before, μ can be chosen arbitrarily, although Eq.(1.14) is only valid if α_S is small enough. Therefore to make use of this relation, the scale μ has to be chosen in the perturbative domain. Usually it is set equal to the mass M_Z of the Z boson. Figure 1.3 shows the predicted curve for $\alpha_S(Q^2)$ using $\mu = M_Z$. The data points, obtained from different experiments, show a good agreement between the measured value and the theoretical predictions.

On top of these observations, figure 1.3 shows that the value for α_S starts to diverge at low energies. Indeed, assuming that expression (1.14) also holds for lower scales, the expression contains a pole in $Q = \Lambda_{QCD}$:

$$\begin{aligned}
1 + \frac{\beta_0}{4\pi} \alpha_S(\mu^2) \log \frac{\Lambda_{QCD}^2}{\mu^2} &= 0 \\
\Leftrightarrow \Lambda_{QCD}^2 &= \mu \exp \left\{ -\frac{4\pi}{\beta_0 \alpha_S(\mu^2)} \right\}
\end{aligned} \tag{1.15}$$

An important property of Λ_{QCD} is that it does not depend on the chosen value for μ , since it is a physical parameter of the theory. The strong coupling constant will always diverge at this energy scale. The Λ_{QCD} parameter hereby indicates at which energy scales non-perturbative effects start to arise. Perturbative predictions are therefore only predictable when $Q \gg \Lambda_{QCD}$. The value for this parameter has been obtained from experiments and is approximately 200 MeV [1], which is much lower compared to the energies that particles acquire in accelerators. However, as will be discussed in the following chapters, interactions involving hadrons are spread out over multiple energy scales, which means that non-perturbative effects still have to be dealt with.

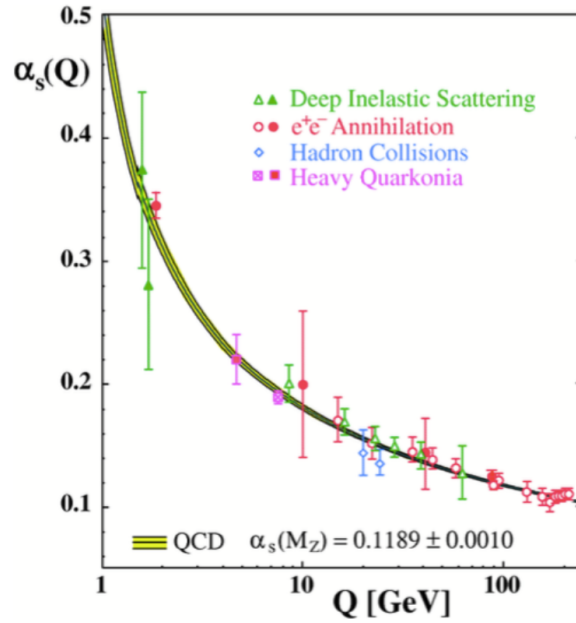


Figure 1.3: The running of the coupling constant visualized by theoretical predictions and measured values in different experiments. Source: [10]

Chapter 2

Parton distribution functions

Previous chapter mentions that the running coupling constant causes complications in QCD. At low energies, the interaction becomes too strong and it is no longer possible to use methods from perturbation theory for predictions. Quarks and gluons then form hadrons that are observed by the detectors but cannot be mathematically described. This chapter will describe how cross sections can still be calculated for experiments involving hadrons. The factorization theorem is essential here and states that the expression for the cross section can be split up into a short-distance and a long-distance part. The first part is calculable in perturbation theory. The non-perturbative behaviour is described by parton distribution functions (PDF) that portray the structure of hadrons. Although it is not possible to calculate these PDFs, their energy scale dependence can be described by the Dokshitzer-Gribov-Lipatov-Altarelli-Parisi (DGLAP) equations. These equations are used to obtain the PDFs at various energy scales, once the expression is known at an initial scale. This thesis will be concentrated on the PDFs for a proton. Predictions for processes involving these particles are of great importance, because the LHC for example generates proton-proton collisions.

Two processes for which a factorization theorem holds, will be discussed. The first one is the Drell-Yan process. It refers to the annihilation of a quark and antiquark in hadron-hadron collisions. The annihilation can produce different bosons, which decay into a lepton-pair. Experimental study of this process is important in the context of precision measurements. The second interaction involves a lepton and a hadron, called deep inelastic scattering (DIS). Even though this is a QED process at LO, higher order corrections are from QCD and experiments involving DIS have therefore been able to confirm concepts of QCD. It shows that hadrons consist of smaller particles called partons. Now it is known that these partons refer to the quarks and gluons.

2.1 Factorization

The factorization theorem provides the possibility to calculate cross sections for interactions involving hadrons. Even though these particles acquire high energies in accelerators, long-distance effects are still present in the collision.

Without a way of comparing the measured cross sections to predicted values, the LHC would have never been built. Thanks to the factorization theorem [11], this is possible and it makes the theorem very important for high energy physics. It states that the expression for the cross section σ can be factorized into short-distance behaviour $\hat{\sigma}$ and long-distance behaviour F :

$$\sigma \sim \hat{\sigma} \times F \tag{2.1}$$

The short-distance contributions refer to the hard interaction $\hat{\sigma}$, the interaction with the largest momentum exchange Q^2 . It is often referred to as the partonic cross section. Its expression is calculable with perturbation theory, because this process takes place at a short distance. The high energies acquired by the particles in accelerators ensure this. Following the Feynman rules, one is able to obtain the partonic cross

section.

The long-distance contributions F are not calculable with perturbation theory. These are represented by the PDFs, functions that give the probability of finding a parton of a certain flavour inside the hadron. The partons carry a fraction ξ of the momentum of the hadron and the probability depends on this parameter. As will be shown later in this chapter, QCD processes cause the PDFs to also depend on the energy scale Q^2 . This dependence is described by the DGLAP equations, a set of coupled integro-differential equations.

Important to note here, is that the PDFs do not depend on the interaction. They describe the internal structure of a hadron and as long the same hadrons are being considered, the PDFs are the same. Although the distributions are not calculable, their value can be extracted from detector measurements of DIS for example. Once this is done, the same PDFs can be used in calculations for other processes like Drell-Yan. Therefore, once the PDFs are known, the cross section can be calculated thanks to the factorization theorem. It is applicable for both mentioned interactions (DIS and Drell-Yan) and a short description of these interactions follows now. It will also provide an intuitive image of the factorization.

2.1.1 Deep inelastic scattering

DIS is the scattering of a lepton against a hadron. The process takes place through the exchange of a virtual boson (γ , Z , or W^\pm), that interacts with one of the partons inside the hadron. The hard interaction is therefore described by the electroweak theory. The four-momentum squared of the exchanged boson is q^2 , which has a negative value because the particle is virtual (this can be verified by simple kinematics). Therefore the energy scale Q^2 is in this case defined as $Q^2 = -q^2$. Figure 2.1 shows the Feynman diagram for DIS. The momenta depicted here will appear in several expressions.

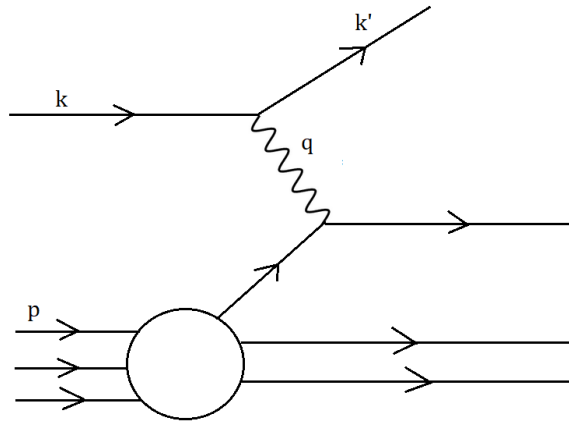


Figure 2.1: Feynman diagram of DIS. The incoming lepton carries a four-momentum k , which changes after the interaction to k' . The four-momentum of the hadron is p , which is divided over the different partons. Source: [1]

DIS can be used to provide an intuitive image of the factorization theorem. This will be described for the scattering of an electron against a proton, through the exchange of a photon. Switching to the center-of-mass (COM) frame, a coordinate system in which the center of mass remains at the same point, causes Lorentz contraction and time dilation as Special Relativity describes. The Lorentz contraction makes the hadron stretch out, as is shown in figure 2.2. The electron then has to travel over a shorter distance through the hadron. The time dilation acts upon the interactions inside the hadron. QCD processes, that change

the internal structure of the particle, now take place at a longer time scale. The time that it takes for the electron to travel through the hadron is shorter and therefore the internal structure of the hadron stays the same during the interaction. This structure is described by the PDF.

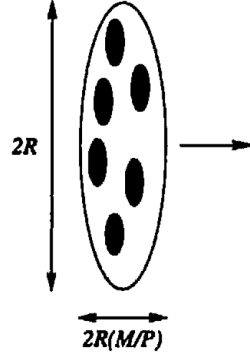


Figure 2.2: Representation of the Lorentz contraction in the COM frame. The hadron is contracted in the direction of the interaction by a factor M/p , with M referring to the mass of the hadron. Source: [1]

The probability for the DIS to happen can then actually be seen as the product between two probabilities. The first one refers to the chance of the electron-parton interaction to take place. This is the hard interaction and can therefore be described by the partonic cross section $\hat{\sigma}$, calculable with perturbation theory. The second probability is represented by the PDF $f_a(\xi)$, which gives the chance for the electron to encounter a parton with flavour a carrying a momentum fraction ξ of the hadron. The dependence of f_a on the energy scale Q^2 is being neglected for the moment. This is only valid in the limit $Q^2 \rightarrow \infty$, as will be clarified later. Together these factors combine to the cross section σ for DIS:

$$\sigma(x, Q^2) = \sum_a \int_x^1 d\xi f_a(\xi) \hat{\sigma}(x/\xi, Q^2) \quad (2.2)$$

This equation is actually the factorization theorem applied to DIS. Indeed, the expression for the cross section σ is factorized into short-distance behaviour ($\hat{\sigma}$) and long-distance behaviour (f_a).

The variable x that appears in Eq.(2.2) is called Bjorken x [12]. It is an important parameter in DIS and other processes involving hadrons because it represents the momentum fraction of the quark at the moment that it interacts with the exchanged boson. Kinematics show that the value for x is equal to $Q^2/(2p \cdot q)$ and can therefore be reconstructed from the transverse momenta, energy and scattering angles of the observed particles by the detector. Before the interaction takes place, partons have a momentum fraction $\xi \geq x$. QCD processes, like for example the emission of a gluon, will cause the momentum fraction to decrease so that the parton would contribute to $\sigma(x, Q^2)$. More on this follows in section 2.2.

2.1.2 Drell-Yan

The Drell-Yan process refers to the production of a lepton pair in hadron-hadron collisions through the annihilation of a quark and antiquark. Figure 2.3 shows the Feynman diagram for this process. The two leptons originate from the decay of the boson (γ^*, Z, W^\pm) created by the annihilation.

Emission of partons occurs throughout the whole interaction and thanks to confinement, the detectors measure these as an abundance of hadrons, called a jet. This makes it difficult to study interactions that produce strongly-interacting particles. The produced leptons in the Drell-Yan process can easily be distinguished from background hadron jets (except for neutrinos), because there is no QCD radiation from these particles. Therefore the characteristics of this interaction have been studied well. It has for example led to the discovery of the electroweak bosons.

The Drell-Yan process is still an important experiment for particle physicists nowadays. Measurements of the cross section are used to extract the mass of the W^\pm boson, which is complicated to obtain. The decay of this boson is namely always associated with the appearance of a neutrino or antineutrino, which is one of the particles of the lepton pair. Neutrinos however are not detected because they only participate in the weak interaction, making it too difficult to observe them. The four-momentum of this particle is however necessary to extract the properties of the W^\pm boson. The mass of the Z boson is for example easier to obtain, because both leptons are observed and their measurement makes it possible to reconstruct the four-momentum of the Z boson.

Precise measurements on the mass of the W^\pm boson are needed to test the Standard Model. The theory states that the mass of the W^\pm boson, the mass of the Higgs boson and the mass of the top quark are related to each other. The last two parameters have been measured precisely and therefore provide a prediction for the mass of the W^\pm boson. The Drell-Yan processes involving the photon and Z boson are used to calibrate the detector in order to measure the mass of the W^\pm boson as well as possible and to check if the relation between the masses of the three particles indeed holds.

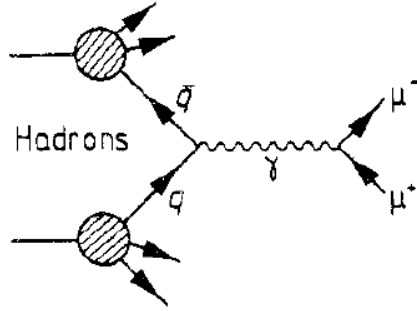


Figure 2.3: LO Feynman diagram for the Drell-Yan process. The annihilating quark and antiquark originate from two colliding hadrons, pictured by the bulb. The interaction causes the creation of a virtual photon in this case, which later splits into a lepton-antilepton pair. Source: [13]

As mentioned before, the factorization theorem also holds for the Drell-Yan process. The same intuitive description from DIS can be applied here. The main difference is that the hard interaction is now between two partons (quark and antiquark), which means that there is need for two PDFs, one for each of the interacting hadrons:

$$\frac{d\sigma}{dq_T^2}(q_T, Q, s) = \sum_{a,b} \int_0^1 dx_1 \int_0^1 dx_2 f_{a/A}(x_1, \mu_F^2) f_{b/B}(x_2, \mu_F^2) \frac{d\hat{\sigma}_{F,ab}}{dq_T^2}(q_T, Q, \hat{s}, \alpha_S(\mu_R^2), \mu_R^2, \mu_F^2) \quad (2.3)$$

Instead of the total cross section, the differential cross section is displayed here. Chapter 4 will study this expression and therefore a more detailed description of the cross section is given (compared to DIS). The cross section is now a distribution of the transverse momentum $q_T = |\mathbf{q}_T|$ of the decaying boson. By measuring the transverse momenta of the two leptons, the value for q_T can be reconstructed using momentum conservation. Figure 2.4 shows a visual representation of the collinear factorization for the Drell-Yan process. The hadron-hadron interaction is split up in three parts, that each represent contributions originating from different scales. The two PDFs f_q portray the non-perturbative region, while the partonic cross section $\hat{\sigma}$ focusses on the quark-antiquark annihilation.

Expression (2.3) contains several parameters that have not yet been mentioned previously. Q^2 is still the energy scale, which now corresponds to the four-momentum squared of the decaying boson (no additional minus sign as in DIS). The Mandelstam variable s is the COM energy for the hadron-hadron interaction, while \hat{s} represents the same for the parton-parton interaction. These two are related to each other by $\hat{s} = x_1 x_2 s$, where x_1 and x_2 are the Bjorken x for the two interacting quarks. Besides the renormalization scale μ_R ,

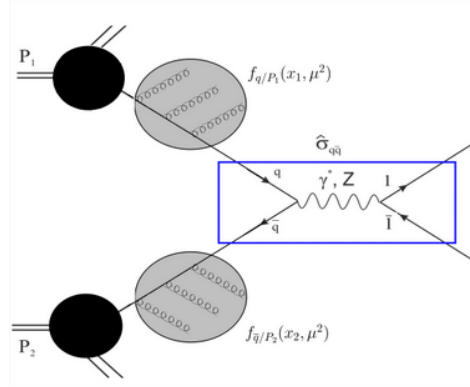


Figure 2.4: Visual representation of the collinear factorization for the Drell-Yan process. Source: [14]

another arbitrary scale μ_F appears. This is the factorization scale and its origin will be discussed in the next section.

Similarly to the DIS cross section, one factorizes the Drell-Yan cross section in short-distance behaviour and long-distance behaviour in expression (2.3). The long-distance behaviour is represented in the same way as in DIS with PDFs $f_{a/A}(x_1, \mu_F^2)$ and $f_{b/B}(x_2, \mu_F^2)$. The short-distance behaviour refers to the partonic cross section $\frac{d\hat{\sigma}_{F,ab}}{dq_T^2}$, which at lowest order is the annihilation of a quark with flavour a and a quark with flavour b . This is again calculable with perturbation theory.

Due to its importance, the Drell-Yan process will return in later chapters. Numerical results for the cross section of this interaction will be discussed in Chapter 7. For the moment, the rest of this chapter goes into more details on DIS and shows how the DGLAP equations can be obtained.

2.2 DGLAP equations

Previous section showed how the cross section for DIS can be calculated. In order to be able to do this, knowledge on the PDFs is required. This section will show that these can be obtained through structure functions, which are extracted from measurements. Furthermore, it is also important to know how the PDFs behave at different energy scales. This is described by the DGLAP equations, which can be acquired from theoretical calculations for DIS.

2.2.1 Bjorken scaling

The cross section for DIS can also be written in terms of structure functions F_1 and F_2 , that parametrize the internal structure of the nucleon as seen by the exchanged boson. Considering a proton as target hadron, the cross section is:

$$\frac{d^2\sigma}{dx dQ^2} = \frac{4\pi\alpha^2}{Q^4} \left[[1 + (1-y)^2] F_1 + \frac{(1-y)}{x} (F_2 - 2xF_1) \right] \quad (2.4)$$

with $y = \frac{1}{2}(1 - \cos\theta^*)$ and θ^* the scattering angle in the COM frame. This expression is obtained by applying a small modification to the Rosenbluth formula (see [5]). It describes the elastic scattering of an electron against a proton at an energy scale where the internal structure of the proton does not play an important role, but where one has to account for the finite size of the proton. To do this, form factors were introduced that have now been rewritten as structure functions. Originally, these form factors are related to the charge and magnetic moment distributions of the proton. In DIS, the structure functions are related to the PDFs as will be shown.

To obtain a more meaningful expression for the structure functions, the partonic cross section has to be calculated and compared to expression (2.4). Feynman rules for QED (considering only the exchange of a photon) provide the matrix element at lowest order in perturbation theory and are used to obtain the following expression for the partonic cross section $\hat{\sigma}$ ([1]):

$$\frac{d^2\hat{\sigma}}{dx dQ^2} = \frac{4\pi\alpha^2}{Q^4} [1 + (1-y)^2] \frac{1}{2} e_q^2 \delta(x - \xi) \quad (2.5)$$

The contributions from exchanging a W^\pm or Z boson can be neglected for $Q < M_W, M_Z$. The δ function implies that only partons with a momentum fraction $\xi = x$ contribute to the partonic cross section. As mentioned before, Bjorken x is the momentum fraction of the parton at the moment of the interaction. At lowest order, when no additional processes (like gluon emission) are taken into account, the momentum of the parton does not change. Therefore, the scattering only takes place against quarks with momentum fraction x .

Comparing expressions (2.5) and (2.4), the structure functions and PDFs can be related to each other by using the factorization formula (2.2):

$$\begin{aligned} F_2(x) &= 2xF_1(x) = \sum_a \int_0^1 d\xi f_a(\xi) x e_a^2 \delta(x - \xi) \\ &= \sum_a x e_a^2 f_a(x) \\ &= x \left[\frac{4}{9} (u(x) + \bar{u}(x) + c(x) + \bar{c}(x)) + \frac{1}{9} (d(x) + \bar{d}(x) + s(x) + \bar{s}(x)) \right] \end{aligned} \quad (2.6)$$

with e_a being the electric charge of a quark of flavour a . This expression for the structure functions is specific for the scattering of an electron/muon against a proton target. Similar structure functions can be defined when the target is a neutron or when the scattered lepton is a neutrino. This process takes place through the weak interaction, meaning that the exchanged boson is now a W^\pm boson.

Expression (2.6) shows that the exchanged boson sees the proton as a collection of quarks that carry a momentum fraction x . These are the only particles that interact, according to the theory at lowest order. The distribution of these quarks is given by the PDFs. The last line from (2.6) emerges from working out the sum over the flavours a . The two flavours with the largest mass are hereby neglected. This expression for the structure functions will be used later in the discussion of the measured values for these functions. These can be extracted by fitting expression (2.4) to the data.

One important result that is going to be discussed already is the fact that early measurements show no dependence on Q^2 for both structure functions. These only depend on Bjorken x , which was a fraction between Q^2 and $p \cdot q$. The structure functions seem to obey a scaling law, called Bjorken scaling. This differs from the behaviour of the form factors in the Rosenbluth formula, which become negligible small at high Q^2 due to the finite dimensions of the proton. Bjorken scaling therefore suggests that the scattering is from point-like particles that do not have smaller constituents. Increasing the resolution ($\sim 1/Q$, similar to microscopes) does not change the structure of the hadron as it is seen by the exchanged boson. Furthermore, the relation between F_1 and F_2 indicates that these point-like particles have a spin equal to $1/2$. The first observations of DIS therefore showed that protons have an internal structure, consisting of quarks.

2.2.2 Breaking of Bjorken scaling

The structure functions found in the last section did not depend on the energy scale Q^2 . This is actually only true in the limit $Q^2 \rightarrow \infty$. The strong coupling α_S is then negligible small and interactions between the partons can be disregarded (the concept of asymptotic freedom). Taking those QCD processes into account for lower values of Q^2 , the structure functions become dependent of Q^2 . The struck quark can emit a gluon before interacting with the electron or after the interaction. Gluons can split into a quark-antiquark pair, particles that participate in the DIS process. Gluons therefore also contribute to the structure functions, meaning that one expects the appearance of a gluon distribution function in the expressions for the

structure functions. The Feynman diagrams for these processes are shown in figure 2.5. The leading-order QCD corrections to the structure functions can be obtained by calculating the partonic cross sections for these diagrams using the Feynman rules for QED and QCD. Once this expression is obtained, it can again be related to the structure functions in the same way as it has been done to retrieve Eq.(2.6). The detailed calculations can be found back in [1] or [3], only the important results will be shown here.

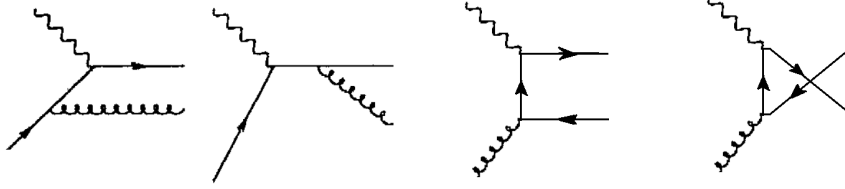


Figure 2.5: First order QCD corrections on the hard process of DIS. The exchanged boson arrives from the top left corner and interacts with the quark. This quark could emit a gluon before or after the interaction (first two pictures) or it could originate from a gluon (last two pictures).

Taking into account the diagrams from figure 2.5, the structure function becomes:

$$F_2(x, Q^2) = x \sum_a e_a^2 \int_x^1 \frac{d\xi}{\xi} \left[f_a(\xi) \delta\left(1 - \frac{x}{\xi}\right) + f_a(\xi) \frac{\alpha_S}{2\pi} \left(P_{qq}^{(0),R}(x/\xi) \log\left(\frac{Q^2}{\kappa}\right) + C_q(x/\xi) \right) + \dots \right. \\ \left. \dots + f_g(\xi) \frac{\alpha_S}{2\pi} \left(P_{qg}^{(0),R}(x/\xi) \log\left(\frac{Q^2}{\kappa}\right) + C_g(x/\xi) \right) \right] \quad (2.7)$$

The first term still represents quarks that already have a momentum fraction x before the interaction takes place. The other two terms show that the interacting quark can emerge from other quarks with a momentum fraction $\xi \geq x$ or from gluons, whose PDF is given by f_g . For these partons to contribute to $F_2(x, Q^2)$, a splitting as in figure 2.5 must occur so that the momentum fraction would drop down to x . Only then the exchanged boson would observe these contributions for an interaction characterized by x . The probability for this splitting to occur, is displayed by the splitting functions $P_{ab}(z)$. More specifically, these functions give the probability for a parton a to emerge from a splitting of parton b (where a and b are gluons and quarks of a given flavour). The parton with flavour a carries then a momentum fraction z of the momentum of the original parton. Expressions for these splitting functions are obtained by calculating the partonic cross section up to a certain order in α_S . The splitting functions in expression (2.7) represent the contributions from real-emission diagrams up to first order in α_S (displayed in figure 2.5). This explains the '(0), R' superscript for the splitting functions. As will be described later, QCD contributions of all orders in α_S have to be taken into account, including virtual (loop) diagrams. More on this will follow, including the explicit expressions for the functions.

Expression (2.7) reveals that the Bjorken scaling is broken by logarithms of Q^2 . Figure 2.6 shows that this is also observed in experiments and that the effect is largest (but still relatively small) for very low and very high x . The breaking of the Bjorken scaling can also be explained intuitively. The virtual photon has a resolution $\sim 1/Q$. Probing the proton with a high-energetic photon means that the photon can distinguish more particles inside the hadron. All those particles carry a fraction of the momentum of the proton. When more partons are observed, the proton momentum has to be distributed over more particles, meaning that there is an increase in the lower x region. The breaking of the Bjorken scaling also means that the constituents of hadron can not be described as point-like particles. This is displayed in figure 2.7. The structure of the hadron namely changes with the energy scale.

Other new variables that appear are the C functions and the cut-off κ . The C functions just collect all constant terms and terms that depend on x/ξ , showing up in the perturbative calculations of the partonic cross section. The cut-off κ was introduced in the calculations due to IR divergences. These appeared in the integration over the transverse momentum q_T for when $q_T \rightarrow 0$. The transverse momentum appears in the expression from the higher order corrections to the partonic cross section. The singularity is still present

when taking the limit $\kappa \rightarrow 0$, so this problem is not yet solved. It will now be shown how to deal correctly with this cut-off.

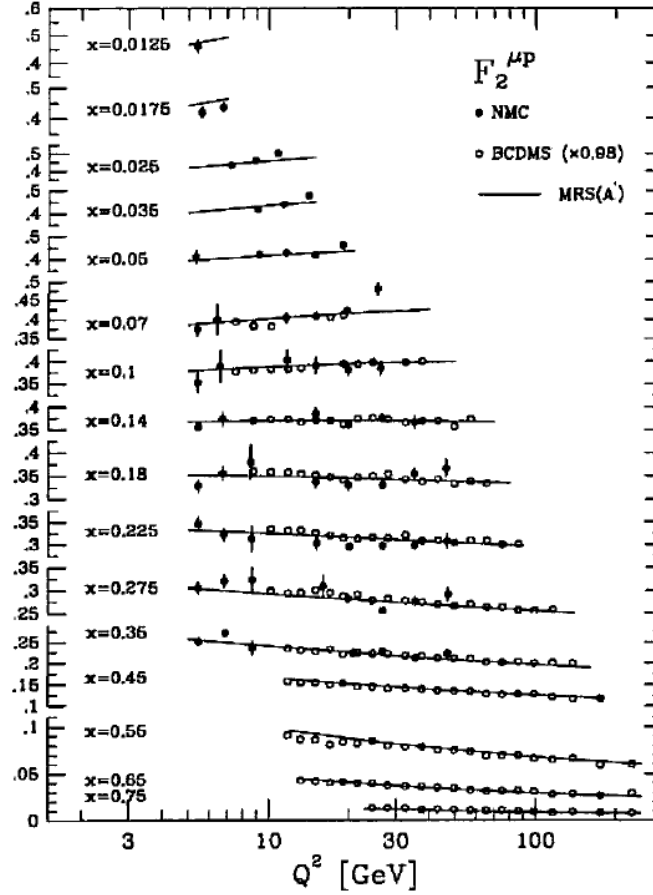


Figure 2.6: Experimental data on the structure function F_2 for muon-proton DIS. The breaking of Bjorken scaling can be observed here. The curves represent QCD predictions, the data is from the BCDMS [15] and NMO [16] collaborations. Source: [1]

2.2.3 Factorization scheme

The expression for $F_2(x, Q^2)$ in (2.7) is not completely satisfactory due to the presence of the cut-off κ . The cut-off was introduced because of a divergence that arose when $q_T \rightarrow 0$. This corresponds to an emitted gluon that is collinear with the quark and is therefore called a collinear divergence. It can be handled the same way as divergences in the electron propagator were handled in Section 1.3. Renormalized parameters were hereby introduced and the divergences were absorbed into the relation between renormalized and bare parameters. Similarly, the quark and gluon distribution functions in Eq. (2.7) can be seen as bare distribution functions $f_{a,0}(x)$ and $f_{g,0}(x)$. The renormalized distributions become dependent on a new scale μ_F , the factorization scale:

$$\begin{aligned}
 f_a(x, \mu_F^2) = & f_{a,0}(x) + \frac{\alpha_S}{2\pi} \int_x^1 \frac{d\xi}{\xi} f_{a,0}(\xi) \left(P_{qq}^{(0),R}(x/\xi) \log\left(\frac{\mu_F^2}{\kappa^2}\right) + C(x/\xi) \right) + \dots \\
 & \dots + \frac{\alpha_S}{2\pi} \int_x^1 \frac{d\xi}{\xi} f_{g,0}(\xi) \left(P_{qg}^{(0),R}(x/\xi) \log\left(\frac{\mu_F^2}{\kappa^2}\right) + C_g(x/\xi) \right) + \dots
 \end{aligned} \tag{2.8}$$

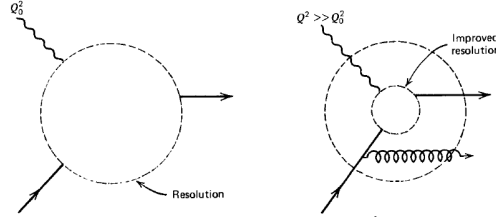


Figure 2.7: Visual representation of energy scale dependence of the structure functions. At Q_0^2 , the exchanged boson observes another quark than at Q^2 , because the quark lost energy due to the emission of a gluon. This is resolvable at Q^2 but not at Q_0^2 . Source: [3]

The divergence $\kappa \rightarrow 0$ is still present here, but because the bare PDFs are never observed, this won't give any trouble. It is common to choose the same values for the renormalization scale μ_R and μ_F , therefore these will now both be written as μ . Physical quantities like the structure function $F_2(x, Q^2)$ do not depend on μ_F , similar to the case where observables also could not depend on μ_R . The expression for $F_2(x, Q^2)$ with the renormalized PDFs becomes:

$$F_2(x, Q^2) = x \sum_a e_a^2 \int_x^1 \frac{d\xi}{\xi} \left[f_q(\xi, \mu^2) \left(\delta(1 - \frac{x}{\xi}) + \frac{\alpha_S}{2\pi} P_{qq}^{(0),R}(x/\xi) \log\left(\frac{Q^2}{\mu^2}\right) + \dots \right) + \dots \right. \\ \left. \dots + f_g(\xi, \mu^2) \left(\frac{\alpha_S}{2\pi} P_{qg}^{(0),R}(x/\xi) \log\left(\frac{Q^2}{\mu^2}\right) + \dots \right) \right] \quad (2.9)$$

Choosing $\mu^2 = Q^2$, which one can do since μ is an arbitrary scale, makes the logarithms disappear and gives:

$$F_2(x, Q^2) = x \sum_a e_a^2 f_a(x, Q^2) \quad (2.10)$$

This relation between the structure functions and the PDFs has appeared before in Eq.(2.6). However, that result was obtained in the $Q^2 \rightarrow \infty$ limit. The expression in (2.10) shows that a similar results still holds, after taking QCD processes into account. As mentioned before, structure functions can be obtained from fits with experimental data, which then can provide an expression for the PDFs.

The renormalized PDFs from expression (2.8) absorbed the two C functions, which are finite contributions. The way that finite contributions are treated is arbitrary and depends on the choice of the factorization scheme. The PDFs from expression (2.8) refer to the DIS scheme, which has the benefit that $F_2(x, Q^2)$ can be written simply as in Eq.(2.10). Another frequently used factorization scheme is the $\overline{\text{MS}}$ scheme. There the PDFs only absorb the divergent term together with a $(\log 4\pi - \gamma)$ contribution. The structure function F_2 then looks like:

$$F_2(x, Q^2) = x \sum_a e_a^2 \int_x^1 \frac{d\xi}{\xi} \left[f_a(\xi, \mu^2) \left(\delta(1 - \frac{x}{\xi}) + \frac{\alpha_S}{2\pi} C_q^{\overline{\text{MS}}}(x/\xi) + \dots \right) + \dots \right. \\ \left. \dots + f_g(\xi, \mu^2) \left(\frac{\alpha_S}{2\pi} C_g^{\overline{\text{MS}}}(x/\xi) + \dots \right) \right] \quad (2.11)$$

The expressions for $C_q^{\overline{\text{MS}}}(x/\xi)$ and $C_g^{\overline{\text{MS}}}(x/\xi)$ can be found in [1]. An important remark here is that if for example PDFs are obtained through Eq.(2.10) from DIS experiments, that they can only be used in the theoretical calculations of other factorized theories if the same factorization scheme was applied in these calculations.

2.2.4 Evolution equations

The PDFs that appear in the expression for the structure function $F_2(x, Q^2)$ are not calculable with perturbation theory because they illustrate long-distance behaviour. It is however possible to determine how

the PDFs depend on the factorization scale μ . The structure function $F_2(x, Q^2)$ does not depend on this scale, so the $\frac{\partial}{\partial \log \mu^2}$ derivative of expression (2.9) should be equal to zero. This is similar to how the running coupling constant was introduced in Chapter 1. The derivative yields:

$$\mu^2 \frac{\partial}{\partial \mu^2} f_a(x, \mu^2) = \frac{\alpha_S(\mu^2)}{2\pi} \int_x^1 \frac{d\xi}{\xi} \left[P_{qq}^{(0),R}(x/\xi) f_a(\xi, \mu^2) + P_{qg}^{(0),R}(x/\xi) f_g(\xi, \mu^2) \right] \quad (2.12)$$

This is the RGE for the quark distribution functions and it is called the DGLAP equation. It serves the same purpose as the RGE for the strong coupling $\alpha_S(\mu^2)$ in Eq.(1.10). When the PDFs are known at a certain scale μ_0^2 (obtained through experimental data), they can be acquired at any other scale with the DGLAP equation.

With the probabilistic property of the splitting functions, this equation is easy to interpret. The amount of quarks with a momentum fraction x grows for increasing μ thanks to two sources. The first one are quarks of the same flavour with momentum fraction ξ that obtain a momentum fraction x by emitting a gluon. The second contribution comes from gluons that split into a quark-antiquark pair, where the quark has a momentum fraction x . By using the same logic, it is also possible to construct a similar equation for gluon distribution functions:

$$\mu^2 \frac{\partial}{\partial \mu^2} f_g(x, \mu^2) = \frac{\alpha_S(\mu^2)}{2\pi} \sum_a \int_x^1 \frac{d\xi}{\xi} \left[P_{gq}(x/\xi) f_a(\xi, \mu^2) + P_{gg}(x/\xi) f_g(\xi, \mu^2) \right] \quad (2.13)$$

2.2.5 Splitting functions

The DGLAP equation for the PDFs in expressions (2.12) only takes leading-order real-emission contributions into account at the moment. When QCD processes of all orders are considered, including virtual emissions, the splitting functions can be written as a perturbative expansion in α_S .

$$P_{qq}(z, \alpha_S) = \frac{\alpha_S}{2\pi} P_{qq}^{(0)}(z) + \left(\frac{\alpha_S}{2\pi}\right)^2 P_{qq}^{(1)}(z) + \dots \quad (2.14)$$

The other splitting functions have similar expansions. The strong coupling α_S depends on the renormalization scale μ , therefore the splitting functions will also depend on this scale. For completeness, the coefficients of the splitting functions at leading-order are given here.

$$\begin{aligned} P_{qq}^{(0)}(z) &= \frac{4}{3} \frac{1+z^2}{(1-z)_+} + 2\delta(1-z) \\ P_{qg}^{(0)}(z) &= \frac{1}{2} (z^2 + (1-z)^2) \\ P_{gq}^{(0)}(z) &= \frac{4}{3} \frac{1+(1-z)^2}{z} \\ P_{gg}^{(0)}(z) &= 6 \left[\frac{z}{(1-z)_+} + \frac{1-z}{z} + z(1-z) \right] + \delta(1-z) \frac{33-2n_f}{6} \end{aligned} \quad (2.15)$$

The plus-prescription used here is defined for an arbitrary function $f(z)$ as:

$$\int_0^1 dz \frac{f(z)}{(1-z)_+} = \int_0^1 dz \frac{f(z) - f(1)}{1-z} \quad (2.16)$$

Splitting functions at higher orders become more complicated. For example, the quark splitting function doesn't require any longer that the initial and final quark are the same flavour. At next-to-leading-order, a charm quark could for example emit a gluon that splits into an $u\bar{u}$ -pair. This means that the DGLAP equation from expression (2.12) needs a slight modification for it to be true for all orders in perturbation theory:

$$\mu^2 \frac{\partial}{\partial \mu^2} f_a(x, \mu^2) = \sum_b \int_x^1 \frac{d\xi}{\xi} P_{ab}(x/\xi, \mu^2) f_b(\xi, \mu^2) \quad (2.17)$$

The indices a and b run over all quark flavours and the gluon. Note that the factor $\alpha_S/2\pi$ from Eq.(2.12) is now absorbed into the definition of the splitting functions in Eq.(2.14). Expression (2.17) combines therefore the two DGLAP equation in (2.12) and (2.13) and it takes into account all orders of perturbation theory.

Usually the PDFs are parametrized at a starting energy scale Q_0^2 and fitted to data corresponding to this scale. The DGLAP equations, with the splitting functions truncated at a fixed order, can then be used to obtain PDFs at other energy scales. The DGLAP equations are therefore of great importance for the PDF fits.

2.2.6 Momentum sum rule

An important identity for the splitting functions arises if one requires that the total momentum of the proton is carried by the quarks and gluons. This can be written as:

$$\sum_a \int_0^1 dx x f_a(x, \mu^2) = 1 \quad (2.18)$$

The expression is valid for all values of μ^2 . Using this property, the momentum sum rule is obtained:

$$\sum_{q_i} \int_0^1 dz z P_{q_i q_j}(z, \mu^2) = 0 \quad (2.19)$$

The complete calculation can be found back in [14]. This momentum sum rule represents the conservation of momentum in the parton splitting. The expression will return in Chapter 5, where an approach to solve the DGLAP equations will be portrayed. The momentum sum rule will hereby be used to deal with virtual contributions.

2.2.7 Related experimental results

To give a final remark on the structure functions, expression (2.6) is brought up again. It shows the relation between the PDFs and the structure functions for the electron-proton DIS, where QCD interactions have been neglected. As has been mentioned before, expressions for the structure functions of other interacting particles can be obtained similarly. These can also be extracted from measurements of the corresponding cross sections. Some of the interesting results are given here. Only u and d quarks are considered for simplicity.

- The structure function $F_3^{\nu N}$, present in the cross section for neutrino-nucleon (ν - N) DIS, indicates the amount of valence quarks found in a proton/neutron target. Valence quarks are defined as the difference $u(x) - \bar{u}(x)$ and similarly for other flavours.

$$\begin{aligned} I &= \int_0^1 F_3^{\nu N}(x) dx = \int_0^1 [u(x) + d(x) - \bar{u}(x) - \bar{d}(x)] dx \\ &= \int_0^1 [u_V(x) + d_V(x)] dx \end{aligned} \quad (2.20)$$

This is called the Gross-Llewellyn-Smith (GLS) sum rule [17]. Up to lowest order in perturbation theory, one expects this value to be equal to three since a proton consists of two u and one d quarks. However, Section 2.2.2 showed that Bjorken scaling is broken and that the structure functions depend on the energy scale. This implies that the GLS sum I is also a function of the energy scale Q^2 and that it can be written as:

$$I(Q^2) = 3 \left[1 + d_1 \frac{\alpha_S(Q^2)}{\pi} + d_2 \left(\frac{\alpha_S(Q^2)}{\pi} \right)^2 + \dots \right] \quad (2.21)$$

Expressions for the d_n coefficients can be found back in [1]. At $Q^2 = 3 \text{ GeV}^2$, its value is 2.50, obtained from measurements of the neutrino-nucleon DIS cross section [18]. It shows that the proton has a more complicated structure and that it does not just consist of three quarks.

- The structure functions for an electron-neutron scattering can be obtained easily by using isospin symmetry. This approximate symmetry tells that the difference in mass between the u and d quark can be neglected. The only difference between these particles is then their electric charge. In the structure functions F_2^{ep} of (2.6) one simply has to swap the $u(x)$ and $d(x)$ distributions to obtain the F_2^{en} structure functions, because those distributions are switched when considering a neutron instead of a proton.

$$F_2^{en}(x) = x \left[\frac{4}{9} (d(x) + \bar{d}(x)) + \frac{1}{9} (u(x) + \bar{u}(x)) \right] \quad (2.22)$$

One has to keep in mind that the quark distributions $f_a(x)$ are always defined for a proton, even in the expression for F_2^{en} . The difference between F_2^{ep} and F_2^{en} integrated over x gives the Gottfried sum rule [19]:

$$\begin{aligned} \int_0^1 \frac{1}{x} [F_2^{ep}(x) - F_2^{en}(x)] dx &= \frac{1}{3} \int_0^1 [u(x) + \bar{u}(x) - d(x) - \bar{d}(x)] dx \\ &= \frac{1}{3} \int_0^1 [u_V(x) + 2\bar{u}(x) - d_V(x) - 2\bar{d}(x)] dx \\ &= \frac{1}{3} + \frac{2}{3} \int_0^1 [\bar{u}(x) - \bar{d}(x)] dx \end{aligned} \quad (2.23)$$

Experiments show that the value for this expression is 0.235 ± 0.026 [20], which is another indication that protons/neutrons do not solely consist of three quarks. It also shows that there is a difference in the amount of \bar{u} and \bar{d} quarks inside a proton. The origin of this asymmetry could be assigned to the fact that more u states than d states are occupied in a proton, which causes the creation of a $d\bar{d}$ pair to be favoured.

- The final result that is going to be discussed is the $F_2^{\nu N}$ function, another structure function that appears in the cross section for neutrino-nucleon DIS. Integrating this over x gives the total momentum fraction carried by quarks and antiquarks:

$$\int_0^1 F_2^{\nu N}(x) dx = \int_0^1 x [u(x) + \bar{u}(x) + d(x) + \bar{d}(x)] dx \quad (2.24)$$

The measured value for this is approximately 50%. It shows that the quarks do not carry all the momentum. Half of it is carried by the gluons, which were not present in the calculations for expression (2.6).

2.3 Event generators

It has become clear now that hadrons do not simply consist of two or three quarks. These quarks can continuously emit gluons, which at their turn can split into multiple gluons or a quark-antiquark pair. This constant branching is also present in collider experiments. Detectors at colliders involving hadrons therefore have to deal with a large amount of particles. These are all colourless due to confinement, that cause the hadronization of each parton.

The continuous parton branching makes it challenging to do the calculations for the cross section manually. The hadronization process is not even possible to describe with perturbation theory since it represents long-distance behaviour. Therefore, physicists use so-called Monte Carlo (MC) event generators to obtain predictions for cross sections [21, 22]. They reconstruct the processes that occur in collision experiments numerically with MC techniques. These techniques involve mathematical methods to solve integrals and generate variables. Integrals that are complicated to solve, appear in the calculations of the cross section.

MC integration can handle these by generating random values for the variables first, which are then evaluated by the integrand. This is done a large amount of times and the integrands are summed over. Dividing this result by the amount of generated numbers provides an approximate solution for the integral.

Due to the abundance of partons, multiple interactions will find place in collisions involving hadrons. MC event generators handle these by working in three parts. First there is the hard interaction. The expression for the partonic cross section can be calculated with perturbation theory up to a certain order in α_S . To evaluate this expression, values for the variables on which it depends (like Q) are randomly generated according to a distribution. This distribution is provided by the PDFs.

Next the event generator proceeds to take into account real-emission corrections. This happens through the simulation of a so-called parton shower. These consist of multiple parton branching, where flavour and four-momentum are conserved. Besides that, the only other condition on the branching is that unitarity is also taken into account, which means that the sum of the probabilities for a parton to branch or not to branch should be equal to one. The branching can occur before the hard process (initial-state branching) or afterwards (final-state branching). The parton shower simulation can then be accomplished by using the splitting functions that appear in the DGLAP equations, since these functions represent the probability for a parton to undergo branching. More information can be found in Chapter 5, which describes a new sort of MC event generator. The general idea behind parton showers is first illustrated before it is extended by the new method.

The original final state of the hard process is now expanded by additional partons from initial-state and final-state branching. The last effect that the MC event generator has to take into account, is the hadronization of the particles produced in the parton shower and the hard interaction. This is accomplished by using hadronization models, but a more detailed description on how the MC event generators treat this can be found back in [21,22]. This is not important for the further course of the thesis. MC event generators will be used in Chapter 7, but the hadronization will not be necessary. The reason is that the cross section of the Drell-Yan process will be studied here. The hard interaction produces a pair of leptons, which are colourless and do not hadronize. Additional particles that are obtained in the final state, originating from the parton shower, are considered to be unmeasured.

Part II

TMD formalisms

Chapter 3

TMD factorization

3.1 Introduction

Previous chapter showed how the factorization theorem can be used to calculate the cross section of DIS and the Drell-Yan process. It was hereby assumed that the partons were collinear with the proton, meaning that they do not have any transverse momentum k_T with respect to the forward motion of the proton. The theorem is therefore also called collinear factorization. The use of collinear factorization proved to be very successful. There is an excellent agreement between theoretical predictions and measured data for processes that are characterized by a single scale (like for example Q^2 in DIS).

Collinear factorization however reaches its limits for processes where multiple scales are involved. An example that will be studied in this thesis is the differential cross section of the Drell-Yan process as function of the transverse momentum q_T of the created Z boson. It is not possible to obtain accurate predictions on the lower part of the spectrum with collinear factorization, as will be discussed in this chapter. In order to solve this, the low q_T factorization has been introduced.

Another problem that arises with collinear factorization, is a large uncertainty on the PDFs in the low x regime. The longitudinal momentum of the partons is hereby too small for the transverse momentum to be negligible. The high-energy factorization therefore introduces the transverse momentum dependent (TMD) PDFs, which extends the PDFs with an additional dependence on the transverse momentum of the partons in order to improve the accuracy.

This section provides a portrayal of the problems that arise with collinear factorization and how the low q_T and high-energy factorization propose to solve them. These two are examples of so-called TMD factorizations. Section 3.2 will describe the low q_T formalism more thoroughly. The high-energy factorization will not be directly studied in this thesis. Instead, Section 3.3 will focus on a recently developed approach to obtain TMD PDFs.

3.1.1 Low q_T factorization

The low q_T factorization is described by the Collins-Soper-Sterman (CSS) formalism [23]. This theorem is only valid for $q_T \ll Q$ and was originally formulated for the Drell-Yan process. This process offers a great opportunity to test the Standard Model by studying the transverse momentum distribution of the electroweak bosons in hadron-hadron collisions. More specifically, it can verify QCD predictions because the annihilating quarks acquire transverse momentum through the splitting of the partons, as was described in Section 2.2.2. Without this, the quarks would not have transverse momentum and neither would the bosons.

Applying the collinear factorization theorem however causes problems in the perturbative calculation of the partonic cross section, which is not integrated over q_T now so that the q_T distribution can be obtained.

The expression for the Drell-Yan cross sections has already been mentioned in Section 2.1.2 (Eq.(2.3)). To clarify where the theorem breaks down, the expression is given again here:

$$\frac{d\sigma}{dq_T^2}(q_T, Q, s) = \sum_{a,b} \int_0^1 dx_1 \int_0^1 dx_2 f_{a/A}(x_1, \mu_F^2) f_{b/B}(x_2, \mu_F^2) \frac{d\hat{\sigma}_{F,ab}}{dq_T^2}(q_T, Q, \hat{s}, \alpha_S(\mu_R^2), \mu_R^2, \mu_F^2) \quad (3.1)$$

At LO, the partonic cross section does not contain any q_T dependence. This is only present from NLO, where the initial parton can split and obtain transverse momentum. The NLO expression however diverges for $q_T \rightarrow 0$. In general, the higher order expressions contain $\alpha_S^n \log^m(Q^2/q_T^2)$ terms, with $1 \leq m \leq 2n$, in all orders of the coupling constant. For large q_T , the collinear factorization stays valid. For small q_T , the logarithmic coefficients become too large and higher order terms in the expansion are no longer of order α_S^n . Neglecting these will therefore cause a large uncertainty on the theoretical prediction.

The perturbative calculations show that the emission of low-energetic (soft) gluons leads to the appearance of the logarithms in the expansion. The fact that it appears at every order in α_S means that the emission can contain an arbitrary amount of gluons and that they all need to be taken correctly into account. It won't suffice to only regulate the NLO term for example. It is also these emissions that cause the Z boson to have a low transverse momentum. The energy of a single soft gluon is negligible small, but the cumulative gain in transverse momentum of the annihilating quark by emitting an arbitrary amount of these gluons causes the low q_T of the Z boson.

The CSS formalism takes emission of an arbitrary amount of soft gluons into account through resummation of the large logarithms up to all orders in α_S . It actually factorizes the expression for the partonic cross section into functions that each represent contributions from different scales. The resummation is hereby performed through exponentiation. This TMD factorization will be discussed further in Section 3.2.

3.1.2 High-energy factorization

The second TMD factorization is k_T -factorization [26], which is valid for $s \rightarrow \infty$ and arbitrary values for the transverse momentum. This focusses more on the PDFs than on the expression for the cross section. With the inauguration of the LHC, physicists were able to study particle interactions at higher COM energy s compared to other colliders. This increase in s however means that more of the hadron structure can be resolved in the interaction, which leads to an increase of the PDFs at low x (see Section 2.2.2). More specifically, the momentum fraction x is related to the COM energy as ($\sim 1/s$) at a fixed energy scale. Precise predictions at low x are thus needed. The collinear factorization is not able to provide them, because the transverse momentum of the parton is no longer negligible compared to the low longitudinal momentum.

Figure 3.1 shows the gluon density as function of x . These were obtained from fits, performed at LO, NLO and NNLO of the DGLAP equations. The plot shows that there is a large uncertainty on the PDF for low values of x . This uncertainty is again a consequence of neglecting higher order terms, which are not small for high s . These contain namely powers of $\log(\sqrt{s}/Q)$, caused again by the emission of soft gluons.

The k_T -factorization provides a resummation of the large logarithms. Similarly to collinear factorization, it factorizes the cross section into the partonic cross section and the PDFs. For the Drell-Yan process, this can schematically be displayed as:

$$\sigma = \sum_{q\bar{q}} \int d^2\mathbf{k}_{T,1} d^2\mathbf{k}_{T,2} \int dx_1 dx_2 \mathcal{A}_q(x_1, \mathbf{k}_{T,1}, \mu^2) \mathcal{A}_{\bar{q}}(x_2, \mathbf{k}_{T,2}, \mu^2) \hat{\sigma}_{q\bar{q}}(x_1, x_2, \mathbf{k}_{T,1}, \mathbf{k}_{T,2}, \mu^2) \quad (3.2)$$

The PDFs \mathcal{A}_q now have an additional dependence on the transverse momentum of the parton. These are from now on called TMD PDFs and they are related to the collinear PDFs as

$$f_a(x, \mu) = \int d^2\mathbf{k}_T \mathcal{A}_a(x, \mathbf{k}_T, \mu) \quad (3.3)$$

Therefore TMD PDFs are also often called unintegrated PDFs. The partonic cross section $\hat{\sigma}_{q\bar{q}}$ from expression (3.2) is again calculable with perturbation theory and also acquires a k_T -dependence. This was not

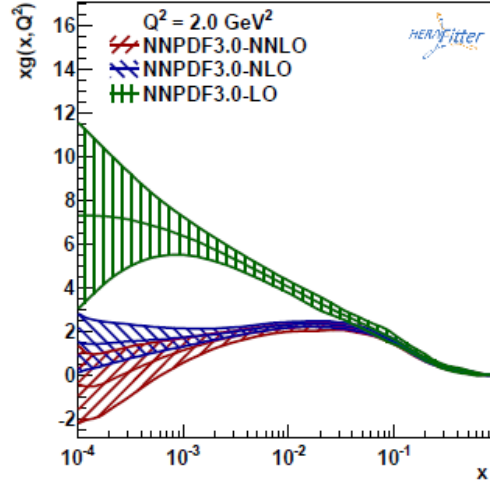


Figure 3.1: The gluon distribution function obtained from global fits to the data [27]. Source: [25]

present in the collinear factorization, because the partonic cross section was integrated over the transverse momentum (which caused an IR divergence, see Section 2.2.3). For numerical calculations, a matching scale is usually introduced to divide the q_T spectrum into a part where the TMD PDFs dominate (low q_T) and a part where the partonic cross section dominates (high q_T). This has to be done to avoid double counting, since both factors take into account the k_T -dependence.

In section 3.3, a recently developed approach, called the Parton Branching (PB) method, is described that aims on using the high-energy factorization in MC event generators. As will be explained, TMD PDFs are needed for this and the PB method provides a way of obtaining them from the DGLAP equations. This procedure is not necessarily related to the high-energy factorization because the obtained TMD PDFs are valid over a broad range in kinematics, from low energies to high energies.

3.2 CSS formalism

The resummation procedure has been set up by Collins, Soper and Sterman [23]. They have described how the partonic cross section can be written in terms of perturbative functions that resum the large logarithms. Their result had been determined for the Drell-Yan process, but it can be easily converted into a general form for inclusive hard-scattering processes, for which the expression in Eq.(3.1) is also valid. This has been done in [28, 29] and these papers will be followed in this section. Inclusive hard-scattering processes hereby refer to interactions that can be described as

$$h_1(p_1) + h_2(p_2) \rightarrow F(Q, q_T) + X \quad (3.4)$$

where F is the final state that one studies, like the lepton pair in the case of the Drell-Yan process. It could also consist of vector bosons, Higgs particles or other non-strongly interacting systems. The gluon-gluon fusion process is for example the main source of Higgs bosons in hadron colliders at LHC energies, which gives another reason to try and understand these processes thoroughly from a theoretic point of view. The inclusive description refers to the fact that the other final state X is left unmeasured. In case of the Drell-Yan process, this refers to the jet of hadrons that is produced together with the lepton pair.

3.2.1 Resummation

The resummation procedure is set up in terms of the impact parameter $b = |\mathbf{b}|$, which is the Fourier transform of the transverse momentum q_T . The low transverse momentum of the boson is caused by the emission of

n soft gluons with transverse momentum k_T and the formulation in b -space provides a proper treatment of the conservation of the transverse momentum. In transverse momentum space, this is represented by a sum inside a δ function. Calculating the Fourier transformation gives an expression that is more straightforward to solve [1]:

$$\delta^{(2)}\left(\sum_{i=1}^n \mathbf{k}_{T,i} - \mathbf{q}_T\right) = \frac{1}{(2\pi)^2} \int d^2\mathbf{b} e^{-i\mathbf{b}\cdot\mathbf{q}_T} \prod_{i=1}^n e^{i\mathbf{b}\cdot\mathbf{k}_{T,i}} \quad (3.5)$$

The CSS formalism then provides the following expression for the hadronic cross section:

$$\frac{d\sigma_F}{dq_T^2}(q_T, Q, s) = \frac{Q^2}{s} \int_0^\infty d^2\mathbf{b} \frac{e^{i\mathbf{b}\cdot\mathbf{q}_T}}{4\pi^2} W^F(b, Q, s) + \frac{d\sigma_F^{(\text{fin})}}{dq_T^2}(q_T, Q, s) \quad (3.6)$$

with

$$\begin{aligned} W_N^F(b, Q) &= \sum_c \sigma_{c\bar{c},F}^{(0)}(\alpha_S(Q^2), Q^2) H_c^F(\alpha_S(Q^2)) S_c(Q, b) \\ &\times \sum_{a,b} C_{ca,N}(\alpha_S(b_0^2/b^2)) C_{\bar{c}b,N}(\alpha_S(b_0^2/b^2)) f_{a/A,N}(b_0^2/b^2) f_{b/B,N}(b_0^2/b^2) \end{aligned} \quad (3.7)$$

This expression can be obtained from the collinear factorization formula in Eq.(3.1) by dividing the expansion of the partonic cross section into regular terms and terms that are singular for $q_T \rightarrow 0$ (containing the large logarithms). The lowest order term is represented by $\sigma^{(0)}$ in the expression above. The regular terms are collected in the $\sigma_F^{(\text{fin})}$ term, which dominates for large q_T ($q_T \sim Q$). The singular terms are gathered together into the W_N^F function and provide the largest contributions for low q_T ($q_T \ll Q$). In the transition from lower to higher values of q_T , one has to apply a matching procedure between the two terms to guarantee a correct result. This will be briefly described at the end of the chapter.

Scale invariance of the hadronic cross section implies a RGE for the W_N^F function, similar to how the running coupling α_S was obtained by applying scale invariance of R in Section 1.3. Solving this RGE leads to the appearance of an exponent S_c containing the problematic logarithm. In b -space, this is $\log(Q^2 b^2)$ and the complications appear for $b \rightarrow \infty$. This exponent is called the Sudakov form factor and it contains the resummation of the logarithms. Indeed, the expansion of e^x contains all powers of x and S_c will therefore include all powers of the logarithm. The explicit expansion of S_c will briefly be portrayed later in this section. The remaining functions C_{ab} and H_c^F represent other contributions, as will also be made clear in this section.

Besides changing to b -space, the CSS formalism also prefers to work with the Mellin moments of certain functions. In expression (3.7), the benefit of using the Mellin moments is that the integrals over the momentum fractions, appearing in the C_{ab} functions and the PDFs f_a and f_b , are now replaced by a product between these functions, which is computationally easier to solve. The definition for the Mellin moment is:

$$\mathcal{W}_N^F(b, Q, \alpha_S(\mu_R^2), \mu_R^2, \mu_F^2) = \int_0^1 dz z^{N-1} \mathcal{W}_N^F(b, Q, \hat{s}, \alpha_S(\mu_R^2), \mu_R^2, \mu_F^2) \quad (3.8)$$

Moments of other functions that appear, are defined in the same way.

The functions appearing in (3.7) represent contributions to the partonic cross section coming from different transverse momentum scales, as is shown in figure 3.2. Since it is assumed that the created boson has a negligible transverse momentum, only soft and collinear radiation are being considered. The scale $q_T \sim Q$ refers to the hard process itself (quark-antiquark annihilation, gluon-gluon fusion). The only QCD corrections at this scale are virtual, which are contained in the H_c^F function. At the scale $q_T \leq 1/b$, the real and virtual contributions from the collinear radiation are comprised within the C_{ab} functions. The Sudakov form factor S_c takes into account contributions from processes occurring at the scale $Q \geq q_T \geq 1/b$. It provides the real and virtual contributions from soft partons and it also contains the flavour-conserving part of the collinear radiation. The explicit expression for S_c is

$$S_c(Q, b) = \exp \left\{ - \int_{b_0^2/b^2}^{Q^2} \frac{dq^2}{q^2} \left[A_c(\alpha_S(q^2)) \log \frac{Q^2}{q^2} + B_c(\alpha_S(q^2)) \right] \right\} \quad (3.9)$$

The notation (no index F) implies that the Sudakov form factor is universal, meaning that it is process independent. It only differs for quarks and gluons. The same applies for the C_{ab} functions, which only depend on the type of parton.

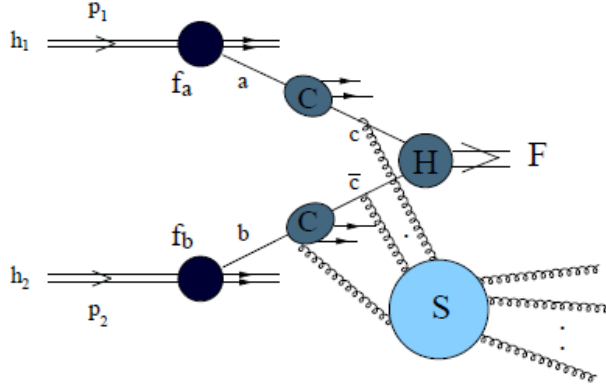


Figure 3.2: Visual representation of the different functions that appear in expression (3.7). Source: [28]

The PDFs still represent the non-perturbative region of the phase space, while the other functions represent contributions at transverse momentum scales that are large enough for perturbation theory. The functions A_c , B_c , C_{ab} and H_C^F all have a perturbative expansion in α_S :

$$\begin{aligned} A_c(\alpha_S) &= \sum_{n=1}^{\infty} \left(\frac{\alpha_S}{\pi} \right)^n A_c^{(n)} \\ B_c(\alpha_S) &= \sum_{n=1}^{\infty} \left(\frac{\alpha_S}{\pi} \right)^n B_c^{(n)} \\ C_{ab}(\alpha_S, z) &= \delta_{ab} \delta(1-z) + \sum_{n=1}^{\infty} \left(\frac{\alpha_S}{\pi} \right)^n C_{ab}^{(n)}(z) \\ H_c^F(\alpha_S) &= 1 + \sum_{n=1}^{\infty} \left(\frac{\alpha_S}{\pi} \right)^n H_c^{F(n)} \end{aligned} \quad (3.10)$$

By working out the integral from (3.9), it becomes clear how the all-order resummation of the soft gluons is provided by the exponent. First, the running of $\alpha_S(q^2)$ from Eq.(1.10) has to be used to change the variable inside the coupling constant. This evolution is given by the β -function (see Section 1.3):

$$\begin{aligned} \frac{d \log(\alpha_S(q^2))}{d \log q^2} &= \beta(\alpha_S(q^2)) = - \sum_{n=0}^{\infty} \beta_n \alpha_S(q^2)^{n+1} \\ \Leftrightarrow \alpha_S(q^2) &= \frac{\alpha_S(Q^2)}{l} - \left(\frac{\alpha_S(Q^2)}{l} \right)^2 \frac{\beta_1}{\beta_0} \log l + \dots \end{aligned} \quad (3.11)$$

where

$$l = 1 + \beta_0 \alpha_S(Q^2) \log \left(\frac{q^2}{Q^2} \right) \quad (3.12)$$

The integration variable q^2 now only appears in the function l and no longer in the coupling constant. The Sudakov form factor can then be expanded as:

$$\begin{aligned} S_c(Q, b) &= \exp \left\{ - \int_{b_0^2/b^2}^{Q^2} \frac{dq^2}{q^2} \left[A_c(\alpha_S(q^2)) \log \frac{Q^2}{q^2} + B_c(\alpha_S(q^2)) \right] \right\} \\ &= \left(\frac{\alpha_S(Q^2)}{\pi} \right)^{-1} \bar{g}^{(1)} + \left(\frac{\alpha_S(Q^2)}{\pi} \right)^0 \bar{g}^{(2)} + \left(\frac{\alpha_S(Q^2)}{\pi} \right) \bar{g}^{(3)} + \dots \end{aligned} \quad (3.13)$$

The functions $g^{(m)}$ can be expanded in terms of $\alpha_S^n L^n$, with L representing the large logarithms. Expression (3.13) shows that all large logarithmic terms $\alpha_S^n L^m$, which appeared in the perturbative expansion of the partonic cross section, are included in the Sudakov form factor. Logarithmic contributions for $n+2 \leq m \leq 2n$ are namely vanishing.

The term $\alpha_S^{-1} g^{(1)}$ is called the leading-log (LL) contributions, since this contains all the $\alpha_S^n L^{n+1}$ terms. The next term in the expansion of the Sudakov form factor consists of all $\alpha_S^n L^n$ terms, which can be seen as a correction to the LL term. The function $g^{(2)}$ is therefore the next-to-leading-log (NLL) term. The terms $\alpha_S^n L^{n-1}$ are gathered in the $g^{(3)}$ term, the NNLL term. This expansion continues similarly for the other $g^{(n)}$ terms and is now converging, which was not the case for the expansion in powers of only α_S . The relation between $g^{(n)}$, $A^{(n)}$ and $B^{(n)}$ can be found back in [28, 29]. In order to obtain the full expression for the $g^{(n)}$ functions, one also has to take into account the b dependence of the PDFs (which appears through the factorization scale) and the C_{ab} functions from expression (3.7), which can be obtained by solving the corresponding RGE (see [28, 29]).

One last remark has to be made on the expression for L . The argument of the logarithms can be rescaled:

$$\log Q^2 b^2 = \log Q^2 / \mu_S^2 + \log \mu_S^2 b^2 \quad (3.14)$$

This introduces the resummation scale μ_S . The rescaling is only valid when $\mu_S \sim Q$, therefore one usually chooses $\mu_S = Q$, similar to the preferred choice of the other two scales μ_R and μ_F . Just like with these scales, physical observables cannot depend on the resummation scale.

The parameter L is then usually defined as

$$L = \log \left(\frac{\mu_S^2 b^2}{b_0^2} + 1 \right) \quad (3.15)$$

The factor $b_0 = 2e^\gamma$ emerges from kinematics and is included in the logarithm to simplify the expression for the Sudakov form factor. By including the additional second term in the logarithm, the expression inside becomes 1 at small b (large q_T), so no enhancements would occur in this region of b . It therefore ensures that no large contributions arise from the resummed component for $q_T \sim Q$. At large b (small q_T), the constant term within the logarithm is negligible compared to the first term, and therefore the original definition of $L = \log(Q^2 b^2 / b_0^2)$ is obtained again.

3.2.2 Resummation scheme

Expression (3.7) is invariant under the following transformations:

$$\begin{aligned} H_c^F(\alpha_S) &\rightarrow H_c^F(\alpha_S) [h(\alpha_S)]^{-1} \\ B_c(\alpha_S) &\rightarrow B_c(\alpha_S) - \beta(\alpha_S) \frac{d \log h(\alpha_S)}{d \log \alpha_S} \\ C_{ab}(\alpha_S, z) &\rightarrow C_{ab}(\alpha_S, z) [h(\alpha_S)]^{1/2} \end{aligned} \quad (3.16)$$

The β -function refers again to the RGE of α_S from Eq.(1.10). This type of transformations with an arbitrary perturbative function $h(\alpha_S)$ is called a resummation scheme transformation. It shows that the three functions in Eq.(3.16) can be defined in multiple ways. This ambiguity originates from the divergence

that appears at low q_T . The regularization of this singularity can be done with different procedures, which affects the C_{ab} functions directly and the others through the C_{ab} function. A similar ambiguity appeared already in the introduction of renormalization (Section 1.2) and factorization schemes (Section 2.2.3), both describing how to deal with certain divergences.

As mentioned before, the functions A_c , B_c and C_{ab} are universal. Functions B_c and C_{ab} (and H_c^F) however do depend on the resummation scheme. Usually a choice is being made for H_c^F for one certain process and is $h(\alpha_S)$ set equal to this function. This unambiguously defines the other functions, although the coefficients become process dependent:

$$\begin{aligned} B_c^F(\alpha_S) &= B_c(\alpha_S) - \beta(\alpha_S) \frac{d \log H_c^F}{d \log \alpha_S} \\ C_{ab}^F(\alpha_S, z) &= C_{ab}(\alpha_S, z) [H_c^F]^{1/2} \end{aligned} \quad (3.17)$$

One of the possible resummation schemes is the Drell-Yan scheme, which sets $H_c^F = 1$. The expression for W_N^F in Eq.(3.7) is then the same as the one obtained in the original CSS paper [23]. The expression for B_c^F is then equal to the results obtained for Drell-Yan in this resummation scheme. It shows that viewed from the modern description for all inclusive processes, the resummation procedure for the Drell-Yan process is only one of the possible resummation schemes.

In Chapter 4, the Sudakov form factor for quarks will be compared to a similar form factor appearing in the PB formalism from Chapter 5. For this comparison, the perturbative coefficients of A_q and B_q are needed, therefore they are given here (coming from [28]).

The first two coefficients for the expansion of A_q are:

$$\begin{aligned} A_q^{(1)} &= C_F \\ A_q^{(2)} &= \frac{1}{2} C_F \left(\frac{67}{18} - \frac{\pi^2}{6} \right) \frac{1}{2} C_F C_A - \frac{1}{2} C_F \frac{5}{9} N_f \end{aligned} \quad (3.18)$$

For the $B_q^{(n)}$ coefficients, a choice for the resummation scheme is needed. Choosing the Drell-Yan scheme, the coefficients are:

$$\begin{aligned} B_q^{(1)} &= -\frac{3}{2} C_F \\ B_q^{(2)} &= C_F^2 \left(\frac{\pi^2}{4} - \frac{3}{16} - 3\zeta(3) \right) + C_F C_A \left(\frac{11}{36} \pi^2 - \frac{193}{48} + \frac{3}{2} \zeta(3) \right) + C_F N_f \left(\frac{17}{24} - \frac{\pi^2}{18} \right) \end{aligned} \quad (3.19)$$

with ζ referring to the Riemann zeta-function. The expressions above contain some parameters that are frequently used in SU(N) theories. For QCD, $N_f = 6$ (number of flavours), $C_A = 3$ and $C_F = 4/3$.

3.2.3 Matching procedure

The resummation procedure from above is only valid for $q_T \ll Q$. Resummation is needed in this region of q_T because the perturbative expansion of the partonic cross section contains logarithmically enhanced terms. For higher values of q_T , finite contributions are needed, as is shown in Eq.(3.6). In the original paper on CSS, an expression was obtained for the finite term. In Bozzi et al. [29], another approach is suggested. For higher values of q_T , the logarithms, which cause the problems at low q_T , are no longer large. Perturbation theory is therefore valid in this q_T region. This means that the finite term can be obtained by calculating the difference between the partonic cross section, calculated at a fixed order in α_S , and the resummed term:

$$\left[\frac{d\hat{\sigma}_{F,ab}^{(\text{fin})}}{dq_T^2} \right]_{f.o.} = \left[\frac{d\hat{\sigma}_{F,ab}}{dq_T^2} \right]_{f.o.} - \left[\frac{d\hat{\sigma}_{F,ab}^{(\text{res})}}{dq_T^2} \right]_{f.o.} \quad (3.20)$$

where the "f.o." stands for "fixed order". This describes a matching procedure to obtain the finite term. The partonic cross section calculated at a fixed order in α_S diverges for $q_T \rightarrow 0$ due to the large logarithms,

but this causes no inconveniences because the matching procedure states that the resummed component dominates in the lower q_T regions. The finite term should be zero here, so the subtraction from (3.20) does not have to be performed. On the other hand, in the high q_T region, the resummed component becomes negligible small and the finite term at a fixed order in α_S is simply equal to the partonic cross section calculated at the same order in α_S . The matching procedure becomes crucial for intermediate values of q_T . In this region, both the resummed component and the finite term contribute to the partonic cross section. By extracting the resummed component from the partonic cross section, which does not diverge in this q_T region, the finite term is obtained and double counting is avoided when the partonic cross section is reconstructed again from Eq.(3.6).

One small remark has to be made on the expression of the resummed component in Eq.(3.20). The expression says that this term has to be truncated at the same power of α_S as for the partonic cross section. The resummed component was however ordered in LL, NLL, ... accuracy instead of in powers of α_S . In [29], it is shown how the expression for W_N^F can be rewritten in terms of α_S . This can then be used in Eq.(3.20) to obtain the finite term.

3.3 Parton Branching method

Section 3.1 already described that TMD factorizations are needed in order to obtain accurate results for processes that involve multiple scales. To understand the need for the PB formalism, used to obtain TMD PDFs, the MC event generators will be brought up again. The mechanism behind these computational programs has been explained in Section 2.3 for collinear factorization.

The resummation of the soft gluons, which cause the collinear factorization to fail, is already included in the MC generators through the treatment of the parton showers (a similar procedure will be described in this section). The main concern here is a mismatch that occurs between the calculation of the hard process and the parton showers. The kinematics of the partons that participate in the hard interactions are generated according to the collinear PDFs, meaning that the interacting particles do not have any transverse momentum. In the parton showers however, the partons acquire a transverse momentum at each splitting so the two elements of the event generator cannot be combined immediately. In order to solve this inconvenience, the four-momenta of the partons in the hard process are adjusted. Taking into account energy-momentum conservation, the partons are assigned a transverse momentum that is equal to the transverse momentum obtained from the parton shower. The consequence of doing this, is that the kinematics from the particles in the hard interaction do not correspond any longer to the PDFs. This causes a loss in accuracy on the final results, as is described in [14].

In order to prevent the mismatch and the inaccuracy, a new approach has been set up where the kinematic variables of the partonic cross section are generated according to TMD PDFs instead of collinear PDFs. Using the same TMD PDFs as input for the parton showers makes sure that the transverse momentum of the partons is treated consistently through the whole simulation. Such MC event generators could then be used for inclusive processes (e.g. only the Z boson is being considered as in the CSS formalism) and also for exclusive processes (e.g. studying the Z boson together with the hadron jets).

The key element for the development of these new MC event generators are the TMD PDFs. Several formalisms already exist that can be used to obtain TMD PDFs ¹, but these are usually limited to a certain part of the phase space or do not apply to all quark flavours. The main idea behind the PB formalism is to formulate an evolution equation for TMD PDFs by modifying the DGLAP equations. These equations can be solved using an iterative Monte Carlo procedure, providing TMD PDFs that are valid over a broad range in kinematics for all parton flavours.

¹Two examples are TMD PDFs obtained from the BFKL [31] and the CCFM [32] equations.

3.3.1 Resolvable and non-resolvable emissions

The PB method [30] starts with the DGLAP equations for the collinear PDFs f_a . These equations describe the effect of multiple branching of collinear partons [1]. Following the conventions from [30], the DGLAP equations are written as

$$\frac{\partial \tilde{f}_a(x, \mu^2)}{\partial \log \mu^2} = \sum_b \int_x^1 dz P_{ab}(\alpha_S(\mu^2), z) \tilde{f}_b(x/z, \mu^2) \quad (3.21)$$

with $z = x/\xi$ being the splitting variable. Eq.(3.28) shows the evolution equations for the momentum-weighted PDFs $\tilde{f}_a = x f_a$. Indices a and b still refer to all (anti)quark flavours and the gluon. Before solving these differential equations, the splitting functions P_{ab} have to be rewritten in order to obtain expressions that can be used in numerical calculations. These functions can be divided into three terms:

$$P_{ab}(\alpha_S, z) = D_{ab}(\alpha_S) \delta(1-z) + K_{ab}(\alpha_S) \frac{1}{(1-z)_+} + R_{ab}(\alpha_S, z) \quad (3.22)$$

where the plus index refers to the plus-distribution defined in (2.16). The D_{ab} term represents the virtual contributions, indicated by the Dirac delta function for the longitudinal momentum. Emission and absorption of the same gluon namely does not change the momentum of the parton. The K_{ab} term takes into account the soft gluon contributions. The low energy of these gluons cause the splitting variable z to be close to one. When $z \rightarrow 1$, the K_{ab} term increases and the other terms can then be neglected. The D_{ab} and K_{ab} terms are diagonal in flavour and can be expanded perturbatively:

$$\begin{aligned} D_{ab}(\alpha_S) &= \delta_{ab} \sum_{n=1}^{\infty} \left(\frac{\alpha_S}{2\pi} \right)^n d_a^{(n-1)} \\ K_{ab}(\alpha_S) &= \delta_{ab} \sum_{n=1}^{\infty} \left(\frac{\alpha_S}{2\pi} \right)^n k_a^{(n-1)} \end{aligned} \quad (3.23)$$

The R_{ab} term is free of any singularities and can also be expanded in powers of α_S :

$$R_{ab}(\alpha_S, z) = \sum_{n=1}^{\infty} \left(\frac{\alpha_S}{2\pi} \right)^n R_{ab}^{(n-1)}(z) \quad (3.24)$$

The coefficients $d_a^{(n)}$, $k_a^{(n)}$ and $R_{ab}^{(n)}$ can be found in [33].

The form of the splitting functions as in Eq.(3.22) is inserted into the DGLAP equations. The soft-gluon resolution parameter z_M is now introduced by splitting the integral over z into a part from x to z_M (the resolvable emissions) and a part from z_M to 1 (the non-resolvable emissions). For two partons to be resolvable from each other, they must have a minimal difference in transverse momentum. Conservation of momentum hereby implies that the longitudinal momentum of resolvable emissions is restricted to a maximum value, represented by z_M . Figure 3.3 provides a visualization of splitting the phase space into a resolvable and non-resolvable region. In this particular case, z_M is dependent on the energy scale at which the branching takes place. This will become clearer in Section 3.2.4. The intention of showing this picture here is to simply illustrate the division of the phase space.

First, the contributions from the K_{ab} term are being considered. Using the definition of the plus-distribution, this term can be rewritten as:

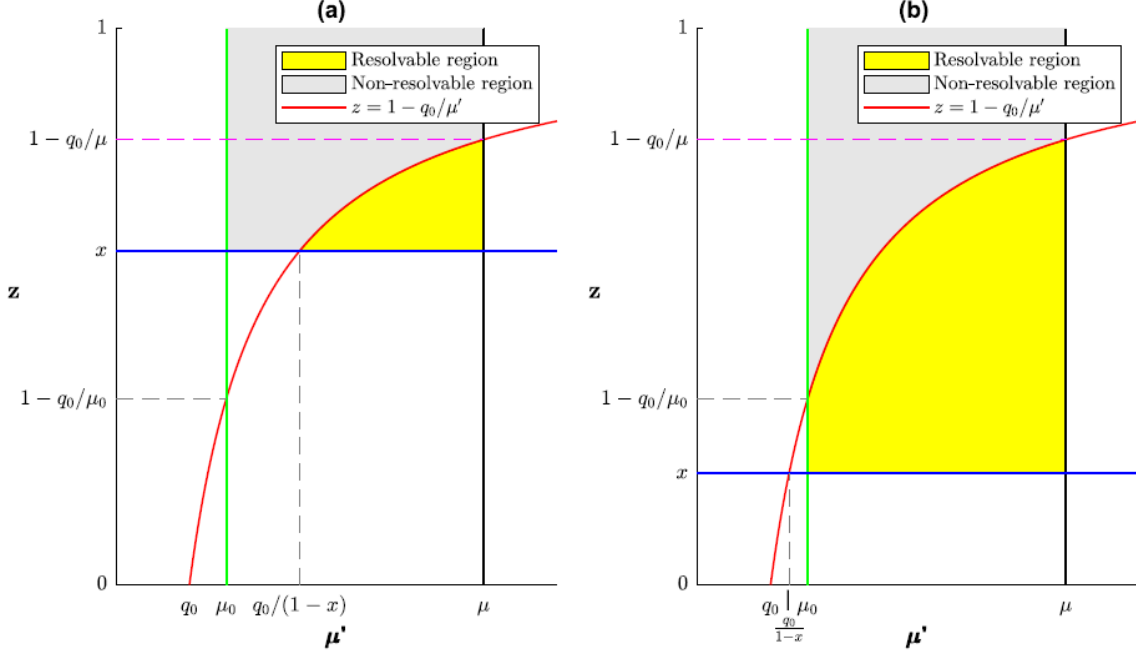


Figure 3.3: Display of the resolvable regions for $1 - q_0/\mu_0 \leq x < 1$ (left) and $1 - q_0/\mu_0 > x > 0$. Source: [34]

$$\begin{aligned}
& \int_x^1 dz K_{ab}(\alpha_S(\mu^2)) \frac{1}{(1-z)_+} \tilde{f}_b(x/z, \mu^2) \\
&= \int_0^1 dz K_{ab}(\alpha_S(\mu^2)) \frac{1}{(1-z)_+} \tilde{f}_b(x/z, \mu^2) - \int_0^x dz K_{ab}(\alpha_S(\mu^2)) \frac{1}{(1-z)_+} \tilde{f}_b(x/z, \mu^2) \\
&= \int_0^1 dz K_{ab}(\alpha_S(\mu^2)) \frac{1}{1-z} \tilde{f}_b(x/z, \mu^2) - \int_0^1 dz K_{ab}(\alpha_S(\mu^2)) \frac{1}{1-z} \tilde{f}_b(x, \mu^2) \\
&\quad - \int_0^x dz K_{ab}(\alpha_S(\mu^2)) \frac{1}{1-z} \tilde{f}_b(x/z, \mu^2) \\
&= \int_x^1 dz K_{ab}(\alpha_S(\mu^2)) \frac{1}{1-z} \tilde{f}_b(x/z, \mu^2) - \int_0^1 dz K_{ab}(\alpha_S(\mu^2)) \frac{1}{1-z} \tilde{f}_b(x, \mu^2)
\end{aligned} \tag{3.25}$$

In the integral from 0 to x , the plus-description can be dropped since the $z = 1$ singularity is not included in the integration range.

When inserting the z_M parameter, one can make use of the approximation that $1 - z_M$ is very small. It can be chosen to be of the order of Λ_{QCD}/μ , with Λ_{QCD} being the QCD scale. Therefore only terms up to $(1 - z_M)^0$ are included, higher powers are neglected. The momentum-weighted PDF's in the region between z_M and z can then be expanded:

$$\tilde{f}_b(x/z, \mu^2) = \tilde{f}_b(x, \mu^2) + (1-z) \frac{\partial \tilde{f}_b}{\partial \log x}(x, \mu^2) + \mathcal{O}(1-z)^2 \tag{3.26}$$

In this region for z , the second term in the expansion can be dropped, meaning that $\tilde{f}_b(x/z, \mu^2) = \tilde{f}_b(x, \mu^2)$ up to $\mathcal{O}(1 - z_M)$. This gives:

$$\begin{aligned}
& \int_x^1 dz K_{ab}(\alpha_S(\mu^2)) \frac{1}{(1-z)_+} \tilde{f}_b(x/z, \mu^2) \\
&= \int_x^{z_M} dz K_{ab}(\alpha_S(\mu^2)) \frac{1}{1-z} \tilde{f}_b(x/z, \mu^2) + \int_{z_M}^1 dz K_{ab}(\alpha_S(\mu^2)) \frac{1}{1-z} \tilde{f}_b(x/z, \mu^2) \\
&\quad - \int_0^1 dz K_{ab}(\alpha_S(\mu^2)) \frac{1}{1-z} \tilde{f}_b(x, \mu^2) \\
&= \int_x^{z_M} dz K_{ab}(\alpha_S(\mu^2)) \frac{1}{1-z} \tilde{f}_b(x/z, \mu^2) + \int_{z_M}^1 dz K_{ab}(\alpha_S(\mu^2)) \frac{1}{1-z} \tilde{f}_b(x, \mu^2) \\
&\quad - \int_0^1 dz K_{ab}(\alpha_S(\mu^2)) \frac{1}{1-z} \tilde{f}_b(x, \mu^2) \\
&= \int_x^{z_M} dz K_{ab}(\alpha_S(\mu^2)) \frac{1}{1-z} \tilde{f}_b(x/z, \mu^2) - \int_0^{z_M} dz K_{ab}(\alpha_S(\mu^2)) \frac{1}{1-z} \tilde{f}_b(x, \mu^2)
\end{aligned} \tag{3.27}$$

The integral from z_M to 1 cancels exactly with the third integral (split into two parts) in the last step. Therefore this alteration of the integral of K_{ab} is correct up to $\mathcal{O}(1-z_M)$. The contributions from the other two terms from Eq.(3.22) can each be assigned to one of the two terms in the integral of the K_{ab} term above. The D_{ab} term will contribute proportional to $\tilde{f}_b(x, \mu^2)$ due to the Dirac delta function. The R_{ab} term does not contain any singularities. This function can therefore be expanded in a Taylor series around $z = 1$. Therefore, for $z > z_M$, the contributions from the R_{ab} term will be of order $\mathcal{O}(1-z_M)$ and can thus be neglected. For $z < z_M$, the contributions from the R_{ab} term will be proportional to $\tilde{f}_b(x/z, \mu^2)$.

The DGLAP equations can thus be written as:

$$\begin{aligned}
\frac{\partial \tilde{f}_a(x, \mu^2)}{\partial \log \mu^2} &= \sum_b \int_x^{z_M} dz \left[K_{ab}(\alpha_S(\mu^2)) \frac{1}{1-z} + R_{ab}(\alpha_S(\mu^2), z) \right] \tilde{f}_b(x/z, \mu^2) \\
&\quad + \sum_b \left\{ \int_x^1 dz D_{ab}(\alpha_S(\mu^2)) \delta(1-z) - \int_0^{z_M} dz K_{ab}(\alpha_S(\mu^2)) \frac{1}{1-z} \right\} \tilde{f}_b(x, \mu^2)
\end{aligned} \tag{3.28}$$

The benefit of decomposing the DGLAP equations in terms of $\tilde{f}_b(x, \mu^2)$ and $\tilde{f}_b(x/z, \mu^2)$, is that the real emissions are now separated from the virtual and non-resolvable emissions. The real emissions alter the momentum fraction and are therefore represented in the first line of (3.28). The terms inside the square brackets are defined as the real-emission branching probabilities $P_{ab}^{(R)}(\alpha_S, z)$. The second line refers to virtual emissions, that do not change the momentum fraction carried by the initial parton.

In Section 2.3, the momentum sum rule has been introduced in expression (2.19):

$$\sum_c \int_0^1 dz z P_{ca}(\alpha_S(\mu^2), z) = 0 \tag{3.29}$$

The same separation of singularities as in (3.22) can be applied inside the integral:

$$\begin{aligned}
& \int_0^1 dz z P_{ca}(\alpha_S(\mu^2), z) \\
&= \int_0^1 dz z D_{ca}(\alpha_S(\mu^2)) \delta(1-z) + \int_0^1 dz z K_{ca}(\alpha_S(\mu^2)) \frac{1}{(1-z)_+} + \int_0^1 dz z R_{ca}(\alpha_S(\mu^2), z) \\
&= \int_0^1 dz z D_{ca}(\alpha_S(\mu^2)) \delta(1-z) + \int_0^1 dz z K_{ca}(\alpha_S(\mu^2)) \frac{1}{1-z} \\
&\quad - \int_0^1 dz K_{ca}(\alpha_S(\mu^2)) \frac{1}{1-z} + \int_0^{z_M} dz z R_{ca}(\alpha_S(\mu^2), z)
\end{aligned} \tag{3.30}$$

As was mentioned before, the contribution from the R_{ab} term was negligible when $z > z_M$. By inserting the expression from Eq.(3.29) into the DGLAP equations, which is possible since it is equal to zero, the virtual emissions can be dealt with:

$$\begin{aligned}
\frac{\partial \tilde{f}_a(x, \mu^2)}{\partial \log \mu^2} &= \sum_b \int_x^{z_M} dz P_{ab}^{(R)}(\alpha_S(\mu^2), z) \tilde{f}_b(x/z, \mu^2) \\
&+ \sum_c \left\{ \int_x^1 dz D_{ac}(\alpha_S(\mu^2)) \delta(1-z) - \int_0^{z_M} dz K_{ac}(\alpha_S(\mu^2)) \frac{1}{1-z} \right. \\
&\quad \left. - \int_0^1 dz z P_{ca}(\alpha_S(\mu^2), z) \right\} \tilde{f}_b(x, \mu^2) \\
&= \sum_b \int_x^{z_M} dz P_{ab}^{(R)}(\alpha_S(\mu^2), z) \tilde{f}_b(x/z, \mu^2) \\
&- \left\{ \sum_c \int_0^{z_M} dz z K_{ca}(\alpha_S(\mu^2)) \frac{1}{1-z} + \sum_c \int_0^{z_M} dz z R_{ca}(\alpha_S(\mu^2), z) \right\} \tilde{f}_b(x, \mu^2)
\end{aligned} \tag{3.31}$$

The D_{ac} terms cancel each other due to the Dirac delta function and because this term is diagonal in flavour. The K_{ac} terms that can be combined (due to being diagonal in flavour) give an integral from z_M to 1, which has a contribution of order $(1 - z_M)$ as has been discussed earlier. This can therefore be neglected. The remaining terms between the curly brackets combine together again to the real-emission branching probability $P_{ca}^{(R)}$.

$$\begin{aligned}
\frac{\partial \tilde{f}_a(x, \mu^2)}{\partial \log \mu^2} &= \sum_b \left\{ \int_x^{z_M} dz P_{ab}^{(R)}(\alpha_S(\mu^2), z) \tilde{f}_b(x/z, \mu^2) \right. \\
&\quad \left. - \int_0^{z_M} dz z P_{ba}^{(R)}(\alpha_S(\mu^2), z) \tilde{f}_b(x, \mu^2) \right\}
\end{aligned} \tag{3.32}$$

The DGLAP equations have now be written in terms of the real-emission branching probabilities $P_{ab}^{(R)}$ and $P_{ba}^{(R)}$. Both do not contain the singularity at $z = 1$ (integral only goes to z_M) and there is no longer a Dirac delta function present. This expression will be appropriate to use in an iterative numerical MC solution which will be discussed in the following sections.

3.3.2 Sudakov form factor

One last step is needed before an expression is obtained to solve with MC. For this, the Sudakov form factor is introduced. This factor tells the probability that no branching appears for the parton a when evolving the scale from μ_0 to μ (see [14]).

$$\Delta_a(z_M, \mu^2, \mu_0^2) = \exp \left\{ - \sum_b \int_{\mu_0^2}^{\mu^2} \frac{d\bar{\mu}^2}{\bar{\mu}^2} \int_0^{z_M} dz z P_{ba}^{(R)}(\alpha_S(\bar{\mu}^2), z) \right\} \tag{3.33}$$

The Sudakov form factor also appeared in the review on the CSS formalism in order to resum the soft gluons. A discussion on the differences between the two expressions follows in the next chapter. In this case, the Sudakov form factor resums the large contributions coming from virtual and real corrections up to all orders. The unitarity of the branching probabilities is important here, because this is what takes these contributions into account [1].

Thanks to the unitarity, the Sudakov form factor can be rewritten into a form that is more useful for Chapter 4. Unitarity says that $P_{ab} = P_{ab}^{(R)} + P_{ab}^{(V)}$ and by using the momentum sum rule, the Sudakov form factor becomes [35]:

$$\Delta_a(z_M, \mu^2, \mu_0^2) = \exp \left\{ - \sum_b \int_{\mu_0^2}^{\mu^2} \frac{d\bar{\mu}^2}{\bar{\mu}^2} \int_0^{z_M} dz \left[\frac{K_{ab}(\alpha_S)}{1-z} - D_{ab}(\alpha_S) \delta(1-z) \right] \right\} \tag{3.34}$$

The evolution equation of the Sudakov form factor from Eq.(3.33) is given by:

$$\frac{1}{\Delta_a(z_M, \mu^2, \mu_0^2)} \frac{\partial \Delta_a(z_M, \mu^2, \mu_0^2)}{\partial \log \mu^2} = - \sum_b \int_0^{z_M} dz z P_{ba}^{(R)}(\alpha_S(\mu), z) \quad (3.35)$$

The right-hand side of this expression can be recognized in Eq.(3.32), which shows that the Sudakov form factor takes into account the contributions from the non-resolvable part. Inserting this expression into the DGLAP equations gives:

$$\begin{aligned} \frac{\partial \tilde{f}_a(x, \mu^2)}{\partial \log \mu^2} &= \sum_b \int_x^{z_M} dz P_{ab}^{(R)}(\alpha_S(\mu^2), z) \tilde{f}_b(x/z, \mu^2) \\ &\quad - \frac{1}{\Delta_a(z_M, \mu^2, \mu_0^2)} \frac{\partial \Delta_a(z_M, \mu^2, \mu_0^2)}{\partial \log \mu^2} \end{aligned} \quad (3.36)$$

which can be written as:

$$\frac{\partial}{\partial \log \mu^2} \left(\frac{\tilde{f}_a(x, \mu^2)}{\Delta_a(z_M, \mu^2, \mu_0^2)} \right) = \sum_b \int_x^{z_M} dz P_{ab}^{(R)}(\alpha_S(\mu^2), z) \frac{\tilde{f}_b(x/z, \mu^2)}{\Delta_a(z_M, \mu^2, \mu_0^2)} \quad (3.37)$$

A similar expression to the original DGLAP equations is now obtained, where the momentum-weighted PDFs are divided by the Sudakov form factor and where the splitting functions P_{ab} are replaced by the real-emission branching probabilities $P_{ab}^{(R)}$. Integrating this expression (and setting the initial condition $\mu = \mu_0$) yields a solution for the momentum-weighted PDFs:

$$\tilde{f}_a(x, \mu^2) = \Delta_a(z_M, \mu^2, \mu_0^2) \tilde{f}_a(x, \mu_0^2) + \sum_b \int_{\mu_0^2}^{\mu^2} \frac{d\bar{\mu}^2}{\bar{\mu}^2} \frac{\Delta_a(z_M, \mu^2, \mu_0^2)}{\Delta_a(z_M, \bar{\mu}^2, \mu_0^2)} \int_x^{z_M} dz P_{ab}^{(R)}(\alpha_S(\bar{\mu}^2), z) \tilde{f}_b(x/z, \bar{\mu}^2) \quad (3.38)$$

When solving the evolution equation, the identity $\Delta_a(z_M, \mu_0^2, \mu_0^2) = 1$ is used. The probability to have no-branching in between two identical scales is one since the argument of the exponential from (3.33) is zero.

The solution for $\tilde{f}_a(x, \mu^2)$ is an integral of Fredholm type, which has a general format:

$$f(t) = f_0(t) + \lambda \int_a^b K(t, y) f(y) dy \quad (3.39)$$

One way of solving this type of integral equations is by expanding $f(t)$ as a series:

$$f(t) = \lim_{n \rightarrow \infty} \sum_{i=0}^n \lambda^i u_i(t) \quad (3.40)$$

Each u_i can then be solved iteratively:

$$\begin{aligned} u_0(t) &= f_0(t) \\ u_1(t) &= \int_a^b K(t, y) f_0(y) dy \\ u_2(t) &= \int_a^b \int_a^b K(t, y_1) K(y_1, y_2) f_0(y_2) dy_2 dy_1 \\ &\dots \\ u_n(t) &= \int_a^b \int_a^b \int_a^b K(t, y_1) \dots K(y_{n-1}, y_n) f_0(y_n) dy_n \dots dy_2 dy_1 \end{aligned} \quad (3.41)$$

The next section shows how the iterative solution method exactly works for the calculation of the momentum-weighted PDF's.

3.3.3 Collinear PDFs

Applying the general solution method to the obtained expression for the collinear PDF in Eq.(3.38) gives for the first two terms of the expansion:

$$\begin{aligned}\tilde{f}_a^{(0)}(x, \mu^2) &= \Delta_a(z_M, \mu^2, \mu_0^2) \tilde{f}_a(x, \mu_0^2) \\ \tilde{f}_a^{(1)}(x, \mu^2) &= \sum_b \int_{\mu_0^2}^{\mu^2} \frac{d\bar{\mu}^2}{\bar{\mu}^2} \frac{\Delta_a(z_M, \mu^2, \mu_0^2)}{\Delta_a(z_M, \bar{\mu}^2, \mu_0^2)} \int_x^{z_M} dz \Delta_b(z_M, \bar{\mu}^2, \mu_0^2) P_{ab}^{(R)}(\alpha_S(\bar{\mu}^2), z) \tilde{f}_b(x/z, \mu_0^2)\end{aligned}\quad (3.42)$$

The solution of $\tilde{f}_a^{(0)}(x, \mu^2)$ is inserted into the expression for $\tilde{f}_a^{(1)}(x, \mu^2)$ and this continues for the other functions. That way, an iterative procedure is being followed. The collinear PDF at a scale μ is then a sum of these terms:

$$\tilde{f}_a(x, \mu^2) = \sum_i^{\infty} \tilde{f}_a^{(i)}(x, \mu^2) \quad (3.43)$$

Each of the terms in the expansion can be interpreted as a possible parton branching configuration when evolving the scale from μ_0^2 to μ^2 . The first three iterative solutions are illustrated in figure 3.4, where the initial momentum fraction and scale are x_i and μ_i . A first contribution to $\tilde{f}_a(x, \mu^2)$ is from the possibility that a parton of flavour a and momentum fraction x does not emit other partons when changing the scale. This first configuration is showed in the left figure. No branching occurs evolving from μ_i to μ and the momentum fraction stays the same.

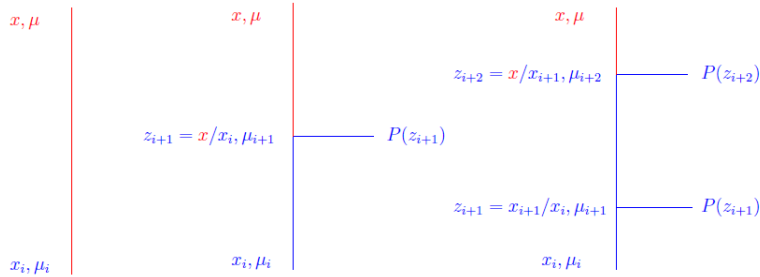


Figure 3.4: When evolving the scale from μ_i to μ , branching can occur at scales μ_{i+1} , μ_{i+2} , \dots with corresponding splitting variables z_{i+1} , z_{i+2} , \dots , as is depicted in this figure. Source: [30]

The first term $\tilde{f}_a^{(0)}(x, \mu^2)$ of the expansion tells the same. One has a PDF for parton a with momentum fraction x at a starting scale μ_0^2 multiplied by the probability that no branching occurs for the parton a between the scales μ_0^2 and μ^2 .

The next possible configuration is that an initial parton of flavour b and with momentum fraction x_i emits a parton at a scale $\bar{\mu}^2$, represented by the middle figure. The initial parton is changed to a parton of flavour a and the momentum fraction is lowered to x due to the splitting. That way $\tilde{f}_a(x, \mu^2)$ can obtain a contribution from $\tilde{f}_b(x_i, \mu^2)$. This configuration is displayed by the $\tilde{f}_a^{(1)}(x, \mu^2)$ term. The integral over z contains two probability functions together with the PDF for the initial parton. The first function tells the probability that parton b does not undergo any branching from μ_0^2 to $\bar{\mu}^2$, represented by Δ_b . The second function refers to the probability that a resolvable splitting occurs at the scale $\bar{\mu}^2$ with a splitting variable $z = x/x_i$, represented by $P_{ab}^{(R)}$.

The fraction of two Sudakov form factors that appears in Eq.(3.42) can be rewritten as

$$\frac{\Delta_a(z_M, \mu^2, \mu_0^2)}{\Delta_a(z_M, \bar{\mu}^2, \mu_0^2)} = \Delta_a(z_M, \mu^2, \bar{\mu}^2) \quad (3.44)$$

by using the definition of this factor. The fraction therefore represents the probability that no further branching occurs when evolving the scale from $\bar{\mu}^2$ to μ^2 , where $\bar{\mu}^2$ refers to the scale at which the one branching occurs. The parton a obtained through the splitting at $\bar{\mu}^2$ retains its momentum fraction till μ^2 .

The same applies for an arbitrary number of branching between the scales μ_0^2 and μ^2 that in the end produce the parton a with momentum fraction x . In this way all the terms $\tilde{f}_a^{(i)}(x, \mu^2)$ can be obtained. For the Δ_b and $P_{ab}^{(R)}$ factors, one uses the perturbative expansions of K_{ab} , D_{ab} and R_{ab} to obtain a value for these expressions. The coefficients for the first two orders of K_{ab} and D_{ab} are (reminding that the two functions are diagonal in flavour):

$$\begin{aligned} d_q^{(0)} &= \frac{3}{2}C_F, & d_g^{(0)} &= \frac{11}{6}C_A - \frac{2}{3}T_R N_f \\ d_q^{(1)} &= C_F^2 \left(\frac{3}{8} - \frac{\pi^2}{2} + 6\zeta(3) \right) + C_F C_A \left(\frac{17}{24} + \frac{11\pi^2}{18} - 3\zeta(3) \right) - C_F T_R N_f \left(\frac{1}{6} + \frac{2\pi^2}{9} \right) \\ d_g^{(1)} &= C_A^2 \left(\frac{8}{3} + 3\zeta(3) \right) - \frac{4}{3}C_A T_R N_f - C_F T_R N_f \end{aligned} \quad (3.45)$$

and

$$\begin{aligned} k_q^{(0)} &= 2C_F, & k_g^{(0)} &= 2C_A \\ k_q^{(1)} &= 2C_F C_A \left(\frac{67}{18} - \frac{\pi^2}{6} \right) - 2C_F T_R N_f \frac{10}{9} \\ k_g^{(1)} &= 2C_A C_A \left(\frac{67}{18} - \frac{\pi^2}{6} \right) - 2C_A T_R N_f \frac{10}{9} \end{aligned} \quad (3.46)$$

Most of the variables have already appeared in the coefficients of the A and B functions in the CSS formalism (expression (3.18) and (3.19)). The variable T_R is equal to $1/2$. The perturbative coefficients of R_{ab} are longer and can be found back in [30].

The integrals over z and $\bar{\mu}^2$ are performed numerically by a Monte Carlo method. Random values for the two variables are generated and the integrands are evaluated at those values. By doing this many times, one obtains an approximate solution for the two integrals. For the initial PDFs that appear in the integrals, different parametrizations can be chosen.

The MC approach of obtaining PDFs is similar to how a MC event generator constructs the parton shower. Writing the solution to the DGLAP equations in terms of branching and no-branching probabilities makes it possible to simulate the numerous emissions that also occur in particle colliders. This technique is however not used to obtain PDFs, but to keep track of all the particles and their kinematic properties.

3.3.4 TMD PDFs

In the previous section, it has been shown how the collinear PDFs can be obtained with the PB method. Generating individual resolvable emissions makes it also possible to evaluate the kinematics in each branching. The transverse momentum of each particle can always be taken correctly into account. The PB method is therefore appropriate to describe the evolution of the TMD PDFs.

Figure 3.5 shows the kinematics of an individual branching. After the branching, the two partons acquire a transverse momentum, which relates to the transverse momentum of the initial parton as $\mathbf{k}_{T,b} = \mathbf{k}_{T,a} + \mathbf{q}_c$. Furthermore, conservation of momentum implies:

$$p_b^2 = \frac{p_a^2 + \mathbf{q}_c^2}{z} + \frac{p_c^2 + \mathbf{q}_c^2}{1-z} \quad (3.47)$$

From this relation, there are multiple ways to relate the energy scale μ'^2 , at which the branching takes place, and the transverse momentum \mathbf{q}_c of the emitted parton c . One way is by setting μ'^2 equal to the virtuality of the propagating parton a : $\mu'^2 = -p_a^2$. This also implies that $p_b^2 = p_c^2 = 0$. In the limit of $z \rightarrow 0$ the relation between μ' and \mathbf{q}_c becomes:

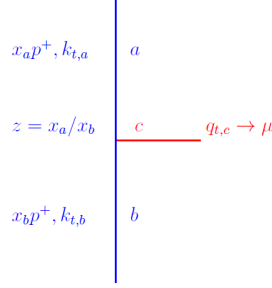


Figure 3.5: The branching of a parton b into a parton a and c , light-cone momenta are assigned to the particles. Source: [30]

$$\mu' = |\mathbf{q}_c| \quad (3.48)$$

This is called transverse momentum ordering [36]. Another possibility is to link μ' to the angle between the beam direction and the parton c . This gives

$$\mu' = \frac{|\mathbf{q}_c|}{1-z} \quad (3.49)$$

which is called the angular ordering [37]. Both ordering relations show how a value for \mathbf{q}_c can be obtained from the generated μ' at each branching. The total transverse momentum \mathbf{k}_T acquired by the initial parton after undergoing branching a numerous amount of times is then:

$$\mathbf{k}_T = - \sum_c \mathbf{q}_c \quad (3.50)$$

which makes it possible to define the TMD PDF $\mathcal{A}_a(x, \mathbf{k}_T, \mu^2)$.

Besides serving as a relation between the energy scale and the transverse momentum, the angular ordering also has a physical meaning. It is a property of all gauge theories, therefore an example from QED will be used.

The angular ordering property is the reason behind the Chudakov effect in QED, which is the suppression of soft photon emissions for electron-positron pairs. Figure 3.6 shows this process. After the creation of the electron-positron pair, the two particles travel away from each other under an angle θ^* with respect to the beam axis. One of the particles emits a photon later under an angle θ , which causes the electron/positron to acquire a transverse momentum k_T . The longitudinal momentum of the lepton is then only a fraction $(1-z)$ of the original momentum p . The angular ordering property refers to a condition on the two angles.

The uncertainty principle sets an available time on the emission of the photon by $\Delta t \sim 1/\Delta E$, with ΔE being the energy imbalance at the vertex. Assuming that $\theta \ll 1$ and $\theta^* \ll 1$, the obtained transverse momentum k_T of the lepton is proportional to $zp\theta$ and therefore:

$$\Delta t \sim 1/\Delta E \sim zp/k_T^2 \sim (zp\theta^2)^{-1} \quad (3.51)$$

In the same time, the transverse separation between the electron and positron has become $\Delta b \sim \theta^* \Delta t$. If the emitted photon is not able to resolve the two leptons, then it sees the pair as one system without a charge. This implies that no photon emissions is possible, because only charged particles are able to do this. The emitted photon, with wavelength λ , resolves the electron and positron when

$$\Delta b > \lambda/\theta \sim (zp\theta)^{-1} \quad (3.52)$$

which gives the following condition:

$$\begin{aligned} \theta^* (zp\theta^2)^{-1} &> (zp\theta)^{-1} \\ \Leftrightarrow \theta^* &> \theta \end{aligned} \quad (3.53)$$

The angular ordering property therefore accounts for a suppression of soft photon emissions under a larger angle than the angle between electron and positron. It creates a coherence effect for the emitted photons.

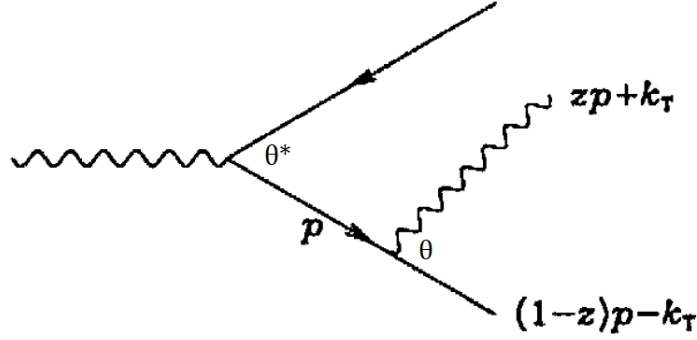


Figure 3.6: Emission of a soft photon from an electron-positron pair. Source: [1]

A similar effect appears in QCD for the emissions of soft gluons and is called the gluon coherence effect. The main difference is that instead of an electric charge, the particles engaged in the process have a colour charge. The electron and positron are replaced by two partons that form a colour singlet together. The coherence effect will also play a role when multiple emissions of gluons appear, as in figure 3.7. The angular ordering can be used here by neglecting the transverse momentum k_T of the parton before emitting the gluon. For example for $q_{T,i+1}$, this means that $k_{T,i} \approx 0$ and $k_{T,i-1} \approx 0$ for $q_{T,i}$. This means that the angles θ_{i+1} , θ_i, \dots can always be seen as the angle with respect to the beam axis. The angular ordering property then implies that $\theta_{i+1} > \theta_i$. The difference in sign is because the Chudakov effect treated final-state emissions, while initial-state emissions are being considered for the parton branching.

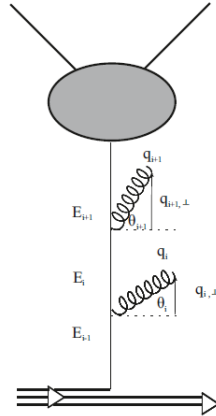


Figure 3.7: A cascade of gluon emissions, where the angular ordering will set a condition on the angles θ_i of successive branching. Source: [14]

By applying angular ordering, the gluon coherence effect is taken into account and the soft gluons are treated correctly. This can be observed in the results from [38]. TMD PDFs generated with the angular

ordering do not depend on the arbitrary soft-gluon resolution parameter z_M , as one would like it to be. However, the result is different when using the transverse momentum ordering, because these TMD PDFs do depend on z_M . That is because this ordering acts as a cut-off on the kinematics of the emitted gluons. The angular ordering on the other hand takes into account the cancellation of non-resolvable emissions due to the coherence effect.

The different ways of relating the transverse momentum with the energy scale also has an influence on the soft-gluon resolution parameter z_M . The parameter can be fixed to some value or it is also possible to make it dependent of μ , which makes z_M dynamical. Introducing a $q_{T,0}$ which stands for the minimum transverse momentum for an emitted parton to be resolvable, one has:

$$q_T > q_{T,0} \quad (3.54)$$

Inserting this into the angular ordering property gives:

$$z_M(\mu') = 1 - \frac{q_{T,0}}{\mu'} \quad (3.55)$$

Different $z_M(\mu')$ functions can be obtained from the other ordering properties. This implies that the resolvable region is determined by the energy scale μ' , as has been displayed in figure 3.3.

After relating the transverse momentum and the branching scale through one of the ordering properties, the following equation for the TMD PDF $\tilde{\mathcal{A}}_a(x, \mathbf{k}_T, \mu^2)$ ($= x\mathcal{A}_a(x, \mathbf{k}_T, \mu^2)$) can be proposed by extending the expression for $\tilde{f}_a(x, \mu^2)$ in Eq.(3.38) to include the k_T dependence. In case of the angular ordering, one obtains:

$$\begin{aligned} \tilde{\mathcal{A}}_a(x, \mathbf{k}_T, \mu^2) &= \Delta_a(z_M, \mu^2, \mu_0^2) \tilde{\mathcal{A}}_a(x, \mathbf{k}_T, \mu_0^2) + \sum_b \int \frac{d^2 \mu'}{\pi \mu'^2} \frac{\Delta_a(z_M(\mu'), \mu^2, \mu_0^2)}{\Delta_a(z_M(\mu'), \mu'^2, \mu_0^2)} \Theta(\mu^2 - \mu'^2) \Theta(\mu'^2 - \mu_0^2) \\ &\quad \times \int_x^{z_M(\mu')} dz P_{ab}^{(R)}(\alpha_S(\mu'^2), z) \tilde{\mathcal{A}}_b(x/z, \mathbf{k}_T + (1-z)\mu', \mu'^2) \end{aligned} \quad (3.56)$$

The dynamical $z_M(\mu')$ can be similarly inserted into the solution for the collinear PDFs. In this case, $z_M(\mu')$ is given by (3.55). The Heaviside step function acts as integral boundaries for the scale $\mu'^2 = |\mu'^2|$. The solution for this equation can be obtained again by solving the integral of Fredholm type with a series for $\tilde{\mathcal{A}}_a(x, \mathbf{k}_T, \mu^2)$:

$$\begin{aligned} \tilde{\mathcal{A}}_a(x, \mathbf{k}_T, \mu^2) &= \sum_{i=0}^{\infty} \tilde{\mathcal{A}}_a^{(i)}(x, \mathbf{k}_T, \mu^2) \\ \tilde{\mathcal{A}}_a^{(0)}(x, \mathbf{k}_T, \mu^2) &= \Delta_a(z_M(\mu'), \mu^2, \mu_0^2) \tilde{\mathcal{A}}_a(x, \mathbf{k}_T, \mu_0^2) \\ \tilde{\mathcal{A}}_a^{(1)}(x, \mathbf{k}_T, \mu^2) &= \int \frac{d^2 \mu'}{\pi \mu'^2} \frac{\Delta_a(z_M(\mu'), \mu^2, \mu_0^2)}{\Delta_a(z_M(\mu'), \mu'^2, \mu_0^2)} \Theta(\mu^2 - \mu'^2) \Theta(\mu'^2 - \mu_0^2) \\ &\quad \times \int_x^{z_M(\mu')} dz P_{ab}^{(R)}(\alpha_S(\mu'^2), z) \Delta_b(z_M(\mu'), \mu'^2, \mu_0^2) \tilde{\mathcal{A}}_a(x, \mathbf{k}_T + (1-z)\mu', \mu_0^2) \end{aligned} \quad (3.57)$$

The terms in the expansion of $\tilde{\mathcal{A}}_a(x, \mathbf{k}_T, \mu^2)$ can be interpreted in the same way as the ones for $\tilde{f}_a(x, \mu^2)$ by considering the order i as the amount of branches that appear. The $\tilde{\mathcal{A}}_a^{(0)}$ term refers to the configuration without a single branching. The $\tilde{\mathcal{A}}_a^{(1)}$ considers a single branching that brings forth the parton a from a parton b with transverse momentum $\mathbf{k}_T + (1-z)\mathbf{q}' = \mathbf{k}_T + \mathbf{q}_c$.

For the collinear PDFs, an initial distribution is parametrized and used to obtain PDFs at other energy scales. The initial TMD PDF is treated similarly by also using an initial collinear PDF. The \mathbf{k}_T -dependence is added through a Gaussian smearing G :

$$G = \exp \left\{ - \frac{|\mathbf{k}_T^2|}{\sigma^2} \right\} \quad (3.58)$$

This is important to take into account when numerical results are being compared to other formalisms, which will be done in Chapter 5.

Part III

Comparison between the PB and CSS formalisms

Chapter 4

Analytic comparison

At first sight, the PB and CSS formalisms look different because they are introduced in different contexts. The CSS formalism provides an analytical resummation of the soft gluon contributions, while the PB method uses a MC approach in order to obtain evolution equations for TMF PDFs. Nonetheless, the two formalisms want to obtain precise predictions for collider observables that are affected by QCD radiation, which means that they can still be compared analytically. This is done in this chapter.

Both formalisms contain the Sudakov form factor which takes into account the resummation of contributions from soft-gluons emissions, although there is a difference in definition between the two formalisms. The factor consists of perturbative functions of which the first couple coefficients are known. The CSS formalism describes the Sudakov form factor in terms of the functions A_a and B_a (as in (3.9)), while the PB approach does it in a similar way with the functions K_{ab} and D_{ab} (see (3.34)). After rewriting expression (3.34), both definitions of the Sudakov form factor can be compared directly to each other to check similarities between the perturbative coefficients.

The comparison of Sudakov form factors up to NNLL accuracy has already been made last year and can be found back in the master thesis of A.M. van Kampen [35]. What follows now is a brief summary of his results combined with a new approach, which is being studied now. This approach introduces a physical coupling (in analogy with [39]) which would provide the possibility to include the $A^{(3)}$ coefficient in the PB method, so that an additional part of the NNLL resummation would be present besides the $B^{(2)}$ coefficient. Another attempt at this has already been made by including the NNLO splitting functions into the PB calculations. However, some issues were encountered.

4.1 Sudakov form factors

Before the two Sudakov form factors can be compared to each other, the expression. It has already been rewritten as

$$\Delta_a(z_M, \mu^2, \mu_0^2) = \exp \left\{ - \sum_b \int_{\mu_0^2}^{\mu^2} \frac{d\bar{\mu}^2}{\bar{\mu}^2} \int_0^{z_M} dz \left[\frac{K_{ab}(\alpha_S)}{1-z} - D_{ab}(\alpha_S) \delta(1-z) \right] \right\} \quad (4.1)$$

in Eq.(3.34). The benefit of writing the factor like this, is because it now contains the virtual splitting and can be compared to the CSS formalism. The angular ordering is also needed here to be sure that the soft gluons are correctly dealt with. Changing the integral variable to the transverse momentum gives:

$$\Delta_a(\mu^2, q_0^2) = \exp \left\{ - \int_{q_0^2}^{\mu^2} \frac{dq_{\perp}^2}{q_{\perp}^2} \int_0^{1-\frac{q_{\perp}^2}{\mu^2}} dz \left[\frac{k_a(\alpha_S(q_{\perp}^2))}{1-z} - d_a(\alpha_S(q_{\perp}^2)) \delta(1-z) \right] \right\} \quad (4.2)$$

where the functions were written as $K_{ab} = \delta_{ab}k_a$ and $D_{ab} = \delta_{ab}d_a$ to get rid of the summation over flavour b . Integrating over z gives

$$\Delta_a(\mu^2, q_0^2) = \exp \left\{ - \int_{q_0^2}^{\mu^2} \frac{dq_{\perp}^2}{q_{\perp}^2} \left[\frac{1}{2} \log\left(\frac{\mu^2}{q_{\perp}^2}\right) k_a(\alpha_S(q_{\perp}^2)) - d_a(\alpha_S(q_{\perp}^2)) \right] \right\} \quad (4.3)$$

This expression simplifies the comparison between the two Sudakov form factors. The factor in the CSS formalism has indeed a similar form:

$$S_a(Q, b) = \exp \left\{ - \int_{b_0^2/b^2}^{Q^2} \frac{dq^2}{q^2} \left[\log\left(\frac{Q^2}{q^2}\right) A_a(\alpha_S(q^2)) + B_a(\alpha_S(q^2)) \right] \right\} \quad (4.4)$$

One difference between the formalisms is that the CSS formalism was set up in \mathbf{b} -space, the Fourier transform of \mathbf{q}_{\perp} . Changing the integration variable in (4.2) to the transverse momentum displays the possibility to shift the expression into \mathbf{b} -space. Transforming from \mathbf{q}_{\perp} to \mathbf{b} would hereby not affect the d_a and k_a functions.

Another difference that needs to be pointed out is that the PB formalism produces an expression for the TMD PDFs, while the CSS formalism calculates the cross section. To evaluate the cross section with TMD PDFs, one would have to convolute these with the partonic matrix element $\hat{\sigma}$ as in [40]:

$$\sigma \sim \int_0^1 \frac{dz_1}{z_1} \int_0^1 \frac{dz_2}{z_2} \int d^2\mathbf{k}_{T,1} \int d^2\mathbf{k}_{T,2} \mathcal{A}(x_1, \mathbf{k}_{T,1}, \mu^2) \mathcal{A}(x_2, \mathbf{k}_{T,2}, \mu^2) \hat{\sigma}(x_1, x_2, z_1, z_2, \mathbf{k}_{T,1}, \mathbf{k}_{T,2}) \quad (4.5)$$

Next chapter will clarify how the cross section can be determined from the partonic matrix element and the TMD PDFs. As the expression above shows, one unintegrated PDF \mathcal{A} is needed for each interacting hadron, which makes the Sudakov form factor appear twice in the calculation of the cross section. In the CSS formalism, the factor only appeared once in expression (3.7). Therefore Δ_a will have to be compared to $\sqrt{S_a}$. Following the definitions of the perturbative expansions of the regarded functions, this means that

$$\begin{aligned} A_a^{(n)} &= \frac{1}{2^n} k_a^{(n-1)} \\ B_a^{(n)} &= -\frac{1}{2^{n-1}} d_a^{(n-1)} \end{aligned} \quad (4.6)$$

for the two Sudakov form factors to be equal. The factor $1/2^n$ appears due to a difference in the definition of the expansions. In the PB formalism, in each term appears a power of $\frac{\alpha_S}{2\pi}$, while in the CSS formalism it is just $\frac{\alpha_S}{\pi}$. An additional factor 2 appears for $d_a^{(n)}$ due to the square root of S_a .

Since the next part will focus on the Drell-Yan process, only the coefficients for quarks will be considered in the comparison below.

4.1.1 LL order

As mentioned in the chapter on the CSS formalism, for LL accuracy only the $A_q^{(1)}$ coefficient is needed, which was equal to C_F . The $k_q^{(0)}$ coefficient of the PB formalism is equal to $2C_F$. This meets the requirements of (4.6) and therefore the Sudakov form factors are equal at LL accuracy.

4.1.2 NLL order

For NLL accuracy, the $A_q^{(2)}$ and $B_q^{(1)}$ coefficients are needed. These are given by:

$$\begin{aligned} A_q^{(2)} &= C_F \left(\frac{67}{18} - \frac{\pi^2}{6} \right) C_A - \frac{5}{9} N_f C_F \\ B_q^{(1)} &= -\frac{3}{2} C_F \end{aligned} \quad (4.7)$$

The coefficients for the PB formalism corresponding to these are:

$$\begin{aligned}
k_q^{(1)} &= 2C_F C_A \left(\frac{67}{18} - \frac{\pi^2}{6} \right) - 2C_F T_R N_f \frac{10}{9} \\
d_q^{(0)} &= \frac{3}{2} C_F
\end{aligned} \tag{4.8}$$

Since $T_R = 1/2$, the $A_q^{(2)}$ and $k_q^{(1)}$ indeed differ from each other by a factor of 2. The $B_q^{(1)}$ and $d_q^{(0)}$ only differ by a minus sign, meaning that they also meet the conditions of (4.6). This means that at NLL accuracy, the two Sudakov form factors still remain the same.

4.1.3 NNLL order

At the moment, the study of the NNLL terms is still ongoing. In the results above, only the Sudakov form factor has been compared. For a full comparison at a certain logarithmic accuracy, one would have to take into account the corresponding perturbative coefficients of the remaining functions H_q^F and C_{ab} in the CSS formalism. This however causes a problem, since the PB formalism does not contain any functions that can be directly related to these. Such inconveniences appear more often when studying the relation between two formalisms. One example of simplifying the comparison is by considering so called NNLL' coefficients, where the H and C functions are neglected. This has been done in [35] by comparing the $B_q^{(2)}$ and $d_q^{(1)}$ terms, which are of order α_S^2 and therefore have a shorter expression than the $A^{(3)}$ and $k^{(2)}$ terms. The considered terms are:

$$\begin{aligned}
B_q^{(2)} &= C_F^2 \left(-\frac{3}{16} + \frac{\pi^2}{4} - 3\zeta(3) \right) + C_F C_A \left(-\frac{193}{48} + \frac{11}{36}\pi^2 + \frac{3}{2}\zeta(3) \right) + C_F N_f \left(\frac{17}{24} - \frac{\pi^2}{18} \right) \\
d_q^{(1)} &= C_F^2 \left(\frac{3}{8} - \frac{\pi^2}{2} + 6\zeta(3) \right) + C_F C_A \left(\frac{17}{24} + \frac{11\pi^2}{18} - 3\zeta(3) \right) - C_F T_R N_f \left(\frac{1}{6} + \frac{2\pi^2}{9} \right)
\end{aligned} \tag{4.9}$$

At first sight, the two terms don't meet the condition of (4.6). The difference that arises is:

$$\begin{aligned}
B_q^{(2)} + \frac{1}{2}d_q^{(1)} &= C_F C_A \left(\frac{11}{18}\pi^2 - \frac{11}{3} \right) + C_F T_R N_f \left(\frac{4}{3} - \frac{2}{9}\pi^2 \right) \\
&= \frac{\pi^2}{6} C_F \left(\frac{11}{3} C_A - \frac{4}{3} T_R N_f \right) - \frac{1}{3} C_F (11C_A - 4T_R N_f)
\end{aligned} \tag{4.10}$$

In both terms, the expression for $\beta_0 = \frac{1}{12}(11C_A - 4T_R N_f)$ appears

$$\begin{aligned}
B_q^{(2)} + \frac{1}{2}d_q^{(1)} &= 4\pi\zeta(2)C_F\beta_0 - 4\pi C_F\beta_0 \\
&= 4\pi C_F\beta_0(\zeta(2) - 1)
\end{aligned} \tag{4.11}$$

The difference is proportional to the β_0 function. The purpose of writing it like this, is because this β_0 can be linked to the change of the B_q function under resummation scheme transformations. As was pointed out in the chapter on the CSS formalism, the B_q function depends on the used resummation scheme. It transforms as (Eq.(3.16))

$$B_c^F(\alpha_S) = B_c(\alpha_S) - \beta(\alpha_S) \frac{d \log H_c^F(\alpha_S)}{d \log \alpha_S} \tag{4.12}$$

The PB functions k_q and d_q were not defined for a particular process or specific scheme, which makes these functions unaltered. The A_q function is also independent of the resummation scheme, which explains why it agrees with the k_q coefficients. The used expression for $B_q^{(2)}$ in the comparison with $d_q^{(1)}$ is valid for the Drell-Yan scheme, where $H_q^{DY} = 1$ was chosen. Expanding the expression above in terms of α_S gives (recalling the perturbative expansion of H_c^F in (3.10)):

$$B_c^F(\alpha_S) = B_c(\alpha_S) - \left(-\beta_0\alpha_S^2 - \beta_1\alpha_S^3 + \mathcal{O}(\alpha_S^4) \right) \left(\frac{H_c^{(1)F}}{\pi} + \frac{2\alpha_S}{\pi^2} H_c^{(2)F} + \mathcal{O}(\alpha_S^2) \right) \tag{4.13}$$

This immediately also shows why the $B_q^{(1)}$ and $d_q^{(0)}$ did coincide, since the lowest power of α_S in the second term is α_S^2 . Performing a resummation scheme transformation would alter $B_q^{(2)}$ as follows:

$$B_q^{(2)F} = B_q^{(2)} + \pi\beta_0 H^{(1)F} \quad (4.14)$$

This shows that the difference between $B_q^{(2)}$ and $d^{(1)}$ can be connected to a resummation scheme. The obtained difference can also be found back in [41]. This implies that the $B^{(2)}$ part of the resummation is included for the PB calculations at NLO (which uses $k^{(1)}$ and $d^{(1)}$), although there is a difference. Current research tries to include more of the NNLL resummation into the PB method and to obtain a better understanding of the scheme dependence of the $B^{(2)}$ coefficient.

Two different approaches are being considered into introducing the $A^{(3)}$ coefficient into the PB calculations. The first one is by performing the calculations at NNLO, which would include the $k^{(2)}$ and $d^{(2)}$ coefficients. The $k^{(2)}$ and $A^{(3)}$ do not coincide as was the case for lower order coefficients. More importantly, using the NNLO splitting functions causes discontinuities to appear in the PDFs [42].

Another approach would like to follow the procedure from [39]. In this paper, a physical coupling α_S^{phys} is being introduced, which is related to α_S in the following way:

$$\alpha_S^{phys} \equiv \alpha_S \left(1 + \sum_{n=1}^{\infty} \left(\frac{\alpha_S}{2\pi} \right)^n K^{(n)} \right) \quad (4.15)$$

The coefficients $K^{(1)}$ and $K^{(2)}$ can be found back in [39]. This physical coupling approach is an extension of the CMW coupling α_S^{CMW} [43], which only includes the $K^{(1)}$ coefficient. This coupling has been used to reproduce results at NLL accuracy with a Monte Carlo coherent branching algorithm for semi-inclusive processes like Drell-Yan and DIS. This branching algorithm is similar to the idea behind the PB formalism. The cascade of partons is generated through the use of splitting functions, which give the possibility for a parton to split into two new partons, and Sudakov form factors, which give the possibility for no-branching. The coherent branching has also already appeared in Chapter 3, in the discussion on the angular ordering. The colour coherence effect caused an angular constraint on successive parton emissions, making the branching angle decrease when moving from the hard scattering towards the initial-state partons.

Calculations made by S. Catani et al. from [43] show that by using the two-loop expression for α_S (see Eq.(1.11)) and the splitting functions from the DGLAP equations up to second order in the branching algorithm, the same results are obtained as for resummation up to NLL accuracy. The splitting functions $P_q(z, \alpha_S)$ are hereby approximated to only include the K_{ab} term from (3.22), since the other terms can be neglected when considering the soft limit ($z \rightarrow 1$):

$$P_q(z, \alpha_S) = \frac{1}{1-z} C_F \frac{\alpha_S}{\pi} \left(1 + k_q^{(1)} \frac{\alpha_S}{2\pi} \right) \equiv \frac{1}{1-z} C_F \frac{\alpha_S^{CMW}}{\pi} \quad (4.16)$$

In [39], α_S^{CMW} is expanded to α_S^{phys} to take into account correlated soft contributions at higher accuracies, determined by the used order for K in (4.15). With the knowledge of $K^{(1)}$ and $K^{(2)}$, Banfi et al. [39] were able to reproduce results from resummation at NNLL accuracy with the physical coupling for two-jet observables in electron-positron annihilation.

The above procedure takes into account the radiation of soft and collinear gluons by introducing an effective/physical coupling. Such effective field theories are often used in the low-energy region to still make it possible to come up with predictions, even though perturbation theory fails due to the large coupling at low energies. A connection can be seen between the description for CMW coupling and the PB method, because both involve a generation of parton splitting. This would imply that it should be possible to apply a similar procedure to the PB method. Even better, from the results of [39] and [43], it becomes clear that the $A^{(3)}$ coefficient can be recovered in the PB method by using the physical coupling together with NLO splitting functions. This means that the discontinuities, that appeared in the other approach, would not be observed in this attempt. This is still work in progress.

Chapter 5

Numerical comparison

Previous chapter discussed the analytical comparison between the CSS and the PB formalism. The CSS approach formulates a method to resum the large perturbative terms up to a certain logarithmic accuracy. A similar decomposition is also present in the PB method, but here it is more difficult to carry out the logarithmic power counting over the whole evolution equation due to the splitting functions, which are truncated at a power of α_S . The analytical comparison however showed that there are similarities between the perturbative coefficients that appear in the Sudakov form factors. In this chapter, a description of the numerical differences is given.

This chapter contains the main outcome of the thesis, which is a systematic study of calculations performed with the CSS approach and the PB approach at different orders in the strong coupling (PB case) and different orders in the resummed cross section (CSS). These will in general not correspond to each other due to different procedures for the decomposition into the separate orders. This review is of great interest for general studies of transverse momentum dependencies. All formalisms have their way of defining the leading contributions together with the corrections. Besides that, they are all constructed within certain limits on the kinematic variables, meaning that they each could perform differently depending on the considered region in phase space. The PB formalism has the advantage of being well suited over a broad range of kinematic variables to obtain TMD PDFs, while the resummation procedure of the CSS approach is only valid for $q_T \ll Q$. To obtain predictions for larger values of q_T , a matching procedure with a finite term has to be applied.

For this project, the predictions from both formalisms will be studied for the Drell-Yan cross section as function of the transverse momentum of the created Z boson. Contributions arising from a virtual photon or W^\pm bosons will be neglected. The obtained TMD PDF from the PB method is matched with a fixed-order matrix element to acquire a solution for the cross section, so that results from both formalisms can be compared directly.

This project was mainly focused on learning how to use the program reSolve [44], which implements the CSS formalism. Although this formalism has already been established a long time ago and several programs have already been developed for these calculations, the reSolve program is rather new. At the moment, a matching procedure is not yet fully available for higher values of q_T . Therefore it will be more interesting to study the reSolve results at low q_T . For the PB formalism, the TMD PDFs are provided through TMDlib [45], which gathers together TMD PDFs from different formalisms. The published TMD PDF sets from the PB method are used here. These sets have already been constructed by the procedure explained in Section 4.3-4.4. Through the use of CASCADE [46], a Monte Carlo event generator, the TMD PDF is combined with a LO or NLO matrix element to calculate the differential cross section.

The mentioned programs will be used to produce the transverse momentum spectrum of the cross section for the Drell-Yan process through the creation of a Z boson.

5.1 reSolve

To obtain numerical results for the CSS formalism, a new C++ program reSolve [44] will be used. Multiple programs already exist that implement the resummation procedure, but these are usually focused on a specific process. For the production of a diphoton pair, there is the program 2gres and the resummation for the Drell-Yan cross section can be calculated with DYRes. The motivation behind the reSolve program is to provide the resummation for multiple processes. These processes would be inclusive hadron-hadron interactions where the considered final state consists of particles that do not interact strongly. The CSS formalism from Chapter 3 was set up for this type of processes. At the moment, only the resummation procedure for diphoton production and the Drell-Yan process are implemented up to NNLL accuracy. The code for these processes is based on the programs 2gres and DYRes.

The implementation of the resummation procedure in reSolve follows the description of the CSS formalism from Chapter 3. The expression for the cross section is

$$\begin{aligned} \frac{d\sigma_{res}^F(p_1, p_2, Q^2, \mathbf{q}_T, y, \Omega)}{d^2\mathbf{q}_T dQ^2 dy d\Omega} &= \frac{Q^2}{s} \sum_c \sigma_{c\bar{c}, F}^{(0)} \int d^2\mathbf{b} \frac{e^{i\mathbf{b}\cdot\mathbf{q}_T}}{4\pi^2} S_c(Q, b) \\ &\times \sum_{a,b} \int_{x_1}^1 \frac{dz_1}{z_1} \int_{x_2}^1 \frac{dz_2}{z_2} H_c^F(x_1 p_1, x_2 p_2, \Omega, \alpha_S(Q^2), \mu_R) \\ &\times C_{ca}(z_1, \alpha_S(b_0^2/b^2)) C_{\bar{c}b}(z_2, \alpha_S(b_0^2/b^2)) f_{a/A}(x_1/z_1, b_0^2/b^2) f_{b/B}(x_2/z_2, b_0^2/b^2) \end{aligned} \quad (5.1)$$

A slightly different expression is being used compared to Eq.(3.7). Here the cross section has additional dependencies on the rapidity y and extra variables represented by Ω . This extensive definition of the cross section offers a complete description for the phase space of the final state F . The total four-momentum of F can namely be extracted from \mathbf{q}_T , Q and y . The variables collected in Ω are used to define the four-momenta of each individual particle of F . In case of the diphoton production, this would be the azimuthal and polar angle of one of the photons.

The only factors in expression (5.1) that are process-dependent, are the H_c^F function and the Born cross section of the hard process $\sigma_{c\bar{c}, F}^{(0)}$. This gives the possibility to construct the program in such a way that adding a new process would only require to implement of these functions. This is exactly what reSolve has accomplished. A new version of the program (not public yet) has for example the implementation for Z' production and results have already been published [47].

The Sudakov form factor in Eq.(5.1) has the same expression as in (3.9), which does not depend on the process. This factor carries out the resummation of large logarithms $\log(b^2 Q^2)$. By working out the integral, one obtains the decomposition in contributions from different logarithmic accuracies, as shown in (3.13). The $g^{(n)}$ functions appearing here each represent one of these contributions. Expressions for $g^{(1)}$ (LL), $g^{(2)}$ (NLL) and $g^{(3)}$ (NNLL) can be found back in [29, 44]. Depending on the desired accuracy, the program then calculates the corresponding $g^{(n)}$ functions.

Two additional b -dependencies are present outside of the Sudakov form factor. Both the PDFs and the C_{ab} functions depend on b through the factorization and renormalization scales and will therefore still contain the large logarithms. In chapter 3, it has been mentioned that this dependency can be extracted by using the evolution operator for both functions. Expressions for these contributions can be found back in [29, 44] and are included in the reSolve calculation.

Although the Sudakov form factor is universal, it does depend on the used resummation scheme through the B_c function. The same applies to the H_c^F and the C_{ab} functions. The current version of reSolve uses the Drell-Yan scheme, meaning that H_c^{DY} is equal to 1. For the diphoton production, this function will have a different expression. This is however not relevant for this thesis, because only the Drell-Yan process will be

studied.

To evaluate the cross section from (5.1), reSolve has to deal with four integrals (the integral over \mathbf{b} is two-dimensional). These integrals are solved by a Monte Carlo simulation, similar to what is done in the event generators (see Section 2.3). The Drell-Yan process is azimuthal symmetric, which makes it possible to simplify the two-dimensional integral to:

$$\int \frac{d^2\mathbf{b}}{(2\pi)^2} e^{-i\mathbf{q}_T \cdot \mathbf{b}} \rightarrow \int_0^\infty \frac{db}{2\pi} J_0(q_T b) \quad (5.2)$$

with J_0 being the 0th-order Bessel function. To evaluate the integral over b , reSolve makes use of an external package that is designed to calculate semi-infinite integrals of rapidly oscillating functions [48]. However, the arising singularities for small and large b have to be addressed first. Small values of b correspond to the region of large q_T where the resummation procedure does not hold any longer. A finite term should provide here the contributions for the cross section, while the resummed part should be negligible small. This is achieved by replacing the logarithms L by \tilde{L} , as was shown before in Eq.(3.15). The replacement ensures that the resummed component fades out for small b , while the difference with L at large b is kept small.

The problems that arise for large b can be found in the expressions for the $g^{(n)}$ functions. These expressions contain the variable λ , which represents the logarithms:

$$\lambda = \frac{1}{\pi} \beta_0 \alpha_S(\mu_S^2) \log\left(\frac{\mu_S^2 b^2}{b_0^2}\right) \quad (5.3)$$

The $g^{(n)}$ functions diverge when $\lambda \rightarrow 1$, where $b = b_L$:

$$b_L^2 = \frac{b_0^2}{\mu_S^2} \exp\left(\frac{\pi}{\beta_0 \alpha_S(\mu_S^2)}\right) \quad (5.4)$$

This value for b corresponds to $1/\Lambda_{QCD}$, where Λ_{QCD} refers to the energy scale where the strong coupling becomes very large and perturbation theory can not be used any more. The contributions for $q_T \sim \Lambda_{QCD}$ therefore arise from non-perturbative phenomena. To regularize the integral, reSolve uses a substitution for b to keep it lower than a fixed limit b_{lim} :

$$b \rightarrow b_* = \frac{b}{\sqrt{1 + b^2/b_{lim}^2}} \quad (5.5)$$

where the limit b_{lim} is usually set around 1 or 2 GeV⁻¹ [49]. This upper limit on b would however neglect contributions from non-perturbative processes, which are not necessarily small. reSolve takes these into account by adding a Gaussian smearing to the integrand, contained in the factor S_{NP} :

$$S_{NP} = \exp\left(-g_{NP}^c b^2\right) \quad (5.6)$$

The factor g_{NP}^c differs for $q\bar{q}$ - and gg -initiated hard processes. These non-perturbative contributions can be seen as an intrinsic transverse momentum of the produced final state. Usually a fit is performed with data to obtain a value for the g_{NP}^c factor, but this is not implemented in the current version of reSolve. At the moment one has to take into account that there is an additional uncertainty on the results from reSolve at the lowest region of the q_T spectrum due to the unknown value of g_{NP}^c .

The integrals over z_1 and z_2 are not computed directly. Instead, a Mellin transformation is used to obtain an expression as in Eq.(3.7). This does not contain any z integrals, because they are implied by the moment N of the C functions and the PDFs. The integration is therefore replaced by a simple product. One inconvenience with the PDFs still arises however. These PDFs are obtained from a library (LHAPDF [50]), which are usually given as functions of the momentum fraction x . Thus, an additional procedure has to be provided by reSolve that calculates the Mellin transformation of those PDFs. At the end, the obtained expression in Mellin space is transformed to x -space by using a rapidly converging Gaussian quadrature.

5.2 p_T spectrum of Z boson

Numerical results for the transverse momentum spectrum of the Z boson in the Drell-Yan process will be discussed now. As mentioned earlier in Section 2.1.2, these are of great importance in the determination of the W^\pm boson mass. Besides that, the spectrum is an ideal observable to study resummation techniques for low transverse momenta.

Results for the CSS formalism will be produced by using reSolve. For the PB formalism, several programs contribute to the final result. The TMD PDFs can be accessed through TMDlib [45], a library containing TMD PDFs, calculated by various formalisms. The PB TMD PDFs have been constructed by the program uPDFevolv [51], which has the implementation of the iterative procedure from Section 3.3. For the matrix element, two different MC event generators are used. Pythia [52] provides the matrix element at LO, MCatNLO [53, 54] does this for NLO. The kinematics within these matrix elements are generated according to the PB PDFs. The MCatNLO event generator provides also the matching procedure, which is needed to avoid the double counting of certain contributions, since the matrix element and the TMD PDFs both contain higher order corrections. These different parts are brought together in CASCADE [46], another MC event generator that calculates the cross section using the matrix element and the TMD PDFs. The obtained events are then processed by Rivet [55]. It follows the same procedure as has been described in Section 3.3. The used PB TMD PDFs are evaluated at NLO, which means that they are obtained by using the NLO splitting functions in the evolution equation. For the strong coupling α_S , the two-loop expression is used (β_0 and β_1 in Eq.(1.11)).

Both reSolve and Cascade actually provide an expression for the cross section which depends on additional variables Q and y besides the transverse momentum, as is shown in Eq.(5.1). The cross section has to be integrated over those two variables before obtaining the p_T spectrum. For the following results, these integrals are always evaluated for $66 \text{ GeV} \leq Q \leq 116 \text{ GeV}$ and $|y| < 2.4$.

The predictions from both formalisms are compared to experimental data from the ATLAS detector [56] at energies of 8 TeV. This gives the opportunity to state more clearly how each program performs. For the comparison with data, the characteristics of the experiment have to be reconstructed as well as possible. This explains the used integration boundaries for y , since the detector tracks the produced leptons in this region. The integration of Q takes place around the mass of the Z boson, because these bins are used in the experiment to limit the detection of events caused by other bosons.

5.2.1 Different orders within reSolve

First the different orders implemented in reSolve will be compared to each other. To be sure that the program was installed properly, some results from [44] were reproduced. These will not be discussed here, but they ensured that the produced results for the Z boson can be trusted.

Figure 5.1 shows the p_T spectrum of the Z boson obtained with reSolve at LL, NLL and NNLL accuracy. The uncertainty band is obtained by running the program for different values of the resummation scale μ_S . As stated before, the cross section should be independent of these scales, but due to the truncation of perturbative functions, this is not the case as can be seen. The idea was to vary the scales following a so-called 9-point scale variation, inspired by [47]. The default settings set the renormalization μ_R and factorization scale μ_F equal to the invariant mass Q of the event. These values are then varied by a factor two up and down. This gives nine p_T spectra which are combined into an uncertainty band where the central value represents the default values for the scales. In addition to that, the uncertainty for the resummation scale is usually also calculated by keeping μ_R and μ_F fixed at their default value, while varying the resummation scale with a factor two up and down from the default value. This value is equal to $Q/2$ and thus a factor two less than the default values of μ_R and μ_F , a choice justified by the results from [29]. However, due to technical issues, this 9-point scale variation has not been done for the reSolve results. Only the varying of the resummation scale is included in figure 5.1 and in the other results from reSolve in this chapter. It is however expected that the uncertainty from the resummation scale will be the largest and will therefore

cover up the uncertainty band of the 9-point scale variation. This is a consequence of the absence of the matching procedure in the reSolve program. This would have decreased the μ_S dependence of the reSolve results at intermediate q_T , which is now not the case as can be seen in figure 5.1. The 9-point scale variation has only been done for the results from the PB method, which follows in Section 5.2.4.

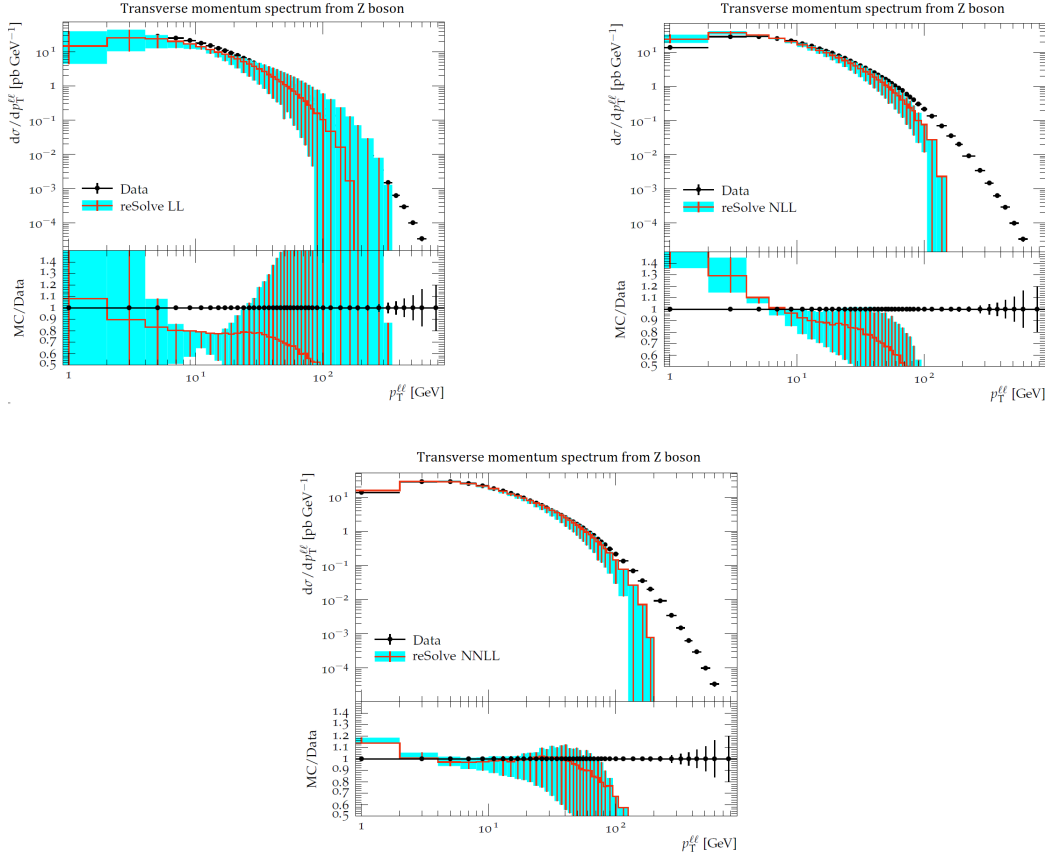


Figure 5.1: Results for the p_T spectrum of the Z boson obtained with reSolve at LL, NLL and NNLL accuracies. The uncertainty band originates from resummation scale variation.

Another input parameter that has to be discussed, is the used PDF set. reSolve extracts this from the LHAPDF library. In analogy with the published results from reSolve in [44], the same PDF sets are used, namely the MSTW2008 LO/NLO/NNLO sets, which are obtained through another procedure than the one considered in this thesis [57]. The orders of the PDF set refer to which order in α_S the splitting functions are evaluated. The LO set is used with the LL resummation and similarly for the higher orders. This is again parallel with [44].

All three plots from figure 5.1 show the result of the resummation procedure. Without this, the cross section would diverge as $q_T \rightarrow 0$. This is no longer the case, as the cross section reaches a maximum value around 3 GeV. The bulk of events is situated in the lower region of q_T , which agrees with the experimental data. This is caused by the emission of virtual and soft gluons.

The validity of the resummation procedure is clearly visible in all three figures. At transverse momenta around 50 GeV, the central value of the reSolve spectra at LL and NLL accuracy already differs from the ATLAS data by more than 20%. The data points are still within the range of the error band at LL accuracy, but the uncertainty is too large for good predictions at these transverse momenta. For NNLL accuracy, the

agreement between results and data holds up to ~ 70 GeV, after that the deviation becomes larger than 20%. As mentioned before, for $p_T \sim Q$, there is need for a finite term to achieve correct results. This final term is still not implemented in reSolve, which explains why the results start to diverge from the experimental data at higher values of p_T .

At intermediate values of p_T , the reSolve results at NLL and NNLL are in good agreement with the data. At LL, the results show a similar shape but there is still a deviation present, even with the uncertainty bands. The NNLL results are an improvement on NLL accuracy. Not only does the central value agree better with the data, the uncertainty band also becomes smaller. This behaviour is expected, although the difference can not be considered to be small. It is also remarkable that the NNLL results still provide excellent predictions up to ~ 40 GeV, while the matching procedure is not implemented in the code. This could imply that this agreement is caused by accident and that NNLL calculations would not always provide such results at higher p_T .

There is however no good agreement between the reSolve results and the data at the lower region of the p_T spectrum. At NNLL accuracy, the results from 1 GeV and upwards till 70 GeV are consistent with the data, but in the lowest bin there is also no overlap between data and the uncertainty band. The resummation procedure should actually produce accurate results for these values of p_T . There is also no clear improvement on the central value when the accuracy is increased. One has to recall that this region corresponds to non-perturbative contributions. In reSolve, an upper limit was introduced for b to deal with the divergences caused by these contributions. To account for this, a Gaussian smearing is implemented in the code. This smearing is however not used for the results in figure 5.1. The next part will study the influence of the smearing to see if this causes the deviation. This could also explain why the anomaly is observed at each order.

5.2.2 Influence of non-perturbative smearing in reSolve

To study the impact of the Gaussian smearing, the parameter g_{NP}^q from Eq.(5.6) is varied. For the results from figure 5.1, the value for this parameter was just zero. The same calculations were repeated with values 1.67 GeV^2 and 5.64 GeV^2 . These values were also used in [29] to analyse the influence of the smearing.

The results combined for these three values of g_{NP}^q at NNLL accuracy are displayed in the left plot of figure 5.2. The plot shows that varying the exponent of the Gaussian smearing affects the spectrum clearly in the lower bins. However, the green curve ($g_{NP}^q=5.64 \text{ GeV}^2$) shows that the influence of the Gaussian smearing also extends to 30-40 GeV, which is far above the boundary which separates the non-perturbative and perturbative parts from each other. One has to note that the g_{NP}^q parameter corresponds to the width in b -space, while the results are shown in p_T -space. Performing the Fourier transformation on the expression in (5.6) results in a width that is four times the g_{NP}^q parameter. The value 5.64 GeV^2 for this parameter is therefore considered to be too large.

Using this Fourier transformation, it is also possible to use a Gaussian smearing that is comparable to the one used in the PB calculations, which has been described by Eq.(3.58). The results for the PB method are obtained using a width $\sigma^2 = 0.125 \text{ GeV}^2$, which in b -space should correspond to $g_{NP}^q = 0.03125 \text{ GeV}^2$. Results with this smearing are also shown in figure 5.2 (right plot), but they barely differ from the results without smearing.

As mentioned before, the value of g_{NP}^q should be fitted to data first before reSolve can produce reliable results for the lowest p_T region. It is also important that the smearing would not influence the cross section at higher values of p_T , which excludes the use of $g_{NP}^q = 5.64 \text{ GeV}^2$. The other curves from 5.2 also do not show an improvement on the spectrum in the lowest bins. Since no conclusion can be made on which value for g_{NP}^q should be used, the Gaussian smearing is not included in the numerical comparison between the CSS and PB formalism, which follows.

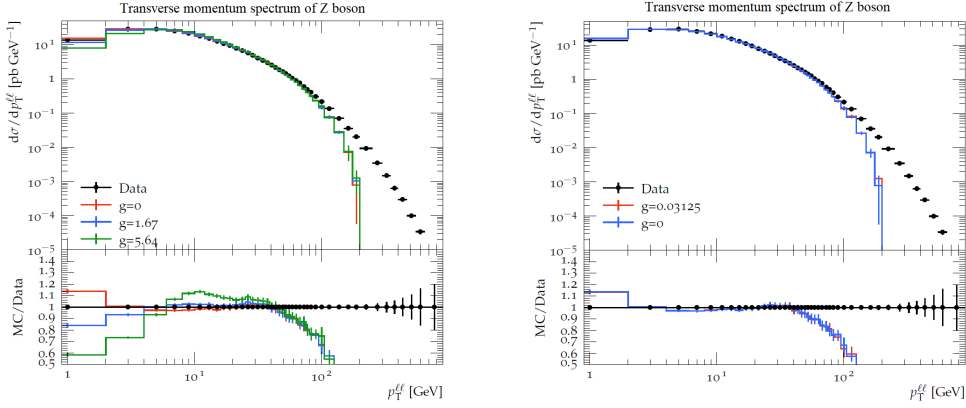


Figure 5.2: p_T spectra calculated for different values of the Gaussian smearing parameter g_{NP}^q , which takes non-perturbative contributions into account.

5.2.3 Use of PDF set

One small comment has to be made on the choice of PDF sets before comparing the two formalisms. Previous figures showed results from reSolve obtained by using the MSTW PDF sets. The PB formalism is however able to provide collinear PDF sets, besides the TMD PDF sets, that can also be used in reSolve. This is exactly what is done to obtain the results in figure 5.3. This figure compares the p_T spectra at NLL accuracy between results from reSolve with different PDF sets. For both curves, the NLO PDF set is used. More precisely for the PB PDF set, it is the PB-TMDNLO-HERAI+II-2018-set2 set. The uncertainty bands are again constructed by performing the 9-point scale variation, the same as in figure 5.1.

The plot does not show any noticeable differences between the two curves, although the deviation from the ATLAS data becomes even bigger in the lowest bins when using the PB PDF set. This PDF set is nonetheless used when comparing the results for the cross section between the two formalisms. To optimize the comparison, the initial parameters for the used programs should agree as well as possible. Since one of these parameters is the used PDF set, the reSolve results are produced with the same PB PDF set as the PB results. The observed difference from figure 5.3 should not be taken into too much consideration. Figure 5.2 already showed that in order to obtain reliable results from reSolve at the lowest bins, a fit is needed to determine the exponent in the Gaussian smearing.

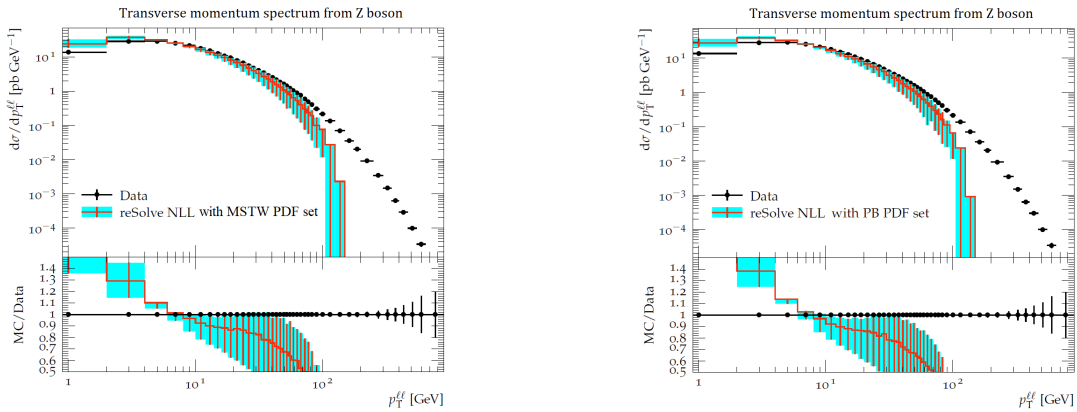


Figure 5.3: p_T spectra for the Z boson calculated with reSolve at NLL accuracy, where different PDF sets were used. The left figure shows the results for using the MSTW PDF set, the right one shows it for the PB PDF set. The uncertainty bands originate from resummation scale variation.

5.2.4 Comparison between PB and reSolve

Figures 5.4 and 5.5 collect the spectra for the main discussion of the thesis. Results for the CSS and PB formalisms are compared against each other at similar orders. Figure 5.4 shows the results for the PB approach with a LO matrix element and for reSolve at LL accuracy. The results for the next order, which is the use of a NLO matrix element for the PB formalism and reSolve up to NLL accuracy, are displayed in figure 5.5. This also includes the NNLL accuracy results for reSolve.

All spectra are produced with the same PDF set, namely the PB NLO set. Up till now, the reSolve results were produced with some sort of matching between the order of the PDF set and the accuracy of the resummation (LO with LL, NLO with NLL, NNLO with NNLL), but this was done to work analogous to the published results in [44]. The order of the used PDF set does not actually improve the accuracy of the numerical results by a significant amount. For this, a higher order matrix element or resummation up to the next logarithmic accuracy is needed. Therefore, using a NLO PDF set for the reSolve results at LL accuracy does not cause any inconveniences.

One additional remark on the uncertainty bands has to be made. For the reSolve results, these are again obtained by carrying out the 9-point scale variation. For the PB results, this was not possible to do. First of all, the PB formalism does not have a resummation scale, this is something specific to the CSS formalism. It does have a so-called matching scale, which determines the part of the spectrum where the TMD PDF or the fixed-order matrix element dominates. The matching scale is provided by MCatNLO and this usually is not varied because it causes a large uncertainty. The 9-point scale variation could therefore not be applied in the same way for these results. Instead, a similar variation has been performed for only the renormalization and factorization scales in figure 5.5. Contrary to the uncertainty bands on the results from reSolve, these two scales are not kept equal to each other. Also a different default value is used. In the PB formalism, the two scales are by choice set equal to the transverse mass, defined as $\sqrt{Q^2 + p_T^2}$.

Figure 5.4 does not contain the scale variation due to technical issues. Instead, the displayed errors originate from an uncertainty which is specific to the PB formalism. This is caused by experimental and model alterations when performing the fit, resulting in variations in the PDF set. These are called TMD variations. These are also shown in figure 5.5, together with the scale variation.

The most notable difference between the two formalisms is the behaviour at high p_T values. As mentioned before, the reSolve results drop down to zero due to the missing finite contribution. This can be observed in both figures 5.4 and 5.5. The bulk of events however is not located in the higher part of the p_T spectrum. Therefore it is more interesting to study the cross section at low and intermediate values of p_T .

The uncertainty bands for the spectra at lowest order in figure 5.4 differ clearly from each other. For the reSolve results, these are created by the usual scale variation, while the TMD variations cause the error on the PB results. The central values do display a similar behaviour at intermediate p_T values (between 5 and 50 GeV). The difference between the numerical values and the ATLAS data does not change greatly in this interval, but stays rather constant around 20-30%. The fact that the spectrum seems to be a constant factor off from the data has been noted in previous results for the PB formalism. Figure 5.4 shows that the reSolve results at LL accuracy depict a similar behaviour, although spread out over a shorter region of the p_T spectrum. Normalizing the p_T spectra is one way of dealing with this factor. This normalization is obtained by dividing the spectrum by the total cross section. This was however too difficult to do with the results produced by reSolve.

At low transverse momenta, the issue arises that reSolve does not have the non-perturbative smearing fitted yet. The excess in the lowest bin is not observed in the PB results, since the intrinsic transverse momentum is treated in these calculations. A similar Gaussian function is introduced hereby to take into account the non-perturbative contributions. This distribution is given by $\exp\left(\frac{-|p_T|^2}{\sigma^2}\right)$, with σ^2 set equal to 0.125 GeV^2 . The curve still does not agree with the data in the lowest bin, but this is caused again by the constant factor which is dealt with after normalization.

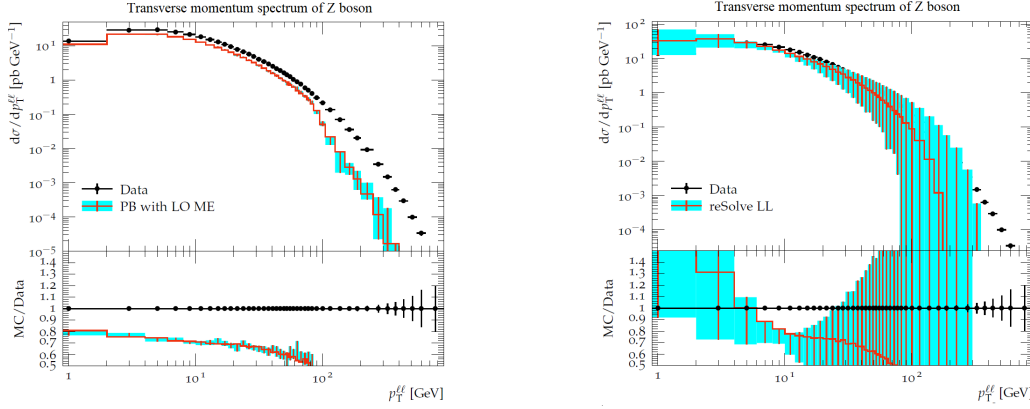


Figure 5.4: p_T spectra produced with the PB formalism including a LO matrix element (ME) (left) and with reSolve at LL accuracy (right). The uncertainty band for the PB results originates from TMD variations, while the errors on the reSolve results are caused by resummation scale variations.

The results at higher order in figure 5.5 are more useful. The scale variation can now be performed for the PB results, which helps with the comparison. The uncertainty band from this variation is smaller compared to the reSolve results, because there is no variation of the resummation scale for the PB results. The TMD variation on these results is also displayed and it only becomes notable at large p_T . This indicates that higher order terms are needed to obtain reliable predictions at high p_T . Using the NLO matrix element is already a big improvement compared to figure 5.4 thanks to higher order corrections which are now taken into account, but the TMD variations show that there is still room for improvement on the higher part of the spectrum. The lower part of the spectrum is however more interesting for the comparison with results from reSolve.

The difference between the PB predictions and the data stays below 10% up to 50 GeV in figure 5.5 and the uncertainty band on the reSolve spectrum encloses the data points in the region between 6 and 50 GeV. However, as the transverse momentum grows and the curve drops, the error on the calculated values from reSolve becomes larger. This is another consequence of the missing finite term, since this makes the spectrum depend more on the resummation scale. This would have been cancelled after applying a matching procedure with the large p_T contribution. A similar matching procedure is present in the PB calculations and this causes the appearance of a bump around 30 GeV in the p_T -spectrum, as is visible in the ratio plot. It actually creates an overshoot around this value of the transverse momentum. This excess should be corrected by higher orders, as the uncertainty band tells.

Figure 5.5 also includes the results at NNLL accuracy. These have been included because they show a better agreement with the PB results than the reSolve results at NLL accuracy. Note that this is not the same curve as the one in 5.1, since the PB PDF set is being used here instead of the MSTW one. The fact that the NNLL results are more similar to the NLO results from PB can be explained by the results obtained from the analytical comparison in Chapter 5. The TMD PDF at NLO includes the $d^{(1)}$ coefficient, which is a higher order correction for virtual contributions. This can be seen from the decomposition of the splitting functions in Eq.(3.22). The $d^{(n)}$ coefficients appear in the term proportional to $\delta(1-z)$, which represents contributions that do not change the momentum of the parton. This is what happens in virtual emissions, when a gluon is emitted and absorbed back again. Chapter 5 showed that the $d^{(1)}$ coefficient can be compared to the $B^{(2)}$ coefficient from the CSS formalism. Although the precise relation between those two coefficients is still being studied, they do represent similar contributions. These contributions are not yet included in the reSolve calculations at NNLL accuracy, since the $B^{(2)}$ coefficient only appears at NNLL accuracy. The addition of the virtual contributions at a higher order therefore seems to improve the results considerably. Besides $d^{(1)}$, the PB calculations at NLO also include the $k^{(1)}$ coefficient, which corresponds

to $A^{(2)}$ from the CSS formalism. This coefficient is however included in calculations at NLL, so this should not cause any difference.

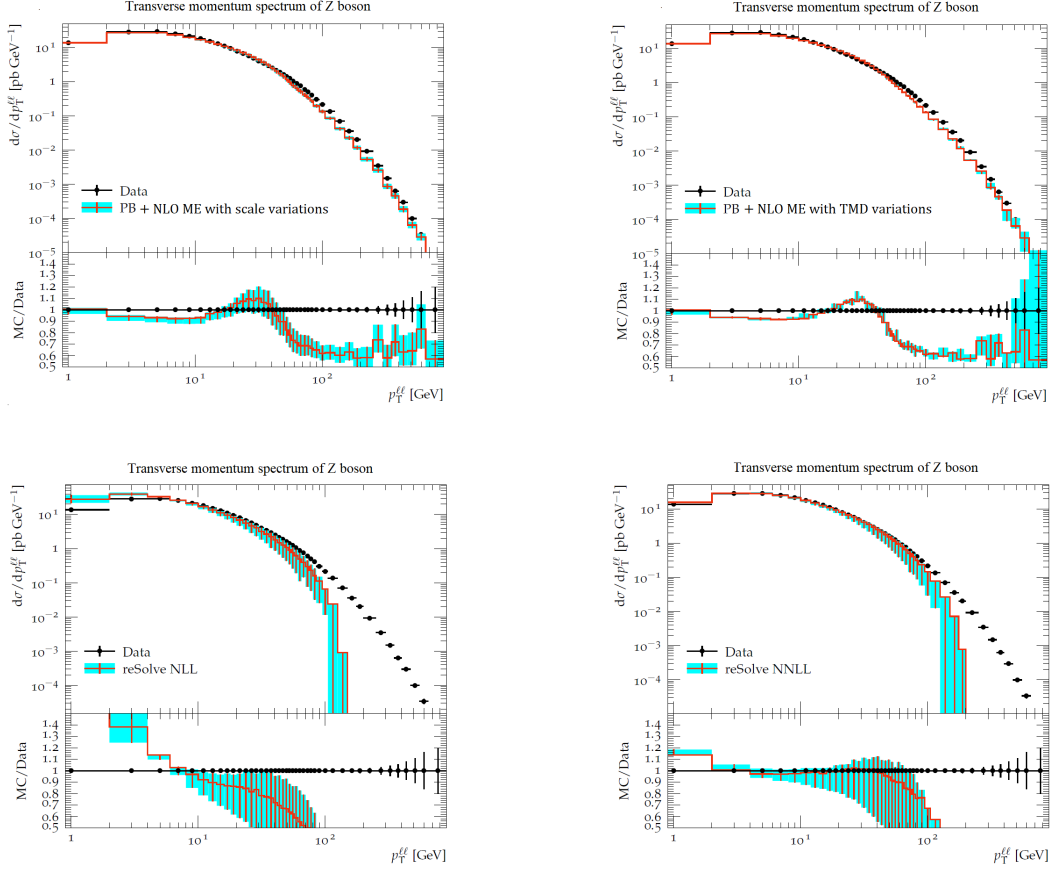


Figure 5.5: The spectrum on the upper row shows the results from the PB method including a NLO matrix element (ME). The uncertainty band for the left figure originates from scale variations, the right figure shows the uncertainty band for the TMD variations. The other two spectra on the bottom row represent results from reSolve at NLL (left) and NNLL (right) accuracy. The uncertainty bands are produced by varying the resummation scales.

Conclusion

The running coupling constant of QCD makes it impossible to describe the strong interaction with perturbation theory at low energies. Interactions between hadrons, which take place in the LHC, always contain contributions from these non-perturbative effects, even though the hadrons collide at high energies. This prevents the calculation of the cross section of these interactions with a perturbative expansion. The factorization theorem however provides the possibility to split the expression of the cross section into a high-energy and low-energy part. The first one can be calculated perturbatively, the second one is represented by PDFs which portray the inner structure of hadrons. Excellent results can be obtained through collinear factorization, although it fails for processes characterized by multiple scales, which indicates the need for TMD factorization. This improved accuracy is needed in order to be able to compare the measured data from experiments with theoretical predictions in search of flaws within the Standard Model.

Two different TMD formalisms have been studied in this thesis. The well-established and commonly-used CSS formalism describes the low q_T factorization and has been introduced to correctly calculate the transverse momentum spectrum of the Z boson in the Drell-Yan process. Nowadays this approach has been extended for calculations of inclusive processes. Contributions from soft gluons, that cause logarithmically enhanced terms in the perturbative expansion of the partonic cross section, are resummed to all orders in α_S by the Sudakov form factor. The relative new but very promising PB formalism is not introduced for a certain process but modifies the DGLAP equations in order to obtain evolution equations for TMD PDFs. These equations can be solved through a MC technique to obtain the TMD PDFs for all partons over a broad kinematic range. The acquired TMD PDFs can then be used within MC event generators to obtain precise descriptions for inclusive and exclusive processes. Despite the differences between the two formalisms, they both aim to acquire precise predictions for QCD collider observables.

This thesis provides a thorough analytical and numerical comparison between the CSS and the PB formalism. First the perturbative functions inside the Sudakov form factors from the two approaches have been analysed. Up to NNLL, this study had been performed recently. It shows that the LL and NLL coefficients correspond to each other, while a difference is observed between the $B_q^{(2)}$ (CSS) and the $d_q^{(1)}$ coefficients. This difference can be rewritten into an expression which is proportional to the β_0 coefficient, indicating that it originates from a resummation scheme transformation of the $B_q^{(2)}$ coefficient. Current research however tries to introduce a physical coupling constant into the PB formulation in analogy with [43] and [39]. By including this, the $A^{(3)}$ CSS coefficient would be present in the PB calculations, meaning that this part of NNLL resummation would be incorporated in the PB method. In [43] for example, it is shown that generating a cascade of partons with NLO splitting functions reproduces the same results as NLL resummation would do. Since the PB approach is similar to how branching algorithms work, it should be possible to implement the same procedure into the formalism.

The main results of this thesis have been displayed in Chapter 5, which contains the numerical comparison between the two formalisms. For PB results, the TMD PDF set PB-NLO-HERAI+II-2018-set2 is used combined with either a LO matrix element (obtained from PYTHIA) or a NLO matrix element (obtained from MADGRAPH5 AMC@NLO). To acquire results for the CSS approach, the program reSolve has been studied, which implements the formalism. It has only been developed recently and is still under construction.

In this thesis, it has been achieved to obtain predictions for the p_T spectrum of the Z boson with the PB

approach and the reSolve program. Results were obtained for energies at 8 TeV and compared to measurements from the ATLAS experiment. From the produced spectra, several conclusions can be made.

It was not evident to compare how the two formalisms perform at a similar accuracy. In reSolve this is determined by whether the LL ($A^{(1)}$), NLL ($A^{(2)}$ and $B^{(1)}$) or NNLL ($A^{(3)}$ and $B^{(2)}$) coefficients are included in the calculations. Although similar coefficients are present in the PB formalism, the order is established through the splitting functions, which are either truncated at LO or NLO. From the analytical comparison, it had been concluded that the LO coefficients correspond to $A^{(1)}$ and $B^{(1)}$ and that the NLO coefficients are related to $A^{(2)}$ and $B^{(2)}$. The numerical results obtained from the PB approach and reSolve indeed show similarities when the $d^{(1)}/B^{(2)}$ coefficients are included in the calculations. The results therefore display that a part of the NNLL resummation is present in the NLO predictions from the PB method.

The produced spectra also show that both approaches can still improve. The reSolve program does not have the matching procedure yet to obtain reliable results at high q_T . For the non-perturbative q_T region, a Gaussian smearing is present in the code, but the width has not yet been obtained from fits to data. Therefore the reSolve results are mostly useful at intermediate q_T for the moment.

The uncertainty on the matching scale, used to combine NLO matrix elements with the PB TMD PDFs, has not yet been analysed. Besides that, the accuracy on the PB results can be improved by implementing the $A^{(3)}$ coefficient into the calculations, so that a larger part of the NNLL resummation would be present. The analytical comparison discussed two possible approaches in order to achieve this.

This thesis thus provides the first numerical comparison between the CSS and the PB approach. These results are of great importance for the community involved in these TMD formalisms. They help to understand the details of the resummation procedure. The produced figures have illustrated that the PB results can produce results of the same quality as the CSS formalism does.

Bibliography

- [1] R.K.Ellis, W.J.Stirling, and B.R.Webber, *QCD and Collider Physics*, Cambridge University Press, 1996.
- [2] F. Mandl, and G. Shaw, *Quantum Field Theory*, Wiley, 2010.
- [3] F. Halzen, and A.D. Martin, *Quarks and Leptons: An Introductory Course in Modern Particle Physics*, Wiley, 1984.
- [4] D. Griffiths, *Introduction to Elementary Particles*, Wiley, 1987.
- [5] M. Thomson, *Modern Particle Physics*, Cambridge University Press, 2013.
- [6] J. Tempere, *Quantum Field Theory*, Course notes, University of Antwerp, Faculty of Sciences, Department of Physics, academy year 2018-2019.
- [7] S. Leupold, *Quantum Chromodynamics and Effective Field Theory*, Uppsala University, Department of Physics and Astronomy, academy year 2018-2019.
- [8] D. J. Gross, F. Wilczek, Phys. Rev. Lett. 30, 1343 (1973).
- [9] CERN collaboration, *LHC, the guide*, CERN Brochure, February 2017 https://home.cern/sites/home.web.cern.ch/files/2018-07/CERN-Brochure-2017-002-Eng_0.pdf.
- [10] A. K. Chaudhuri, *A short course on Relativistic Heavy Ion Collisions*, July 2012, arXiv:1207.7028 [nucl-th].
- [11] J.C. Collins, D.E. Soper, and G. Sterman, Adv.Ser.Direct.High Energy Phys.5:1-91,1988, arXiv:hep-ph/0409313v1.
- [12] J. D. Bjorken, Phys. Rev. 179, 1547.
- [13] I. R. Kenyon, Rep. Prog. Phys. 45 (1982) 1261.
- [14] A. Lelek, *Determination of TMD parton densities from HERA data and application to pp processes*, PhD Thesis, Universität Hamburg, Fachbereich Physik, 2018.
- [15] BCDMS collaboration, A.C. Benvenuti et al., *Phys. Lett.* **B223** (1989) 483.
- [16] NMO collaboration, P. Amaudrus et al., *Phys. Lett.* **B295** (1992) 159.
- [17] D.J. Gross, C.H.Llewellyn Smith, Nucl. Phys., B14 (1969), p. 337.
- [18] A.L. Kataev, and A.V. Sidorov, XXIXth Rencontre de Moriond on QCD and HE Hadronic Interactions, Meribel, France, March 1994 arXiv:hep-ph/9405254v1.
- [19] K. Gottfried, Phys. Rev. Lett. **18** (1967) 1154.
- [20] A.L. Kataev, 11th Lomonosov Conference on Elementary Particle Physics, 21-27 August, Moscow State University, Moscow, Russia, arXiv:hep-ph/0311091v1.
- [21] S. Höche, Lectures presented at TASI, 2014, arXiv:1411.4085v2 [hep-ph].

- [22] M.H. Seymour and M. Marx, 69th Scottish Universities Summer School in Physics (SUSSP 69), St. Andrews, 19th August - 1st September 2012, arXiv:1304.6677v1 [hep-ph].
- [23] J. C. Collins, D. E. Soper and G. Sterman, Nucl. Phys. B 250 (1985) 199.
- [24] P. Nason and B. Webber, Ann.Rev.Nucl.Part.Sci. 62 (2012), arXiv:1202.1251 [hep-ph].
- [25] R. Angeles-Martinez et al., Acta Phys. Polon. B46, 2501 (2015), arXiv:1507.05267 [hep-ph].
- [26] S. Catani, M. Ciafaloni, and F. Hautmann, Nucl. Phys. B366, 135 (1991).
- [27] R. D. Ball et al., JHEP 04 (2015) 040.
- [28] S. Catani, D. de Florian and M. Grazzini, Nucl.Phys. B596, 299-312 (2001) arXiv:hep-ph/0008184v2.
- [29] G. Bozzi, S. Catani, D. de Florian, M. Grazzini, Nucl.Phys. **B737**, 73-120 (2006) arXiv:hep-ph/0508068v1.
- [30] F. Hautmann, H. Jung, A. Lelek, V. Radescu and R. Zlebcik, JHEP 01, 070 (2018), arXiv:1708.03279v1 [hep-ph].
- [31] J. Blumlein, Workshop on Deep Inelastic Scattering and QCD, Paris, France, April 24-28, 1995, pp. 265-268, arXiv:hep-ph/9506403.
- [32] F. Hautmann and H. Jung, Nucl. Phys. B883, 1 (2014). arXiv: 1312.7875 [hep-ph].
- [33] V. N. Gribov and L. N. Lipatov, Sov. J. Nucl. Phys. 15 (1972) 438; G. Altarelli and G. Parisi, Nucl. Phys. B126 (1977) 298; Yu. L. Dokshitzer, Sov. J. Nucl. Phys. 46 (1977) 641.
- [34] F. Hautmann, L. Keersmaekers, A. Lelek and A.M. van Kampen, Nuclear Physics **B949** (2019) 114795.
- [35] A.M. van Kampen, *Transverse Momentum Dependent Parton Distribution Functions in Quantum Chromodynamics and Their Application to LHC Physics*, Master Thesis, University of Antwerp, Faculty of Sciences, Department of Physics, 2019.
- [36] T. Sjostrand and P.Z. Skands, Eur. Phys. J. C 39 (2005) 129.
- [37] S. Gieseke, P. Stephens and B. R. Webber, JHEP 0312 (2003) 045.
- [38] F. Hautmann, H. Jung, A. Lelek, V. Radescu and R. Zlebcik, Phys. Lett. B 772 (2017) 446.
- [39] A. Banfi, B.K. El-Menoufi, P.F. Monni, Journal of High Energy Physics 2019 (1), arXiv:1807.11487 [hep-ph].
- [40] S. Catani, M. Ciafaloni, and F. Hautmann. High-energy factorization and small x heavy flavor production. *Nucl. Phys.*, B366:135-188, 1991.
- [41] D. de Florian and M. Grazzini, Phys. Rev. Lett. 85, 4678 (2000). hep-ph/0008152.
- [42] M. Buza, Y. Matiounine, J. Smith and W.L. van Neerven, Eur.Phys.J.C1:301-320, 1998, arXiv:hep-ph/9612398.
- [43] S. Catani, D. De Florian and M. Grazzini, Eur. Phys. J. C 79 (2019) no.8, 685 doi:10.1140/epjc/s10052-019-7174-9 [arXiv:1904.10365 [hep-ph]].
- [44] F. Coradeschi and T. Cridge, Comput.Phys.Commun. 238 (2019) 262-294, arXiv:1711.02083v2 [hep-ph].
- [45] F. Hautmann, H. Jung, M. Krämer, P. J. Mulders, E. R. Nocera, T. C. Rogers, and A. Signori, Eur. Phys. J. C74, 3220 (2014). 1408.3015.
- [46] H. Jung et al., Eur.Phys.J.C70:1237-1249,2010, arXiv:1008.0152v1 [hep-ph].
- [47] E. Accomando et al., *Phys.Lett.B* 803 (2020) 135293, arXiv:1910.13759v1 [hep-ph].

- [48] T. Hahn, Comput. Phys. Commun. 168 (2005) 78–95. arXiv:hep-ph/ 0404043.
- [49] J. C. Collins, D. E. Soper, Back-To-Back Jets: Fourier Transform from B to K-Transverse, Nucl. Phys. B197 (1982) 446–476.
- [50] A. Buckley et al., GLAS-PPE/2014-05, MCnet-14-29, IPPP/14/111, DCPT/14/222, arXiv:1412.7420v2 [hep-ph].
- [51] F. Hautmann, H. Jung and S.T. Monfared, Eur.Phys.J.C 74 (2014) 3082, arXiv:1407.5935v2 [hep-ph].
- [52] T. Sjöstrand, Comput.Phys.Comm. 246 (2020) 106910, arXiv:1907.09874v1 [hep-ph].
- [53] S. Frixione and B.R. Webber, JHEP06 (2002) 029.
- [54] A.B. Martinez et al., Phys. Rev. D 100, 074027 (2019), arXiv:1906.00919v2 [hep-ph].
- [55] A. Buckley et al., *Rivet user manual*, Comput. Phys. Commun. 184 (2013) 2803–2819, arXiv:1003.0694.
- [56] ATLAS collaboration, Eur. Phys. J. C 76(5), 1-61 (2016), arXiv:1512.02192v2 [hep-ex].
- [57] A.D. Martin, W.J. Stirling, R.S. Thorne and G. Watt, Eur.Phys.J.C63:189-285,2009, arXiv:0901.0002v3 [hep-ph].